Title
Effects of shape and surfaces on fluid-dynamic performance of organisms at intermediate Re

Author
Dolinajec, Trevor Hendry

Publication Date
2015

Peer reviewed|Thesis/dissertation

Effects of shape and surfaces on fluid-dynamic performance of organisms at intermediate Re

By

Trevor Hendry Dolinajec

A dissertation submitted in partial satisfaction of the

requirements for the degree of

Doctor of Philosophy

in

Biophysics

in the

Graduate Division

of the

University of California, Berkeley

Committee in charge: Professor Mimi A.R. Koehl

Professor Robert Dudley
Professor Robert Full
Professor John Taylor

Spring 2015

Abstract

Effects of shape and surfaces on fluid-dynamic performance of organisms at intermediate Re

by

Trevor Hendry Dolinajec

Doctor of Philosophy in Biophysics

University of California, Berkeley

Professor Mimi A.R. Koehl, Chair

An organism's performance in relation to the fluid it lives and operates in is important across size and time scales, but the effects on performance of body shape and proximity to a surface become particularly nuanced at intermediate Re. This physical regime in which both viscosity and inertia play important roles has not been studied as extensively as that of macroscopic animals in which inertia dominates or that of microscopic animals in which viscosity dominates. However, many ecologically important animals such as the copepod occupy these intermediate flow conditions, as do both airborne and aquatic propagules such as the sporocarps of fungi and the larvae of benthic animals. Through recorded observation and modeling this dissertation arrives at biological implication regarding these organisms' habitats and life cycles. This work also creates a fuller understanding of general principles that govern intermediate Re.

Zooplankton contain a range of morphologies, and life cycles that bring them in contact with surfaces that act as crucibles. The purpose of this study was to determine how the morphology and orientation of a variety of ecologically-important microscopic marine animals (adult copepod, snail veliger larva, barnacle nauplius and cyprid larvae) affect the forces they experience while swimming in the water column, and while on surfaces (e.g. prey captured on tentacles of benthic predators, larvae settled onto benthic substrata). Drag, lift, and side forces as well as moments were measured about three axes for dynamically-scaled physical models of each animal. These forces and moments can transport and reorient swimming animals, and can push, lift, peel, or shear animals off surfaces, and thus affect important ecological processes such as dispersal, predation, and larval settlement. The Reynolds numbers (Re, the ratio of inertial to viscous forces) for the zooplankton and the models was in the range of 10^2 to 10^3. Body shape and orientation of small animals were found to have significant

effects on the magnitudes of fluid dynamic forces and moments at Reynolds numbers of order 10^3, but were less important at lower Re's. The magnitude and direction of the net force on an organism was found to change drastically as an organism nears, and then lands on a surface. The shear stress on the attachment of a small animal to a surface that is caused by drag pushing the animal downstream is greater than the shear stress due to rotation of the organism by flow-induced spinning, thus zooplankton on surfaces are more likely to be pushed than twisted off the surfaces by water currents.

For phytopathogenic fungi in the order Erysiphales, the cause of the diseases called powdery mildew, reinfection or dispersal to a new host plant is contingent on sporocarps escaping a fluttering leaf, but the mechanisms that allow for this liberation are largely unknown and unquantified. The genus *Phyllactinia*, unlike other members of the order, has specialized and upwardly bent radial appendages that allow the body of the sporocarp to extend down from the bottom of the host leaf. This causes the tips of the appendages to be the only physical connection between the sporocarp and the leaf with a gap of up to 300μm, thus creating an arrangement where fluid flow may contribute to liberation. To test the importance of ambient fluid flow on sporocarp liberation forces and moments were measured and fluid flow around dynamically-scaled physical models was observed at Re of 60 - 360. Flow velocities, boundary layer heights, and sporocarp morphologies were varied to match unsteady flow conditions and sporocarp maturation. To test the importance of aeroelastically induced inertial forces the kinematics of fluttering leaves in a wind tunnel were recorded at a range of wind speeds, and samples of sporocarps were weighed. Physically modeled aerodynamic forces and moments alongside recorded inertial forces were compared to measured adhesive forces. The comparative forces strongly suggest that steady wind flow and realistic turbulent wind flow do not exert force necessary for liberation in magnitude or direction, but that unsteady flow can lead to significant pitching moments. The accelerations of fluttering leaves and the resulting inertial forces on sporocarps varied greatly among leaves, with forces large enough to liberate sporocarps occurring in a small subset of leaves with a characteristic flutter frequency of $\sim$25 Hz. Pitch-induced overturning of sporocarps can explain the removal of sporocarps observed on wind-exposed leaves, with more sporocarps liberated at greater wind speeds and towards the tips of leaves.

Terminal velocity is an important parameter in the wind dispersal of propagules (seeds, pollen grains, spores). Aerial righting and aerodynamic stability is common among vertebrate and invertebrate animals, and some propagules. Fungal sporocarps of the powdery mildew *Phyllactinia* have shapes that affect their terminal velocity and aerodynamic stability while operating at Re 1.0 - 3.3, thus *Phyllactinia* represents a model organism for aerodynamic performance at near-unity Re. The reproductive success of these mildew species is dependent on stability during aerial transport so that a particular orientation is achieved upon deposition. High speed videography was used to measure terminal velocity, angular velocities, and angular accelerations of free-falling sporocarps during aerial righting. Physical models allowed for qualification of forces

and moments acting on sporocarps falling at terminal velocity, as well as providing fine-scale flow visualization. The morphology of sporocarps is dependent on their maturity, and experiments carried out with collected sporocarps showed that terminal velocity is partially a function of morphological parameters. Terminal velocities of sporocarps ranged from 8 to 28 cm/s. Flow visualizations showed that both the width and length of the wake formed around a falling sporocarp were dependent on the spread of the characteristic radial appendages of the genus. Sporocarps were recorded rotating while falling prior to reaching stability, and angular velocity and angular accelerations decreased as sporocarps approached zero angle of attack. Models confirmed that a stable fixed point existed at an angle of attack of zero for all tested morphologies of *Phyllactinia* sporocarps. However, naturally occurring morphologies that were the most likely to have smaller terminal velocities also displayed smaller aerial-righting moments, and sporocarps most likely to have larger terminal velocities displayed larger aerial-righting moments. This suggests a potential trade-off between sporocarps that are more stable (larger aerial-righting moments) and those that can disperse longer horizontal distances (smaller terminal velocity).

This work is dedicated to

Nidia and Amanita

1

Hydrodynamic forces and moments on zooplankton mid-water versus on surfaces

KEYWORDS

zooplankton, larvae, copepod, hydrodynamics, intermediate Reynolds number, drag, shear

HIGHLIGHTS

- Hydrodynamic forces on zooplankton when mid-water affect swimming and dispersal
- Forces on zooplankton on surfaces affect larval settlement & capture by predators
- Body shape & orientation affect forces & moments on zooplankton only in fast flow
- Magnitude & direction of force changes as an animal nears and lands on a surface
- Small animals are pushed rather than twisted off surfaces by flowing water

INTRODUCTION

Microscopic planktonic animals are abundant and ecologically important. For example, small planktonic copepods play a critical role in pelagic marine food webs (e.g. Turner, 2004; Kiorboe, 2008). Zooplankton are also an important food source for benthic predators such as corals and sea anemones (e.g. Sebens, 1981; Sebens and Koehl, 1984; Heidelberg et al., 2004; Robinson et al., 2013), thereby making an important contribution to the transfer of carbon from the water column to the benthos (e.g. Ambler et al., 1985; and reviewed in Heip et al., 1995). Furthermore, many benthic animals release microscopic planktonic larvae that are dispersed by ocean currents and then settle onto the substratum and recruit to new sites (e.g. Rodriguez et al., 1993; McEdward, 1995; Eckman, 1996; Abelson and Denny, 1997; Schiel, 2004; Koehl, 2007).

Hydrodynamic forces and moments on these microscopic animals can affect the ecologically-important processes of zooplankton transport, prey capture, and larval settlement. Hydrodynamic forces and moments can resist the motion of strong swimmers such as adult copepods, and weak swimmers such as nauplius larvae of crustaceans and veliger larvae of mollusks, and thus can affect metabolic cost of transport (e.g. Strickler, 1977; Pasternak et al., 2004; Visser and Kiorboe, 2006). Forces and moments on zooplankton on surfaces are also ecologically important. Settling larvae can be swept off the substratum by ambient water currents (e.g. Abelson and Denny, 1997; Koehl, 2007; Reidenbach et al., 2008; Koehl and Hadfield, 2004). Likewise, ambient water flow can dislodge prey from the capture surfaces of predators such as tentaculate suspension feeders (e.g. reviewed in Shimeta and Jumars, 1991; Shimeta and Koehl, 1997; Robinson et al., 2013).

Hydrodynamic forces and moments

Hydrodynamic forces and moments on bodies in the size and speed range of small zooplankton are poorly understood. These animals operate at intermediate Reynolds numbers (Re). Re is the ratio of inertial forces to viscous forces for a given flow situation,

$$Re = UL/\nu \tag{1.1}$$

where U is the velocity of the fluid relative to the animal, L is a characteristic linear dimension of the animal (body length in this study), and ν is the kinematic viscosity of the fluid. The fluid mechanics of very small organisms that operate at low Re's (e.g. the Re of bacteria is $\sim 10^{-5}$) have been well studied (e.g. Cisneros et al., 2007). At low Re, the flow is laminar and the hydrodynamic forces are mainly due to the viscous resistance to water being sheared. The fluid mechanics of large, rapidly-moving organisms (e.g. whales that operate at Re $\sim 10^6$) is also well understood (e.g. Weber et al., 2009). At high Re the flow is turbulent and inertial forces are much larger than viscous forces (Vogel 1996). Zooplankton range in size from $\sim$100 to $\sim$3000 μm (e.g. Smith, 1977), and when on surfaces in wave-exposed sites may experience maximum

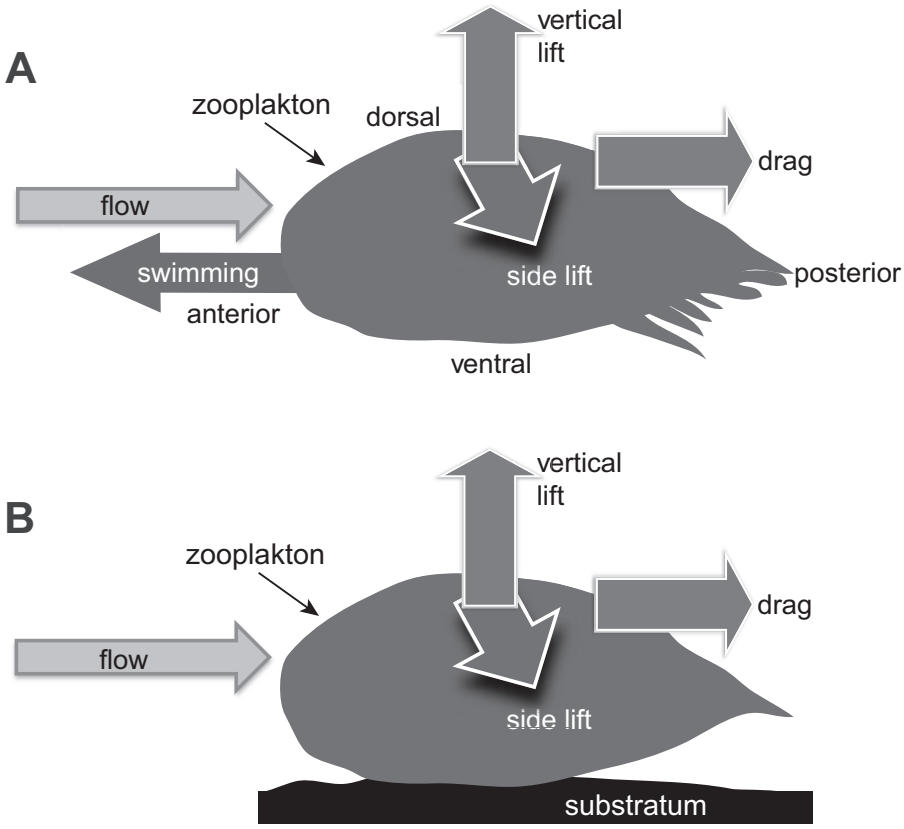

Figure 1.1: Diagrams of the hydrodynamic forces (dark grey arrows) on a barnacle cyprid larva while swimming mid-water (A), and attached to a substratum (B). The light grey arrow shows the direction of water flow relative to the larva. The two components of lift are either in the reference frame of the animal (A), or in the reference frame of the substratum (B). Drag is always in the direction of flow.

water velocities over 2 m/s (e.g. Koehl, 1977; Denny, 1988; Guinez and Pacheco, 1999; Gaylord et al., 2008), and thus operate at intermediate Re's of 10^2 to 10^3. Furthermore, escape swimming of adult copepods reaches Re's of approximately 10^3 (Borazjani at al., 2010).

Drag (D) is the fluid dynamic force on a body that acts in the direction of fluid motion relative to the body:

$$\mathrm{D} = 1/2 C_D \rho S U^2 \tag{1.2}$$

where ρ is the density of the fluid, S is the projected area of the animal, U is the velocity of the fluid relative to the body, and C_D is a shape-dependent drag coefficient. Lift (L) is the fluid dynamic force on a body acting orthogonal to the drag:

$$\mathrm{L} = 1/2 C_L \rho S U^2 \tag{1.3}$$

where, C_L is a shape-dependent coefficient. For an organism on surfaces, lift is sepa-

rated into two components, "vertical lift" normal to the surface, and "side lift" parallel to the surface. For swimming animals "vertical lift" acts in the sagittal plane, and "side lift" acts in the transverse plane (Fig. 1.1). It is appropriate to discuss the hydrodynamic forces acting on an animal of zooplanktonic size entirely in terms of drag and lift since the acceleration reaction force scales as volume and will necessarily be three orders of magnitude smaller in this case (Vogel, 1996).

Drag coefficients in the Re range of 10^2 to 10^3 have been determined by fitting experimental data for spheres and cylinders that were not near a surface (Vogel, 1996). Lift coefficients for bodies in the water column are also a function of Re, however equations for C_L below a Re of 10^3 were determined for non-rigid bubbles (reviewed in Pang and Wei, 2011). The C_D's in this Re range for a sphere on a surface have been reported (Reidenbach et al., 2009), but C_L's for bodies on surfaces in this Re range have not to the author's knowledge been measured. Bumblebees flying at a Re of 1500 were shown to have C_D's that varied from 0.5 to 1.3 as a function of body angle (Dudley and Ellington, 1990), but the effects of the non-spherical body shapes of animals and of their orientations relative to the flow are still poorly understood in the Re range of 10^2-10^3.

In addition to lift and drag forces, an animal may experience hydrodynamic moments when fluid moves relative to it. For flying or swimming animals, the three moments discussed are roll, pitch and yaw, which are in the reference frame of the animal (Fig. 1.2A). These terms are used in this study when considering animals in the water column. However, for animals near a surface the moments are described in the reference frame of the surface, and labeled "parallel peel", "orthogonal peel", and "spinning shear" (Fig. 1.2B). These alternative names for moments are useful in elucidating the potential effect moments have in detaching an animal from the capture surface of a predator or from the substratum. The hydrodynamic moments in the frame of the animal are given by:

$$\text{Pitch, or Parallel Peel} = 1/2 C_M \rho S U^2 L \tag{1.4}$$

$$\text{Roll, or Orthogonal Peel} = 1/2 C_R \rho S U^2 L \tag{1.5}$$

$$\text{Yaw, or Spinning Shear} = 1/2 C_N \rho S U^2 L \tag{1.6}$$

where S is the projected area, L is the length of the body, U is the water velocity relative to the body, ρ is the fluid density, and C_M, C_R, and C_N are coefficients that are dependent on shape and orientation (McCay, 2001; Koehl et al., 2011).

Forces and moments on zooplankton at Re of 10^2 - 10^3:

Zooplankton in the water column

The hydrodynamics of a few types of zooplanktonic animals swimming at intermediate Re have been studied. For example, computational models of rapid escape

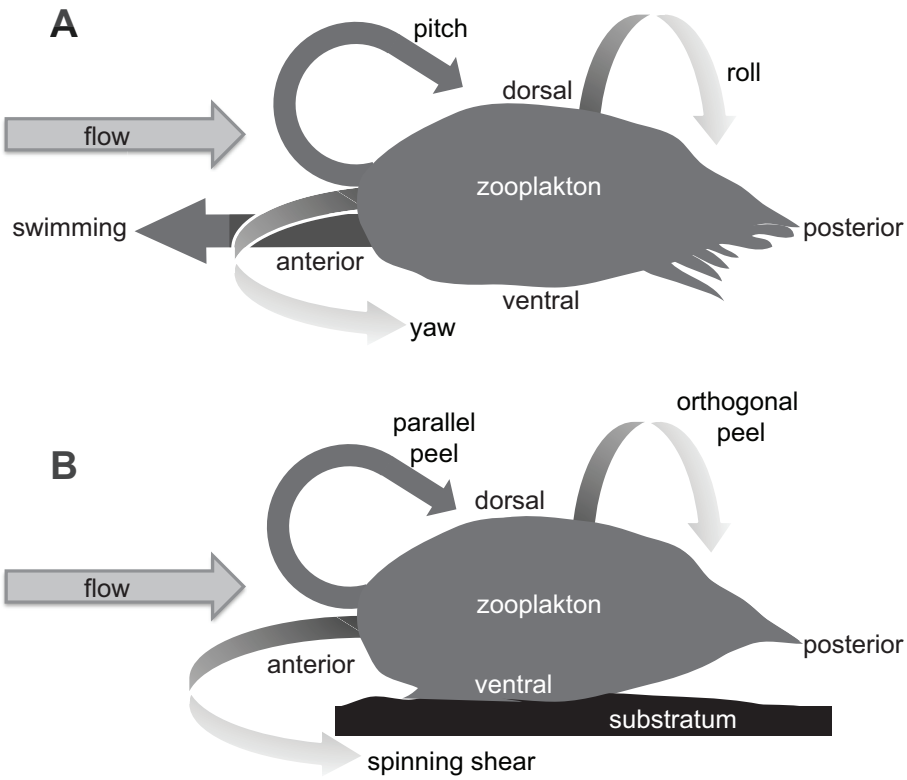

Figure 1.2: Diagram of the hydrodynamic moments (curved arrows) on a barnacle cyprid while swimming mid-water (A), and attached to the substratum (B). The light grey arrow shows the direction of water flow relative to the larva. The three moments are either in the reference frame of the animal (A), or in the reference frame of the flow direction and substratum (B). The diagram shows the animal anterior to the flow where parallel peel is equivalent to the pitch (Eqn. 1.4), spinning shear is equivalent to yaw (Eqn. 1.6), and orthogonal peel is equivalent to roll (Eqn. 1.5). However, when the animal is lateral to the flow, parallel peel is equivalent to roll, spinning shear is equivalent to yaw, and orthogonal peel is equivalent to pitch. When the animal is ventral to the flow parallel peel is equivalent to roll, spinning shear is equivalent to pitch, and orthogonal peel is equivalent to yaw.

swimming by copepods at Re = 10^3 suggest they produce thrust with their antennae (Borazjani et al., 2010). In another recent study an analytical model was used in conjunction with numerical simulation to estimate the propulsion forces per animal cross-sectional area produced by escaping copepods in the Re range of 10^2-10^3, and the values were found to be 50-150 Nm^{-2} (Kiorboe et al., 2010). For slightly lower Re (10^1-10^2) than those in this study, the relative contribution of viscous and inertial forces to the generation of thrust and drag was explored for swimming ascidian larvae (McHenry et al., 2003). The moments on echinoderm larvae of different shapes swimming in an ambient steady shear flow have also been analyzed (Grunbaum and Strathmann, 2003). However, drag, lift, and moments have not been compared across species of microscopic swimmers with different body shapes at Re values of 10^2 to 10^3, nor have comparisons been made between forces and moments experienced by these animals when near or on a surface versus when in the water column.

Zooplankton on surfaces

The hydrodynamics of capture of zooplankton from the water flowing past benthic suspension-feeding predators has been studied. For example, the effects of the velocity profile and turbulence structure of the benthic boundary layer on food delivery to the predators has been investigated (e.g. Nowell and Jumars, 1987; Estes and Peterson, 2000), and the effects of waves on prey capture has been studied (e.g. Hunter, 1989; Johnson and Sebens, 1993; Heidelberg et al., 2004; Robinson et al., 2013)

On a finer scale, the effects of ambient flow and of the size and density of prey on the physical mechanisms by which they are captured by predator tentacles have been analyzed (e.g. Rubenstein and Koehl, 1977; reviewed in Shimeta and Jumars, 1991). Another important factor affecting rates of predation on zooplankton by benthic animals is their ability to retain captured prey in the face of ambient currents (e.g. Shimeta and Koehl, 1997; Pratt 2008; Robinson et al., 2013). Some studies have measured the strength of the adhesion of prey to the capture surfaces of benthic suspension feeders (e.g. Canova, 1999). However, the effects of prey body shape and orientation on the hydrodynamic forces and moments that could wash them off capture surfaces of predators have not yet been reported to the knowledge of the authors.

The hydrodynamics of marine larvae settling onto surfaces have been well studied (e.g. reviewed by Butman, 1989; Abelson, 1997; Abelson and Denny, 1997; Koehl, 2007; Koehl and Hadfield, 2010). Some of these studies have focused on how ambient water flow affects the delivery of larvae to the substratum and on larval behavior following encounter with a surface, while other studies quantified the temporal patterns of shear stresses in the water flowing past larvae as they sit on surfaces (Crimaldi et al., 2002; Reidenbach et al., 2009). A few studies have focused on the water velocities required to dislodge settling larvae from the substratum (e.g. Eckman et al., 1990; Koehl and Hadfield, 2004; Zardus et al., 2008). Although most of these studies report the boundary shear stress required to dislodge larvae from surfaces, a few reported forces on individual larvae. Eckman et al. (1990) calculated that the drag force to

detach a barnacle cyprid larva from a surface ranged from 0.30μN to 24.7 μN. Yule and Walker (1984) directly measured that forces of 9 and 344 mN were required to pull juvenile barnacles as young as one day after metamorphosis off slate surfaces. These studies correlate observations and measurements of the flow to behavior or dislodgment of larvae, but they do not explore the consequences of larval body shape and orientation on the hydrodynamic forces they experience while on surfaces.

Although the moments that aquatic animals on surfaces experience in the Re range of 10^2 - 10^3 may have ecological importance, they have received little attention. The torque on larvae in the water velocity gradient near a surface has been suggested as a means of restricting settling larvae to the viscous sublayer of the benthic boundary layer (Jonsson et al., 1991), and the potential of torque in rolling propagules along the substratum has been acknowledged (Abelson and Denny, 1997). Neither of these studies, however, reported the magnitude of the moments that microscopic aquatic animals might experience.

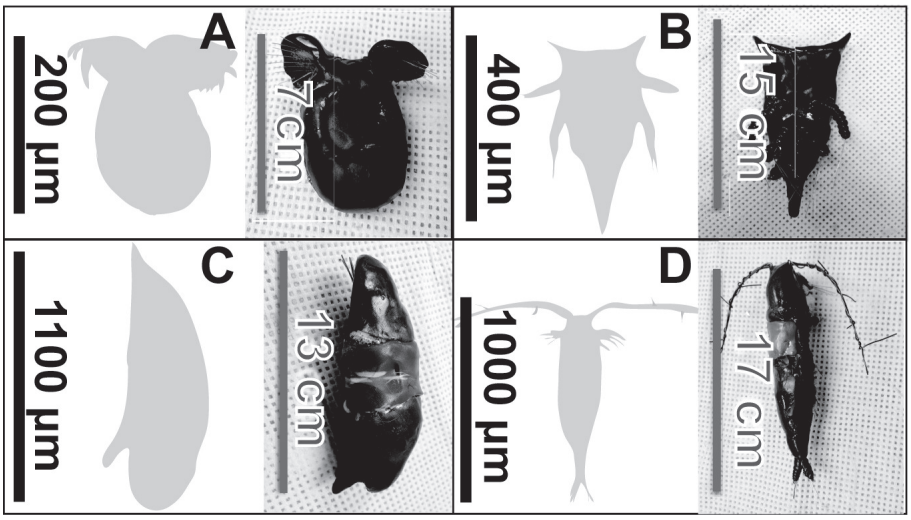

Figure 1.3: Diagrams of zooplankton (left) and photographs (right) of the models: A) Veliger larva (length = 200 μm) and model (length = 7 cm). B) Nauplius larva (length = 400 μm) and model (length = 15 cm). C) Cyprid larva (length = 1100 μm) and model (length = 13 cm). D) Calanoid copepod adult (length =1000 μm) and the model (length = 17 cm). The drawing shows the first antennae extended laterally while the photograph of the model shows the antennae bent back longitudinally. Both configurations of the antennae were tested.

The particular habitat considered in this study is that of wave-swept rocky shores.

Wave-swept rocky shores are an important model system for studying basic questions in community ecology and population dynamics (e.g. Paine, 1994; Nybakken, 2004, Denny et al., 2009; Denny and Gaines, 2007). Likewise, the effect of flow on macroscopic organisms on rocky shores is well studied (e.g. Koehl, 1977; Denny, 1988, Gaylord et al., 2008). However, the forces on microscopic creatures on surfaces in these habitats has received less attention.

Objectives

The objective of the study reported here was to explore how body design and association with a substratum affects the fluid dynamic forces and moments on bodies at Reynolds numbers of 10^2 to 10^3. Study organisms were chosen that represent a variety of common body forms in the plankton (molluscan veliger larvae, crustacean nauplius larvae, barnacle cyprid larvae, and adult calanoid copepods; Fig 1.3), and that interact with surfaces when captured by larger benthic predators or when settling onto the substratum. The body shapes were chosen to capture a wide range of morphologies, included the nearly spherical veliger and long narrow adult copepods. The specific hypotheses of the study were:

1) Body shape effects the hydrodynamic forces and moments acting on the body, with greater forces or moments acting on one body shape as compared to another at the same Re.

2) For a given animal body shape ay a given flow velocity, body orientation with respect to the flow effects hydrodynamic forces and moments.

3) Forces and moments on zooplankton on surfaces are different from those on animals when not near a surface, and the presence of a small gap (1/10 characteristic length) between an animal and a surface will further affect forces and moments.

The forces and moments measured in this study affect ecologically important processes such as swimming, predation, and larval settlement.

METHODS

Hydrodynamic forces and moments on zooplankton were studied in the water column and on rocky shores exposed to waves. The Reynolds numbers (Re) of the zooplankton studied were based on water flow measurements near the substratum at two rocky shore sites in the Bodega Marine Reserve, University of California, Davis. The zooplanktivorous sea anemones *Anthopleura elegantissima* are abundant at these sites, and the larvae of benthic animals accumulate in the nearby water (Mace and Morgan, 2006). Water velocities were measured 2cm above *A. elegantissima* at these sites by acoustic Doppler velocimetry(Robinson et al., 2013), and were used to calculate the Re

of zooplankton on surfaces. This research focused on four types of zooplankton that are common in the Bodega costal waters, and are prey for benthic suspension feeders or are settlers onto rocky substrata. These study animals were the adult calanoid copepod *Acartia clausi* (Smith, 1977; Marcus, 1995); the pretorsional veliger larva of the black limpet *Lottia asmi* (Kay and Emlet, 2002); the nauplius larva of the barnacle *Chthamalus fissus*; and the cyprid larva of the same barnacle species (Morris et al., 1980; Miller et al., 1989). These four types of organisms were chosen to represent a variety of body sizes and shapes, and also to represent a range of swimming abilities, from strong, rapid swimmers (e.g. copepods) to slow swimmers (e.g. veliger larvae).

Dynamically-scaled physical models

Forces and moments on dynamically scaled physical models (Fig 1.3) of these zooplankton of diverse shapes were measured. The models of the organisms studied were made of Sculpey modeling clay (www.sculpey.com) on a metal framework, and metal wire was used to make setae. The dimensions of the models, which were geometrically similar to the animals, were based on measurements made on published images (Smith, 1977; Morris et al., 1980; Miller et al., 1989 Marcus, 1995; Kay and Emlet, 2002). All models contained a metal core by which they could be mounted on a force and moment transducer.

Models were dynamically similar to zooplankton at a Re range of 10^2 to 10^3, so the ratios of velocities and of forces at comparable positions in the fluid around each animal and its model were the same (Vogel, 1996; Koehl, 2003; Sane, 2003). The animals studied had characteristic linear dimensions ranging from 200μm to 1100μm. The environmental flows of interest, which ranged from 0.8 to 2.24 m/s, represented ambient water flow that might dislodge a settling larva or detach captured prey from the surface of a predator. Thus the Re range of the animals in this study was 300-2300. To match this Re range models (7 to 17 cm in length) were towed through mineral oil at velocities of 0.25 cm/s to 0.8 cm/s. Experiments were conducted at 20°C, so the oil had a viscosity of 0.049 Pa s (measured with a Brookfield DV-II digital viscometer, Brookfield Engineering Laboratories, Massachusetts USA), and a density of 850 kg/m^3 (measured by mass and volume of samples).

Towing tank and force measurements

The models were attached to a force and moment transducer (ATI Nano17 force transducer, www.ati-ia.com) that measured forces in three orthogonal directions and moments about three orthogonal axes. The transducer was attached to a robotic arm capable of rotating in pitch, roll and yaw. Pitch and roll angles of the model were controlled by means of two hobby servo motors (Hitec HS-5475HB digital servos, www.hitecrcd.com), and yaw was controlled by manually adjusting the model. Both servos were independently controlled by an Arduino micro controller board (arduino.com) (Munk, 2011).The robotic arm was mounted on a cart that allowed the

model to be towed through a tank of mineral oil at specified velocities (Fig 1.4; Munk, 2011). The tank, which was made from clear acrylic plastic, was 2.1m in length, 0.32 m in width, and 0.40 m in depth. Structural support for the tank was provided by T-slotted aluminum framing (80/20 10 Series T-slot framing, www.8020.net), on which the towing equipment was mounted. A stepper motor (Vexta PH2610-E2.9 standard resolution stepping motor; www.orientalmotor.com) used to drive the cart along tracks on the top of the tank was controlled by an Advanced Micro Systems SAX integrated driver/controlled/power supply (www.ams2000.com). The driver was programmed via serial RS-4222 connected to a PC computer.

The force transducer was fixed relative to the model and rotated with it, therefore

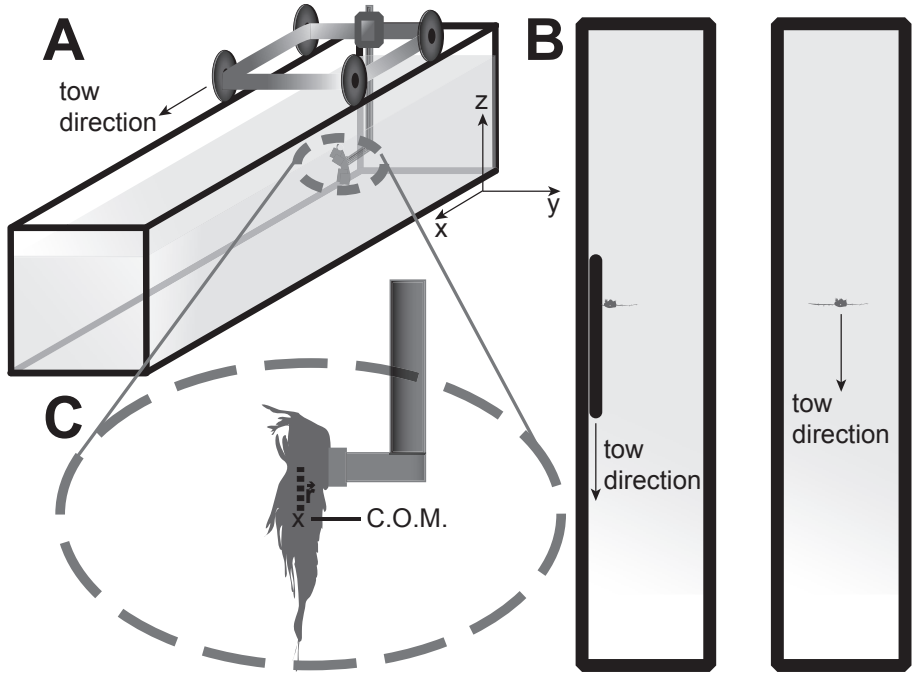

Figure 1.4: A) Diagram of the towing tank showing the towing rig and the robotic arm upon which the force transducer and the model were attached. B) Top views of the towing tank, where the back of the tank is at the top of the diagrams and the models are towed from the back towards the front of the tank. The left diagram shows the moving substratum (black) and nearby model (grey) being towed along the left wall of the tank. The right diagram shows the model being towed along the middle of the tank without nearby surfaces. C) Zoomed view showing the model (light grey) and the displacement vector (dashed line) pointing from the model center of mass (C.O.M.) to the connection point to the transducer (dark grey).

the transducer output was in the frame of reference of the model (as shown in Figs. 1.1 and 1.2), not the frame of reference of the tank. The signal from the force transducer was fed to a National Instruments PCI-6220 data acquisition (DAQ) card and data were recorded on a PC at a sampling rate of 1000Hz. Prior to each tow, a baseline

measurement was used to remove gravity from the readings of the transducer so that forces and moments measured were only those due to the fluid acting on the model (Munk, 2011).

Only forces and moments measured during the middle of a tow when constant velocity was maintained were included in our analysis. The forces and moments acting on a model as it was accelerated at the start and decelerated at the end of a tow were not considered. The center of mass of the models was found by suspending the models and adjusting the suspension point until balance was achieved. Once the location of the center of mass had been determined for each model, the forces and moments measured at the transducer (which was not necessarily located at the center of mass) were used to calculate the forces and moments acting at the center of mass. Since the center of mass was not accelerating during the tow region of interest, the forces measured at the transducer were the same as those at the model's center of mass. The moments about the center of mass were calculated from the moments measured by the transducer by adding a component of torque due to the moment arm between the transducer location and the center of mass. This correction was

$$\tau_{\mathbf{CM}} = \tau_{\mathbf{FT}} - \mathbf{r} \times \mathbf{F} \tag{1.7}$$

where τ_{CM} was the desired vector of torque exerted about the center of mass, τ_{FT} and $\mathbf{F}$ were the vectors of torque and force, respectively, as measured by the transducer during a given run, and $\mathbf{r}$ was the vector between the center of mass and the transducer (Munk, 2011).

For experiments in which the organism was on a substratum relative to which fluid was moving, a plate of Plexiglass (35 cm x 55 cm x 0.3 cm) was attached to the towing cart and dragged alongside the model through the oil (Fig. 1.4B). Because boundary layers in the water flowing over rocky shores build up with time as each wave passes over a surface (Denny 1988), captured prey and settled larvae are more likely to be swept off surfaces when a wave first hits and the boundary layer is very thin. Therefore, during the portion of the tow when forces and moments were measured on the models on surfaces, the boundary layer along the plate was designed to correspond to those that form a few milliseconds after waves start to move across a surface. The thickness (δ) of the boundary layer that forms when a fluid impulsively starts moving across a surface is given by:

$$\delta = \sqrt{\nu \mathbf{t}} \tag{1.8}$$

where t is the time elapsed since the impulsive start of the fluid flow, and ν is the kinematic viscosity of the fluid (1.05×10^{-6} m^2/s for sweater at 20°C) (Batchelor, 1967). The thickness of the boundary layer that develops in 1 to 13 ms after a wave with water velocity 1.6 m/s impulsively hits a substratum was estimated to be 30 to 110 μm for the real animals, which corresponds to a δ of 11 to 13 mm for the models.

Experiments were conducted to test the effects of being near a substratum versus on a substratum. For both types of experiments, the Plexiglass was mounted as close as possible to the model while not t making physical contact, so that the signal from the

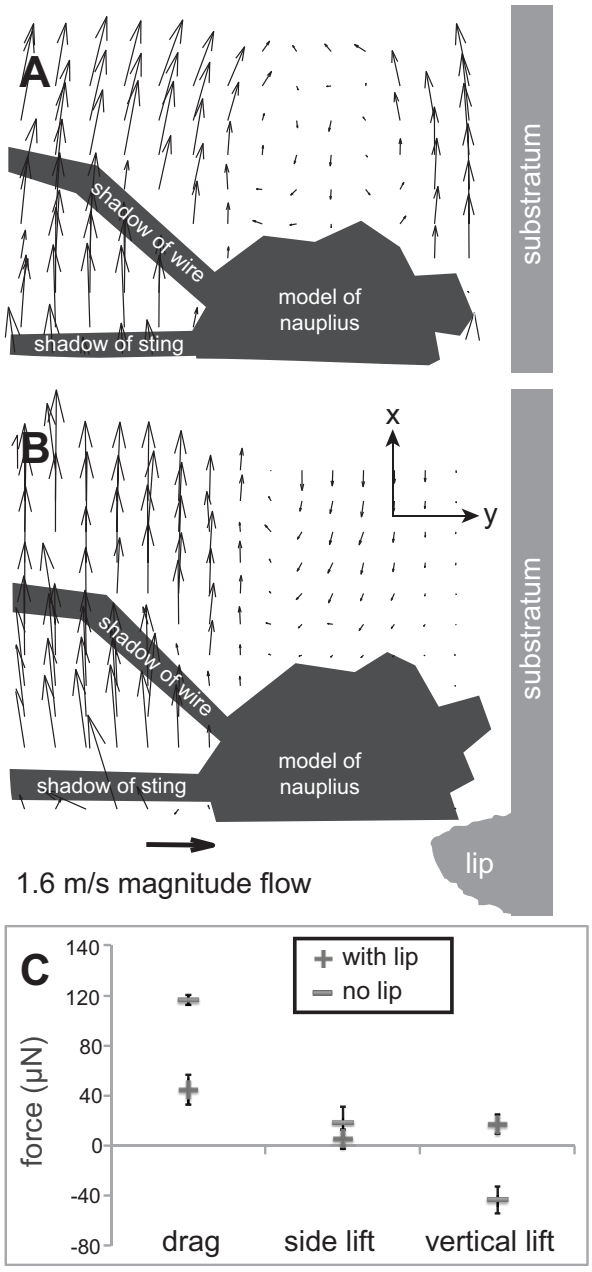

Figure 1.5: A) Water velocity vectors around the model of the nauplius in the lateral orientation with respect to the water flow and in a position "near to the substratum" (i.e. without a lip attached to the substratum). B) Water velocity vectors around the same model in the same orientation, but "on the substratum" (i.e.with a small upstream lip to prevent flow between the model and the substratum). C) The forces with and without a lip for the nauplius in the lateral position in a 1.6 m/s flow. The drag and vertical lift forces were significantly greater when the model was "near" the substraum (no lip) than when it was "on" the substratum (lip) (t-tests, $p<0.05$).

transducer was only due to forces and moments on the model, and not the model coupled with the much larger substratum surface. For runs in which the organism was meant to be attached to the substratum, a lip that was about 10% of the height of the model was built 15 mm upstream from the model to prevent flow through the gap left between the model and the surface. The necessity of using the lip is shown in Fig. 1.5, where flow is clearly shown passing between the model and the substratum without the lip. The lip was not used for experiments mimicking organisms near the substratum, but not attached to it. Both drag and vertical lift were affected by the presence of the lip (Fig. 1.5). This technique of towing a model and the substratum through the fluid while using a small lip to prevent flow between them was an alternative to moving fluid past a stationary model on a transducer mount extending through a hole in the substratum, an approach other studies have used (e.g. Koehl 1977; Denny et al., 1985).

The possibility that proximity to the walls of the tank might affect the forces measured was considered. Drag is increased by no more than 5% due to wall effects if

$$\frac{Y}{L} > \frac{15}{Re} \tag{1.9}$$

where Y is the distance to the wall, and L is the characteristic length of the model (Vogel, 1996, and modified by Loudon et al., 1994). When the models were towed in the middle of the tank they were 13 cm from each wall. When the models were next to the substratum (a wall whose hydrodynamic effect was wanted in the study), they were approximately 25 cm from the opposite tank wall (a wall that needed to be ignored). Since the characteristic length of the models ranged from 7-17 cm and the Re from 300-2300, the above inequality was satisfied many times over, and thus no wall artifacts should be expected.

The small forces on real zooplankters were calculated from the larger forces measured on the models. The amplification factor relating forces on large models to forces on their microscopic prototype organisms can be calculated by considering the force equation without coefficients as a proportionality:

$$F \propto \rho S U^2 \propto \rho (LU)^2 \propto \rho (Re\mu/\rho)^2 \tag{1.10}$$

If one such proportionality is considered for the forces in water and the forces in oil then their ratio is obtained as follows:

$$\frac{F_{oil}}{F_{water}} = \frac{\mu_{oil}^2 \rho_{water}}{\mu_{water}^2 \rho_{oil}} \tag{1.11}$$

where Re has cancelled from the numerator and denominator since it was matched. Once the appropriate values are used one finds that the amplification factor is approximately 2200. This was very useful for the quality of the signal since the forces on the zooplankton were on the order of 100 μN, and yet forces could be recorded acting on the models on the order of 10^{-1} N.

Particle image velocimetry

The fluid velocity vector fields around the models were determined using particle image velocimetry (PIV). A horizontal sheet of laser light illuminated neutrally-buoyant particles in the oil (silver-coated hollow glass spheres 13 μm in diameter (Potter Industries, www.pottersbeads.com). The light sheet was produced by shining the beam from a 300 mW, 532 nm laser (Wicked Lasers S3 Krypton Series; www.wickedlasers.com) through a prism that was mounted at one end of the tank. The sheet of light was at the height of the center of mass of the model being towed. The paths of the marker beads relative to the model was recorded at 60 fps by a video camera (Fastec Hispec 1 Color camera; www.fastecimaging.com). The images were processed using PIVlab (Thielicke, 2014) for Matlab 2008a, using sampling windows of 1280x1044 pixels to calculate velocity vector fields.

Statistical Analysis

Student's t-tests and ANOVA - Tukey tests were conducted using Excel for Mac 2011 and Matlab 2012b, respectively. The built-in TTEST function was used in Excel. The multcompare function was used in Matlab with the Tukey-Kramer default critical value type.

RESULTS

Drag and lift coefficients of zooplankton compared with geometric shapes

The measured forces on dynamically-scalled models of veliger, nauplius, and cyprid larvae and of adult copepods were used to calculate drag coefficients (C_D's) and lift coefficients (C_L's) so that the effects of body shape could be compared. For each shape tested C_D was greater than vertical C_L, which in turn was greater than side C_L (Table 1). Fig. 1.6 shows drag coefficients (C_D's) as a function of Re for the four animal shapes. The signal-to-noise ratio of the force transducer was smaller at the lower towing velocities than at higher velocities, hence the error bars for the coefficients calculated for lower Re are larger.

The fluid-dynamic forces on microscopic organisms are often estimated by approximating the organisms as cylinders or spheres (e.g. Vogel, 1996; Reidenbach et al., 2009). This approach was tested by comparing our measured C_D's and C_L's for animal body shapes with those calculated for simple geometric shapes in the same range of Reynolds numbers. The curves for C_D as a function of Re for cylinder and a sphere when not near any boundaries were calculated as described in Vogel (1996). The C_D for a long cylinder with its long axis orthogonal to the flow (Fig. 1.6A) is given by

$$C_D = 1 + 10Re^{-2/3} \tag{1.12}$$

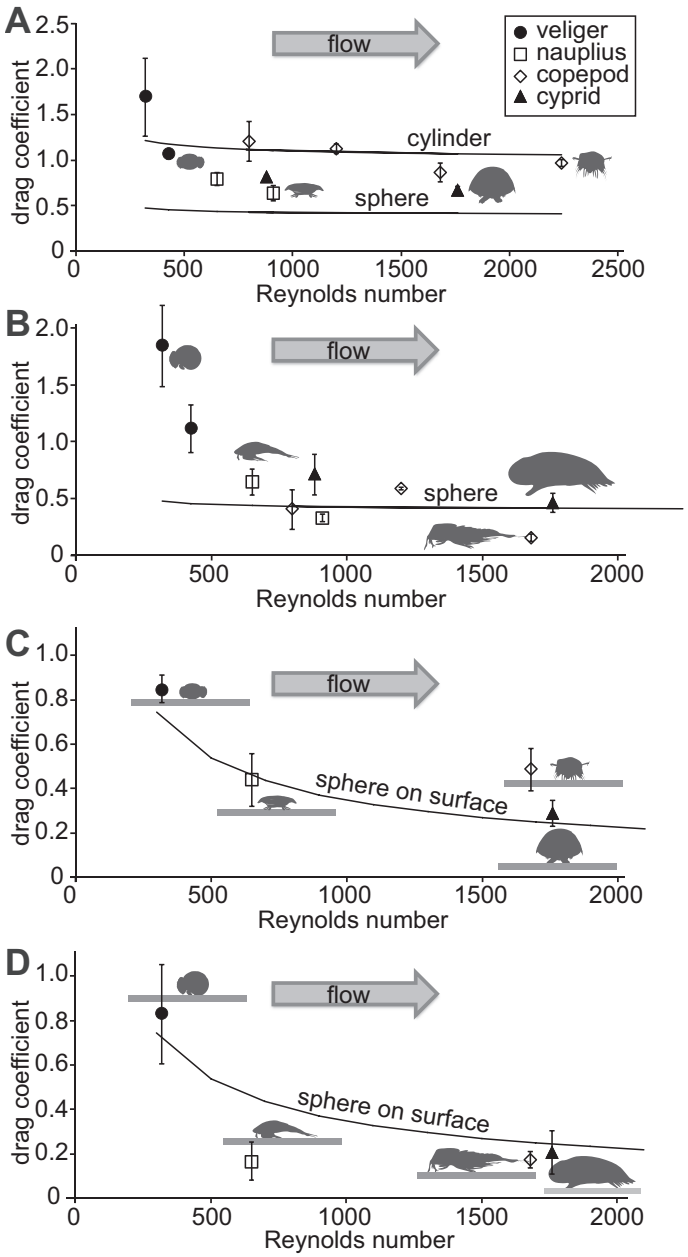

Figure 1.6: Drag coefficients plotted as a function of Re for models of animals when they were mid-water and lateral to the flow (A), mid-water and anterior to the flow (B), on a surface and lateral to the flow(C), and on a surface and facing upstream (D). Lines in (A) and (B) represent drag on a cylinder normal to the flow (Eqn. 1.11) and on a sphere (Eqn. 1.12) when they are not near a surface, and lines in (C) and (D) represent drag on a sphere on a surface (Eqn. 1.13). Grey arrow shows flow direction relative to the models (grey diagrams).

The C_D for a sphere (Figs. 1.6,A and B) is given by

$$C_D = \frac{24}{Re + 6/(1 + Re^{1/2})} + 0.4 \tag{1.13}$$

The C_D for a sphere near a surface (Fig. 1.6,C and D) was calculated as described by Reidenbach et al. (2009) for Re > 3:

$$C_D = \frac{27}{Re^{0.63}} \tag{1.14}$$

Both the body orientation and proximity to a surface affected how the drag and lift on the animal shapes compared with those of spheres and cylinders. When broadside to the flow and not near a substratum, all the animal shapes had C_D's higher than those of a sphere, but similar to or lower than those of a cylinder at comparable Re's (Fig. 1.6A). However, when the animal models were facing upstream with their long axes parallel to the flow, the C_D's of the copepod, cyprid, and nauplius (all of which operated at Re's ≥ 800) were similar to those of a sphere, whereas the C_D's of the veliger (Re's < 500) were much higher (Fig. 1.6B). In contrast, when models were on a surface and were broadside to the flow, their C_D's were comparable to or higher than the C_D's of a sphere at the same Re's (Fig. 1.6C). However, when the animal models on a surface were facing upstream, all but the bluff veliger had C_D's lower than those of a sphere at comparable Re's (FIg. 1.6D).

Effects of body shape and orientation on forces when mid-water

The C_D's and lift coefficients (C_L's) of different body shapes in mid-water were compared to each other at the Re's at which they overlapped: the nauplius, cyprid, and copepod were compared at Re ≈ 800, and the cyprid and copepod were compared at Re ≈ 1700 (Table 1B). All of the comparisons shown in Table 1 were made using the copepod with its antennae bent back parallel to the longitudinal axis of the body (photograph in Fig. 1.3D). At Re ≈ 1700, the C_D's of copepods were significantly lower than those of cyprids in all orientations. In contrast, at a lower Re of ≈ 800, there was no difference between the C_D's of copepods and cyprids, but the nauplius had signficantly lower C_D's than the cyprid when they were facing upstream. At Re $\approx$ 1700, cyprids had much higher vertical C_L's than did copepods, both when they were facing upstream and when they were broadside to the flow. However, as with drag at the lower Re of ≈ 800, shape had no effect on vertical C_L . Side C_L showed no dependence on shape at either Re.

The effects of body configuration on hydrodynamic forces were examined for the copepod in mid-water by comparing C_D's and C_L's when the long first antennae were extended laterally (diagram in Fig. 1.3D) versus when they were bent back parallel to the long axis of the body (photograph in Fig. 1.3D). At Re ≈ 800, C_D was higher when the antennae were extended laterally and the animal's ventral surface was facing

A

		Re ≈ 1700	
		Copepod	Cyprid
Drag Coefficient	Anterior to flow	0.17±0.04	0.21±0.10
	Lateral to flow	0.60±0.03	0.70±0.06 *
	Ventral to flow	0.30±0.03	0.67±0.14 *
Vertical Lift Coef.	Anterior to flow	0.01±0.02	0.06±0.05
	Lateral to flow	0.04±0.02	0.08±0.04
	Ventral to flow	0.16±0.06	0.06±0.04
Side Lift Coef.	Anterior to flow	0.05±0.04	0.06±0.09
	Lateral to flow	0.05±0.03	0.05±0.04
	Ventral to flow	0.09±0.06	0.03±0.02

B

		Re ≈ 800			Re ≈ 1700	
		Copepod	Cyprid	Nauplius	Copepod	Cyprid
Drag Coefficient	Anterior to flow	0.40±0.17	0.71±0.18 *	0.33±0.03 *	0.16±0.03 *	0.46±0.08 *
	Lateral to flow	0.73±0.90	0.80±0.04	0.64±0.09	0.53±0.06 *	0.76±0.08 *
	Ventral to flow	0.59±0.11	0.72±0.15	0.86±0.10	0.32±0.02 *	0.67±0.13 *
Vertical Lift Coef.	Anterior to flow	0.40±0.46	0.09±0.03	0.10±0.05	0.02±0.01 *	0.20±0.05 *
	Lateral to flow	0.53±0.59	0.49±0.14	0.15±0.07	0.02±0.01 *	0.34±0.06 *
	Ventral to flow	0.23±0.05	0.18±0.06	0.10±0.09	0.02±0.01	0.12±0.09
Side Lift Coef.	Anterior to flow	0.24±0.39	0.18±0.11	0.11±0.08	0.09±0.04	0.05±0.01
	Lateral to flow	1.1±1.3	0.10±0.11	0.04±0.03	0.11±0.10	0.14±0.08
	Ventral to flow	0.34±0.15	0.33±0.09	0.14±0.05	0.18±0.09	0.27±0.03

Table 1.1: Comparisons of drag coefficients and vertical and side lift coefficients for bodies of different shapes when on a surface at Re≈1700 (A) and when mid water at Re≈800 and Re≈1700 (B). Only animals at a given Re and orientation were compared. In Table A, models that were anterior or lateral to flow had their ventral surfaces on the substratum, and animals that were ventral to flow had their left side on the substratum. Brackets labeled with an asterisk indicate significant difference (ANOVA-Tukey, $p<0.05$ for significance when three shapes are compared at a given Re; t-tests, $p<0.05$ when two shapes are compared at a given Re).

upstream, but antennal configuration had no effect on C_D for other body orientations with respect to the flow (Table 1.2B). Antennal configuration had no effect on the C_L's for all orientations of copepods when mid-water at Re $\approx$ 800. In contrast, antennal orientation had larger effects on forces at higher velocities. At Re $\approx$ 1700, C_D's were higher when antennae were extended laterally for every orientation except lateral to the flow, and the C_L for vertical lift was higher for extended antennae when the copepod was lateral to the flow. However, C_L's were not affected by antennal configuration for other body orientations relative to the flow at Re $\approx$ 1700. (Table 1.2B).Thus, folding the long antennae back laterally along the sides of the body does not affect lift on a copepod in most cases, but decreases drag at higher speeds.

The effects of orientation with respect to the flow direction in mid-water were also tested for different body shapes when mid-water and the results will be presented below in comparison to bodies on surfaces. In summary, orientation had no effect on the lift force (ANOVA, Tukey, $p < 0.05$ for significance). In the cases of the cyprid, copepod,

A

		Re ≈ 1700 Extended	Re ≈ 1700 Folded
Drag Coefficient	Anterior to flow	0.27±0.08	0.17±0.04
	Lateral to flow	0.58±0.10	0.62±0.03
	Ventral to flow	0.34±0.02	0.29±0.03
Vertical Lift Coef.	Anterior to flow	0.04±0.02	0.01±0.02
	Lateral to flow	0.09±0.04	0.04±0.02
	Ventral to flow	0.12±0.07	0.09±0.06
Side Lift Coef.	Anterior to flow	0.04±0.01	0.05±0.04
	Lateral to flow	0.09±0.01	0.05±0.04
	Ventral to flow	0.16±0.02	0.16±0.03

B

		Re ≈ 800 Extended	Re ≈ 800 Folded	Re ≈ 1700 Extended	Re ≈ 1700 Folded
Drag Coefficient	Anterior to flow	0.29±0.62	0.40±0.17	0.31±0.07	0.16±0.03 *
	Lateral to flow	1.2±0.22	0.73±0.88	0.86±0.10	0.83±0.06
	Ventral to flow	0.77±0.05 *	0.59±0.11 *	0.41±0.03 *	0.32±0.02 *
Vertical Lift Coef.	Anterior to flow	0.47±0.59	0.40±0.45	0.02±0.00	0.02±0.01
	Lateral to flow	0.23±0.14	0.53±0.59	0.07±0.04 *	0.02±0.00 *
	Ventral to flow	0.18±0.09	0.23±0.05	0.05±0.03	0.02±0.01
Side Lift Coef.	Anterior to flow	0.34±0.35	0.24±0.39	0.11±0.09	0.09±0.04
	Lateral to flow	0.30±0.20	1.1±0.50	0.03±0.04	0.11±0.10
	Ventral to flow	0.31±0.22	0.34±0.15	0.11±0.09	0.18±0.09

Table 1.2: Comparisons of drag coefficients and vertical and side lift coefficients between copepods with extended and folded antennae, both on a surface at Re≈1700 (A) and mid water at Re≈800 and Re≈1700 (B). Brackets labeled with an asterisk indicate significant difference (t-tests, $p<0.05$).

and nauplius the drag force was always greater when the animals were broadside to the flow (i.e. lateral or ventral/dorsal to the flow) than when parallel to the flow (i.e. anterior/posterior). In the case of the veliger orientation had no effect on drag forces (ANOVA, Tukey, $p < 0.05$).

Effect of body shape and orientation on forces when on a substratum

Effects of body shape and orientation on the hydrodynamic forces experienced by animals attached to a substratum were studied (e.g. settled larvae or zooplankton captured by a benthic predator). Forces on bodies attached to a substratum were measured with a small lip on the substratum to prevent flow between the model and the substratum, as described in the Methods. Effects of body shape on forces can be assessed by comparing C_D's and C_L's for those shapes that operated at the same Re (Table 1.1A), while the possibility of being washed off a surface is better represented by the actual forces on organisms subjected to ambient water flow (examples in Figs 1.7 and 1.8).

Body shape only affected hydrodynamic forces on animals on surfaces under a few

conditions. When on a substratum at Re $\approx$ 1700, the copepod shape had a significantly lower C_D than did the cyprid shape when at right angles to the flow, but not when facing upstream (Table 1.1A). Although body shape affected drag coefficients in faster flow, shape did not affect vertical or side lift coefficients on bodies on a substratum. No significant effects of antennal configuration on C_D's or C_L's were found for the copepod on a surface at Re $\approx$ 1700 for any body orientation relative to the flow (Table 1.2A).

Examples of the effects of some body orientations on the hydrodynamic forces experienced by animals of different shapes on surfaces in an ambient water current of 1.6 m/s are shown in Figs 1.7A, C, E, G, I and 1.8A. For each body shape, there was no significant difference between anterior and posterior orientations (T-test, $p>0.05$) or between dorsal and ventral orientations (T-test, $p>0.05$). An example of the forces in all eight tested orientations are shown for the copepod with retracted antennae on a surface in Figure 1.8,A. Forces on the cyprid were the largest, followed by those on the copepod, especially when its antennae were extended laterally. In contrast, forces on the nauplius and veliger were much lower. Orientation had no effect on drag or side lift for the nearly-spherical veliger, whereas vertical lift was significantly larger when the veliger was anterior to the flow (ANOVA, Tukey, $p<0.05$). In contrast, the drag on the flatter nauplius was higher when it had its ventral surface facing upstream than when its anterior end was facing upstream, while orientation had no effect on vertical or side lift (ANOVA, Tukey, $p<0.05$). The cyprid experienced higher drag when lateral to the flow than in any other orientation (ANOVA, Tukey, $p<0.05$), whereas vertical and side lift were unaffected by orientation. Drag on the copepod with extended antennae was unaffected by orientation. In contrast, drag on the copepod with its antennae bent along the sides of the body was different for each orientation and was greater when the body axis was at right angles to the flow than when parallel (ANOVA, Tukey, $p<0.05$). In contrast, the vertical lift on the copepod, both with antennae extended and with antennae bent along the body, was unaffected by orientation (ANOVA, Tukey, $p<0.05$). Side lift, however, was significantly greater when the copepod was ventral to the flow for both configurations of the antennae (ANOVA, Tukey, $p<0.05$). Thus, the effects of body orientation on drag and lift depended on body shape and configuration.

Effect of body shape on moments when mid-water

The models of zooplankton experienced moments as they moved through the fluid, and body shape affected the coefficients of roll (C_R), pitch (C_M), and yaw (C_N) on the animals in mid-water (Table 1.3B). The pitch coefficient (C_M) was smaller for the nauplius than for the more elongate cyprid and copepod at Re$\approx$800 when they were oriented with their anterior ends facing upstream. When they were oriented with their long axes perpendicular to the flow at Re of $\approx$800, the cyprid had a larger yaw coefficient (C_N) than both the copepod and nauplius. At the higher Re of $\approx$1700, the cyprid had a larger C_M and C_N than did the copepod when their long axes were perpendicular to the direction of fluid motion, both when lateral or ventral to the flow. The cyprid also had a higher roll coefficient (C_R) than the copepod when lateral to the flow at

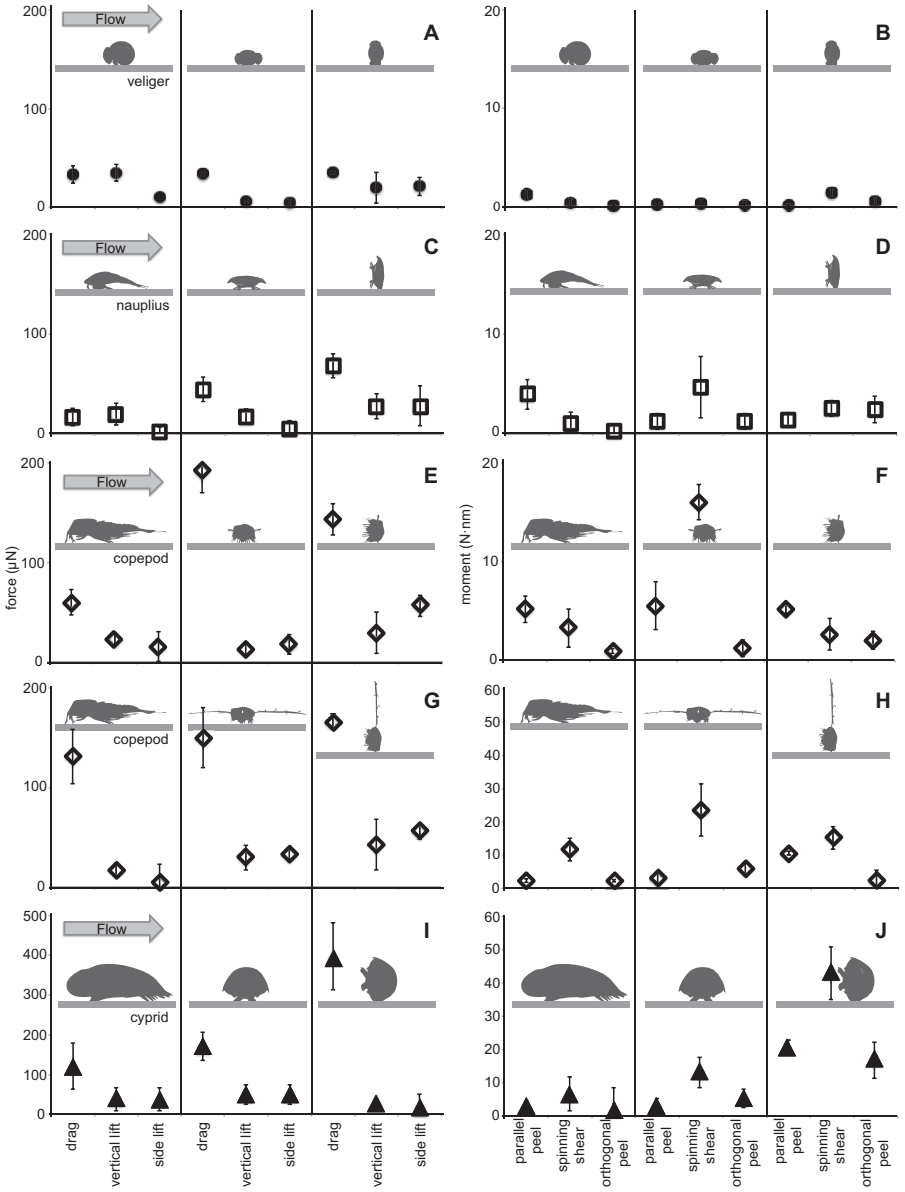

Figure 1.7: Graphs of forces and moments for all animals on a surface in three orientations relative to the direction of water flow past the body (anterior, lateral, and ventral). Forces and moments measured on the models were used to calculate the forces and moments on the real animals on a surface exposed to an ambient water current of 1.6 m/s. Forces (A) and moments (B) for the veliger. Forces (C) and moments (D) for the nauplius. Forces (E) and moments (F) for the copepod with antennae folded. Forces (G) and moments (H) for the copepod with antennae extended laterally. Forces (I) and moments (J) for the cyprid. All force graphs use the same scale, except for that of the cyprid. The moment graphs of the cyprid and copepod with extended antennae use a different scale from the other moment graphs. Grey arrow shows flow direction relative to the models (grey diagrams).

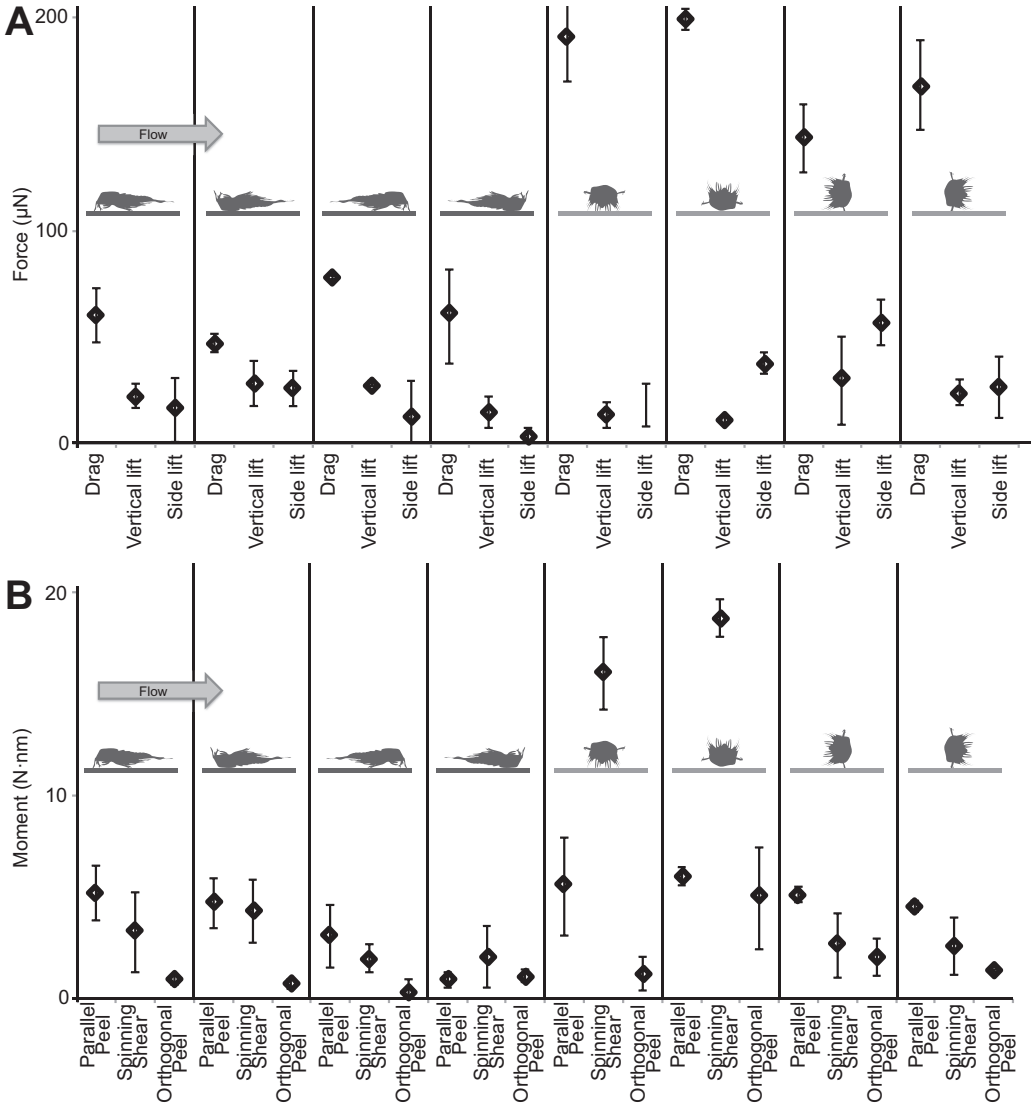

Figure 1.8: Graphs for all eight tested orientations of copepod with folded antennae. Forces and moments measured on the models were used to calculate the forces (A) and moments (B) on the real copepods on a surface exposed to an ambient water current of 1.6 m/s. Grey arrow shows flow direction relative to the models (grey diagrams).

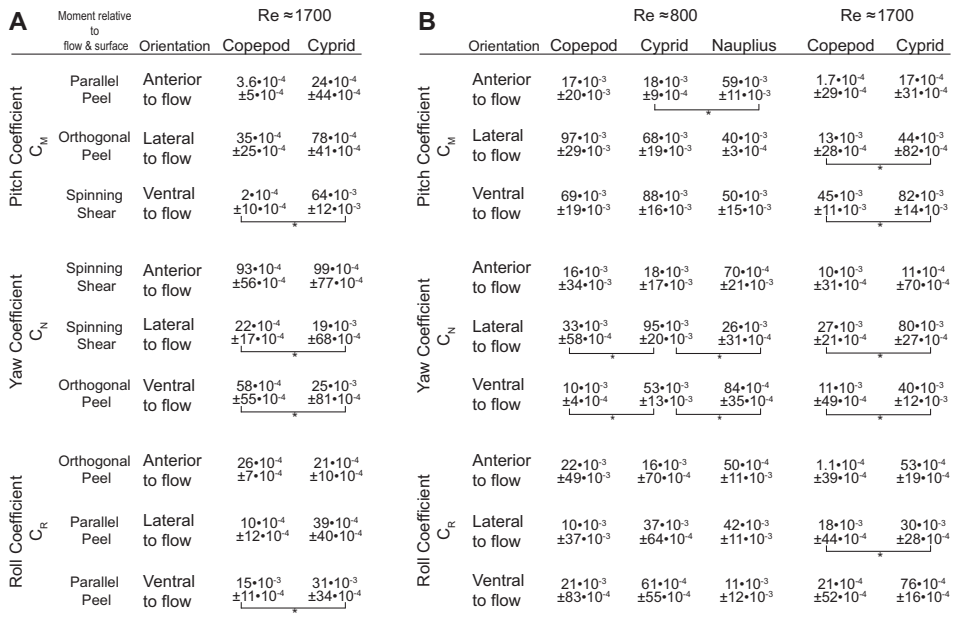

Table 1.3: Comparisons of the moment coefficients of different body shapes for animals on a surface (A) and for animals mid-water (B) (see Fig. 2 for illustrations of the moments). In Table A, when animals were oriented anterior to the flow, pitch coefficient (Eqn. 1.4) were used when comparing parallel peel, the yaw coefficient (Eqn. 1.6) when comparing spinning shear, and the roll coefficient (Eqn. 1.5) when comparing orthogonal peel. When the animals were lateral to the flow, roll coefficient were used to compare parallel peel, the yaw coefficient to compare spinning shear, and the pitch coefficient to compare orthogonal peel. When the animal was ventral to the flow, roll coefficient were used to compare parallel peel, the pitch coefficient to compare spinning shear, and the yaw coefficient to compare orthogonal peel. Brackets labeled with an asterisk indicate significant difference (ANOVA-Tukey, $p<0.05$ for significance when three shapes are compared at a given Re; t-tests, $p<0.05$ when two shapes are compared at a given Re).

Re≈1700.

The configuration of the long antennae of the copepod not only affected drag and lift coefficients, but also affected the moment coefficients under some circumstances (Table 1.4B). At the higher Re≈1600, extended antennae increased the pitch coefficient when the copepod was facing upstream. Extended antennae also increased the yaw coefficient (C_N) when the animal was lateral to the flow at both Re's tested: Re≈1600, and Re≈800. In contrast, roll coefficients (C_R) were unaffected by the configuration of the antennae for all orientations of the copepod when mid-water.

Effect of body shape and orientation on moments when on a substratum

The effects of body shape and orientation on the hydrodynamic moment coefficients

A

	Moment relative to flow & surface	Orientation	Re ≈1700 Extended	Re ≈1700 Folded
Pitch Coefficient C_M	Parallel Peel	Anterior to flow	$2.5 \cdot 10^{-3} \pm 77 \cdot 10^{-4}$	$35 \cdot 10^{-4} \pm 24 \cdot 10^{-4}$
	Orthogonal Peel	Lateral to flow	$17 \cdot 10^{-3} \pm 42 \cdot 10^{-4}$	$40 \cdot 10^{-4} \pm 50 \cdot 10^{-4}$ *
	Spinning Shear	Ventral to flow	$43 \cdot 10^{-3} \pm 98 \cdot 10^{-4}$	$20 \cdot 10^{-4} \pm 10 \cdot 10^{-3}$ *
Yaw Coefficient C_N	Spinning Shear	Anterior to flow	$33 \cdot 10^{-3} \pm 96 \cdot 10^{-4}$	$93 \cdot 10^{-4} \pm 56 \cdot 10^{-4}$ *
	Spinning Shear	Lateral to flow	$67 \cdot 10^{-3} \pm 22 \cdot 10^{-3}$	$22 \cdot 10^{-4} \pm 17 \cdot 10^{-4}$ *
	Orthogonal Peel	Ventral to flow	$68 \cdot 10^{-4} \pm 91 \cdot 10^{-4}$	$58 \cdot 10^{-4} \pm 55 \cdot 10^{-4}$
Roll Coefficient C_R	Orthogonal Peel	Anterior to flow	$66 \cdot 10^{-4} \pm 31 \cdot 10^{-4}$	$26 \cdot 10^{-4} \pm 6 \cdot 10^{-4}$
	Parallel Peel	Lateral to flow	$62 \cdot 10^{-4} \pm 79 \cdot 10^{-4}$	$10 \cdot 10^{-4} \pm 12 \cdot 10^{-4}$
	Parallel Peel	Ventral to flow	$30 \cdot 10^{-3} \pm 16 \cdot 10^{-4}$	$15 \cdot 10^{-3} \pm 11 \cdot 10^{-4}$ *

B

	Orientation	Re ≈800 Extended	Re ≈800 Folded	Re ≈1700 Extended	Re ≈1700 Folded
Pitch Coefficient C_M	Anterior to flow	$48 \cdot 10^{-3} \pm 15 \cdot 10^{-3}$	$17 \cdot 10^{-3} \pm 20 \cdot 10^{-3}$	$11 \cdot 10^{-3} \pm 40 \cdot 10^{-4}$	$17 \cdot 10^{-4} \pm 29 \cdot 10^{-4}$ *
	Lateral to flow	$13 \cdot 10^{-3} \pm 46 \cdot 10^{-3}$	$97 \cdot 10^{-3} \pm 29 \cdot 10^{-3}$	$20 \cdot 10^{-3} \pm 69 \cdot 10^{-4}$	$14 \cdot 10^{-3} \pm 28 \cdot 10^{-4}$ *
	Ventral to flow	$113 \cdot 10^{-3} \pm 33 \cdot 10^{-3}$	$69 \cdot 10^{-3} \pm 19 \cdot 10^{-3}$	$65 \cdot 10^{-3} \pm 27 \cdot 10^{-3}$	$45 \cdot 10^{-3} \pm 11 \cdot 10^{-3}$
Yaw Coefficient C_N	Anterior to flow	$29 \cdot 10^{-3} \pm 80 \cdot 10^{-3}$	$16 \cdot 10^{-3} \pm 34 \cdot 10^{-3}$	$10 \cdot 10^{-3} \pm 17 \cdot 10^{-3}$	$11 \cdot 10^{-3} \pm 33 \cdot 10^{-4}$
	Lateral to flow	$78 \cdot 10^{-3} \pm 57 \cdot 10^{-4}$	$4 \cdot 10^{-4} \pm 58 \cdot 10^{-3}$ *	$49 \cdot 10^{-3} \pm 14 \cdot 10^{-3}$	$27 \cdot 10^{-3} \pm 22 \cdot 10^{-4}$ *
	Ventral to flow	$32 \cdot 10^{-4} \pm 26 \cdot 10^{-3}$	$10 \cdot 10^{-3} \pm 36 \cdot 10^{-4}$	$32 \cdot 10^{-4} \pm 44 \cdot 10^{-4}$	$11 \cdot 10^{-3} \pm 49 \cdot 10^{-4}$ *
Roll Coefficient C_R	Anterior to flow	$30 \cdot 10^{-3} \pm 56 \cdot 10^{-3}$	$22 \cdot 10^{-3} \pm 48 \cdot 10^{-3}$	$32 \cdot 10^{-4} \pm 16 \cdot 10^{-4}$	$1 \cdot 10^{-4} \pm 40 \cdot 10^{-4}$
	Lateral to flow	$37 \cdot 10^{-3} \pm 26 \cdot 10^{-3}$	$10 \cdot 10^{-3} \pm 37 \cdot 10^{-3}$	$16 \cdot 10^{-3} \pm 31 \cdot 10^{-4}$	$18 \cdot 10^{-3} \pm 41 \cdot 10^{-4}$
	Ventral to flow	$20 \cdot 10^{-3} \pm 48 \cdot 10^{-4}$	$21 \cdot 10^{-3} \pm 76 \cdot 10^{-4}$	$4 \cdot 10^{-4} \pm 41 \cdot 10^{-4}$	$23 \cdot 10^{-4} \pm 53 \cdot 10^{-4}$

Table 1.4: Comparisons of the moment coefficients of different antennal configurations for copepods on a surface (A) and mid-water (B). In Table A, when animals were oriented anterior to the flow, pitch coefficient (Eqn. 1.4) were used to compare parallel peel, the yaw coefficient (Eqn. 1.6) to compare spinning shear, and the roll coefficient (Eqn. 1.5) to compare orthogonal peel. When the animals were lateral to the flow, roll coefficient were used to compare parallel peel, the yaw coefficient to compare spinning shear, and the pitch coefficient to compare orthogonal peel. When the animal was ventral to the flow, roll coefficient were used to compare parallel, the pitch coefficient to compare spinning shear, and the yaw coefficient to compare orthogonal peel. Brackets labeled with an asterisk indicate significant difference (t-tests, $p<0.05$).

of zooplankton when on a substratum at Re≈1700 are summarized in Table 1.3A. The spinning shear on the cyprid was greater than that on the copepod when the animals were at right angles to the flow (C_M when ventral to the flow, and C_N when lateral to the flow). Likewise, when the animals were ventral to the flow, the orthogonal peel (C_N) and the parallel peel (C_R) was greater on the cyprid than on the copepod.

The effects on moment coefficients of the configuration of the long antennae of a copepod on a substratum at Re≈1700 are given in Table 1.4A. Extending the antennae laterally increased the orthogonal peel coefficient only when the copepod was oriented lateral to the flow, and increased the parallel peel coefficient only when the copepod was oriented ventral to the flow. The effects of antennal configuration on spinning shear coefficients were the most striking, with greater coefficients in every orientation when the antennae were extended.

Examples of the effects of some body orientations on the hydrodynamic moments experienced by animals of different shapes on surfaces in an ambient water current of 1.6 m/s are shown in Figures 1.7B, D, F, H, J and 1.8B. For each body shape, there was no significant difference between anterior and posterior orientations (T-test, $p>0.05$) or between dorsal and ventral orientations (T-test, $p>0.05$) with respect to the flow, so for simplicity only three orientations are shown in Fig. 1.7. In addition, an example of the moments in all eight tested orientations are shown for the copepod with retracted antennae on a surface in Fig. 1.8B. Moments on the cyprid and copepod were generally greater than on the veliger and nauplius. Both the veliger and the nauplius experienced greater parallel peel when anterior to the flow, but the spinning shear on the animals was unaffected by orientation (ANOVA, Tukey, $p<0.05$). In contrast, both parallel peel and spinning shear were greatest for the cyprid when the animal was oriented ventral to the flow (ANOVA, Tukey, $p<0.05$). In the case of the copepod, antennal configuration affected which orientations experienced the greatest moments. Spinning shear was greatest for the copepod with retracted antennae when the animal was lateral to the flow, while parallel peel was greatest for the copepod with extended antennae when the animal was ventral to the flow. Otherwise the moments on the copepod were unaffected by orientation (ANOVA, Tukey, $p<0.05$). Orthogonal peel was unaffected by orientation for all the body shapes studied. (ANOVA, Tukey, $p<0.05$). Thus, as with hydrodynamic forces, the effects of body orientation on the moments that could peel a zooplankter off the substratum depend on the shape and configuration of the animal.

Consequences of being near or attached to a substratum

The effects of being mid-water versus near or on a substratum are illustrated for zooplankters of different shapes when broadside to the flow direction (Fig. 1.9) and when facing upstream (Fig. 1.10). The two-dimensional resultant force between vertical lift and drag is plotted for animals on or near surfaces exposed to an ambient current of 1.6 m/s, and compared with those of animals moving through open water at the same Re. The near surface experiments were conducted with a gap between the substratum and animal of approximately 1/10 the body length of the animal. It is noteworthy that the greatest resultant force was often when the animal was near but not on the surface. In addition, the contribution of vertical lift consistently increased when animals that were facing upstream moved from the water column to near a surface, and then landed on the surface. In contrast, the contribution of vertical lift to the resultant force on a zooplankter was not affected by the substratum if the animal was oriented with its body axis at right angles to the flow direction.

DISCUSSION

Effects of body shape and orientation on fluid dynamic forces at intermediate Reynolds number

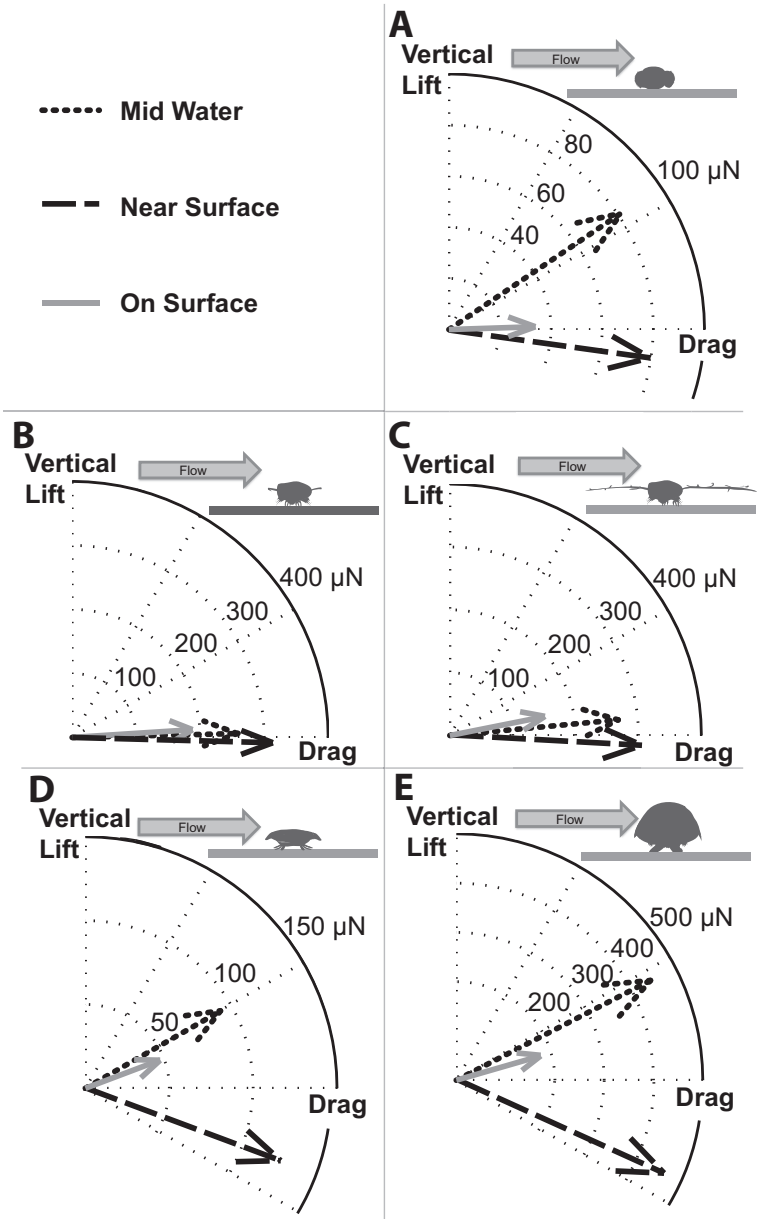

Figure 1.9: Graphs of force vectors that are the resultant of vertical lift and drag when animals were lateral to the flow direction and were mid-water (dotted vectors), near a surface (dashed vectors) and on a surface (solid vectors). The scale varies between graphs. A) veliger; B) copepod with retracted antennae; C) copepod with extended antennae; D) nauplius; and E) cyprid. Grey arrow shows flow direction relative to the models (grey diagrams). Vertical lift is defined normal to the surface.

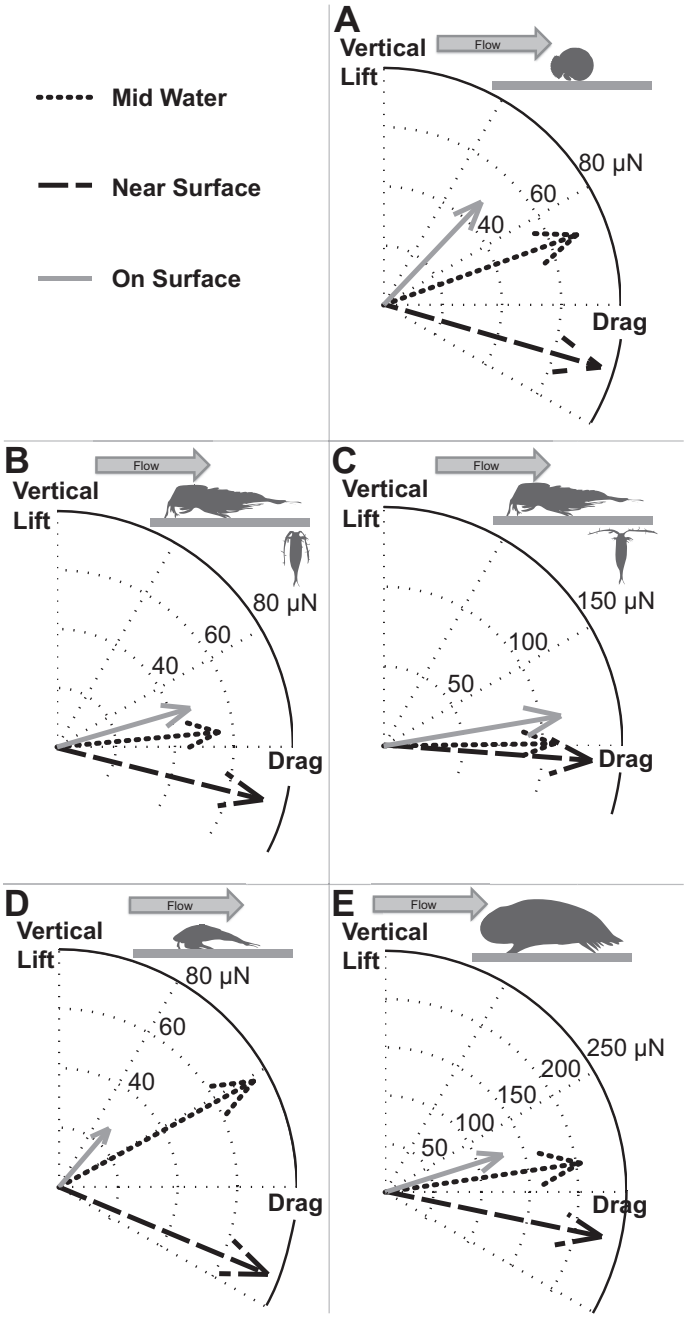

Figure 1.10: Graphs of force vectors that are the resultant of vertical lift and drag when the animals were facing upstream and were mid-water (dotted vectors), near a surface (dashed vectors) and on a surface (solid vectors). The scale varies between graphs. A) veliger; B) copepod with retracted antennae; C) copepod with extended antennae; D) nauplius; and E) cyprid. Grey arrow shows flow direction relative to the models (grey diagrams). Vertical lift is defined normal to the surface.

Fluid dynamic forces acting on aquatic animals were studied in an intermediate range of Reynolds numbers (Re $\sim$ 10^2 to 10^3) at which both viscous and inertial forces are important, and for which the effects of body shape and orientation are still poorly understood. Although planktonic animals are often approximated as spheres or cylinders, it was found that their drag coefficients (C_D) depended on body shape and orientation (Fig. 1.6). When the animals were oriented lateral to the flow, they behaved like bluff bodies with drag coefficients mostly between those of a cylinder and sphere in the same Re range, both when they were mid-water and when they were on a surface (Fig. 1.6A, C). In contrast, when the copepod (Re$\approx$1700) was facing upstream, both in mid-water and on a surface, it had a lower C_D than did a sphere or the less-streamlined cyprid at similar Re's (Fig. 1.6B, D). This suggests that pressure is an important component of drag at Re's of order 10^3, and that wake-reducing shapes can lower C_D's. However, when animals were facing upstream in mid-water at lower Re's of order 10^2, the drag-reducing effect of the streamlined shapes of the copepod and nauplius was small. This finding is consistent with reported effects of streamlining at low Re, which in fact increases drag by creating more surface area that is affected by shear (Vogel, 1996). The exception to this was that the quite low profile of the nauplius when facing upstream on a surface at a Re$\approx$800 that did lead to a lower C_D than that of a sphere (Fig. 1.6D). Conversely, at Re$<$500 the bulbous veliger with its protruding velar lobes had higher C_D's than a sphere when mid-water, and similar C_D's when on a surface (Fig. 1.6).

Our data show that fluid dynamic drag, lift, and moments on organisms are also more likely to be affected by body shape, configuration, and orientation at Re's of order 10^3 than at Re's of order 10^2. For example, the bulkier shape of the cyprid resulted in larger drag, lift, and spinning shear than did the more streamlined shape of the copepod at Re$\approx$1700, but not at Re$\approx$800. This suggests that body shape has little effect on hydrodynamic forces on zooplankton when swimming mid-water (generally at Re's $\leq$ 10^2) (Tables 1.1B, 1.3B). For example, the "hopping" escape response of copepods occurs at a Re of $\sim$800 (Strickler, 1975; van Duren and Videler; 2003). Our data show that when a copepod is facing upstream (the body orientation relative to the flow during a hop; Borazjani et al., 2010), the configuration of the long antennae does not affect the hydrodynamic forces or moments at that Re (Tables 1.2B, 1.4B). In contrast, body shape and orientation can be important when zooplankton experience rapid water flow, such as when exposed to fast ambient currents after capture on the tentacle of a benthic predator (e.g. Robinson et al., 2014) or after landing on the substratum (e.g. Ableson and Denny, 1997; Schiel, 2004; Koehl, 2007) (Tables 1.1A, 1.2A, 1.3A, 1.4A). The complex effects of body shape on the forces and moments on microscopic animals should affect the ability of predators to hold on to different types of captured zooplanktonic prey, and should influence the patterns of settlement of larvae, ranging from nearly-spherical veligers (e.g. Reidenbach et al, 2011) to elongated ascidian tadpoles (McHenry et al., 2003; Osman and Whitlatch, 2004), onto substrata exposed to ambient water currents.

Effects of the substratum on fluid dynamic forces on small organisms

As animals in the Re range of 10^2 to 10^3 approach and land on a substratum, the fluid dynamic forces on them change. For example, as illustrated in Figures 1.9 and 1.10, the relative importance and the sign of vertical lift, and hence the direction of the resultant hydrodynamic force on an animal, was affected by the substratum. In open water, the vertical lift force for all body shapes was positive (i.e. acts in the dorsal direction) and was always a third or less of the magnitude of the drag force. In contrast, when an animal neared the substratum, the vertical lift was negative, drawing the animal towards the substratum. Negative lift occurred when our models were very near a surface because water flowed more rapidly through the narrow gap between the body and the substratum than around the rest of the body, thereby causing a lower pressure on the substratum-facing side of the organism. After an animal landed on a surface, the vertical lift once again became positive, but its magnitude was greater than when the animal was mid-water. In a few instances (e.g. veliger and nauplius facing upstream), the vertical lift on animals on surfaces was as large as the drag (Fig. 1.10A, D). For all body shapes, the largest contributions of vertical lift to the resultant force on an animal on a surface occurred when the animal had its long axis parallel to the flow. Thus, when an animal faced upstream or downstream, it tended to be sucked up off the substratum more than when it was broadside to the flow direction, while an animal broadside to the flow tended to be pushed downstream more than when it was parallel to the flow.

Not only did the direction of the net hydrodynamic force on an animal change when near or on a substratum, but so did the magnitude of the force. As animals neared a surface, the resultant force increased, but after they landed the force decreased, often by more than twofold. The consequences of these changes in force magnitude and direction when zooplankton are near versus on surfaces should be considered when analyzing the mechanisms of capture of zooplankton prey by benthic predators and when considering how larvae settle on and explore surfaces. Any situation that leaves a small gap between the animal and the surface (such as when barnacle cyprid larvae "walk"; Aldred et al. 2013) should cause much larger hydrodynamic forces on the animal and should orient the net force towards the surface.

Are small animals pushed or twisted off surfaces by flowing water?

When animals of various shapes are on a surface exposed to flowing water, they experience forces that can push them off the surface, and they experience moments that can shear or peel them off the surface (Figs 1.7, 1.8). To compare the relative importance of forces and moments in detaching organisms from surfaces, the effects of drag (the largest component of hydrodynamic force on the animals I studied) and spinning (the largest moment on the animals) on the attachment of an animal to a surface were compared. Both drag and spinning impose shear stress on the material sticking an animal to a surface, so I compared the magnitude of the shear stress generated by

drag versus by spinning. An infinitesimal attachment area was considered that was located perpendicular to the direction of force at a distance from the center of mass of the body equal to the moment arm of spinning for that body. The shear stress due to drag is given by

$$\tau_{Drag} = F_D/\Delta A \tag{1.15}$$

and the shear stress due to spinning is given by

$$\tau_{Spin} = M_N/r/\Delta A \tag{1.16}$$

where F_D is the measured drag force, ΔA is the infinitesimal attachment area, M_N is the measured spinning moment, and r is the moment arm length. By taking the ratio of these two calculated shear stresses it was found for all the body shapes tested that the magnitude of the shear stresses due to spinning at the body orientation that produced the largest spinning shear were only 15 to 50% of the magnitude of the shear stresses caused by drag. Therefore, it appears that hydrodynamic forces rather than moments make the biggest contribution to shearing small organisms off surfaces. Furthermore, the drag forces measured on a cyprid exposed to a 1.6 m/s current were an order magnitude larger than the force to detach the animal as calculated by Eckman et al. (1990), suggesting that barnacle larvae attach to rocky shores in microhabitats subjected to slower flow or attach during periods of the tidal cycle when flow is slower..

In conclusion, our study showed for small animals operating at intermediate Reynolds numbers that body shape, configuration, and orientation have bigger effects on fluid dynamic forces and moments at Re's of order 10^3 than at lower Re's. It was also found that the magnitude and direction of the net force on an organism can change drastically as it nears, and then lands on a surface, and that organisms attached to surfaces are more likely to be pushed than twisted off the surface by flowing water.

ACKNOWLEDGEMENTS

This research was supported by a National Science Foundation IGERT Traineeship (to T. Dolinajec), IGERT Grant #DGE-0903711 (to R. Full, M. Koehl, R. Dudley, and R. Fearing), and by NSF Grant #IOS-1147215 (to M. Koehl). For technical assistance, I thank Amy Lyden and Rebecca Tjoelker, students participating in the Undergraduate Research Apprenticeship Program at the University of California, Berkeley.

2

Liberation of fungal sporocarps off of fluttering leaves: the importance of aeroelastic forces and overturning moments

KEYWORDS

phytopathogens, abscission, Erysiphales, fungal biomechanics, intermediate Reynolds number, Phyllactinia, adhesive force

HIGHLIGHTS

- Unsteadiness created by turbulent wind and fluttering leaves strongly suggest that sporocaprs are exposed to full velocity of wind gusts
- Median adhesive force of mature sporocarps to leaves is $\sim$50 μN
- Inertial forces, aeroelastic shedding, and aerodynamic forces are not supported as mechanisms of sporocarp liberation
- Overturning caused by pitching moment on sporocarp is supported as mechanism of sporocarp liberation
- Greater percentages of sporocarps are liberated at faster wind speeds and towards the tips of leaves, and the liberation rate in wind is 10^6 times that in still air

INTRODUCTION

Many small organisms or the microscopic propagules of sessile organisms achieve a transition off of a solid surface and into an adjacent moving fluid. The size and ambient fluid flow velocities experienced by these organisms places them within a physical regime in which both fluid dynamic inertial forces and viscous forces are salient, and in which the interface between solid and fluid is characterized by a velocity gradient of the same order of magnitude in height as the size of the organism or propagule (Vogel, 1996). This regime is described as operating at an intermediate Reynolds number (Re), where the ratio of inertial forces to viscous forces for a given flow situation is given by Re,

$$Re = UL/\nu \tag{2.1}$$

where U is the velocity of the fluid relative to the organism, L is a characteristic linear dimension of the organism (body radius in this study), and ν is the kinematic viscosity of the fluid.

The biologically important process of leaving a surface and entering the flow can be observed in microscopic aquatic organisms such as larvae and copepods being detached from the feeding surfaces of predators (e.g. Shimeta and Jumars, 1991; Robinson et al., 2013), unsuccessful settlement of larvae onto the substratum (e.g. Abelson and Denny, 1997; Koehl and Hadfield, 2010), and failed disposition of seagrass pollen (e.g. Ackerman, 1997; Haugen and Kragset, 2010). The dispersal of terrestrial propagules begins with release (reviewed in Alve, 1999; Zimmer et al. 2009), which includes seed abscission (e.g. Schippers and Jongejans, 2005; Kuparinen, 2006; Martinez-Berdeja et al., 2014), pollen shedding (e.g. Niklas, 1985; Ackerman, 2000), and fungal spore liberation (e.g. Ingold, 1965; Skotheim and Mahadevan, 2005).

An organism's trajectory away from a surface can be a result of stored metabolic energy within the organism as in the case of muscles, stored viscoelastic energy as in the case of pollen catapults (e.g. Edwards et al., 2005), Equisetum spores (e.g. Marmottant et al., 2013), and some fungal sporangia (reviewed in Forterre, 2013), stored energy in the form of turgor pressure as in the case of ascomycete fungi (e.g. Roper et al., 2010; Fritz et al., 2013), or stored water-tension energy in condensing and coalescing droplets as in the case of basidiomycete fungi (e.g. Pringle at al., 2005; Noblin et al., 2009). Passing vertebrate and invertebrate animals can also physically remove microscopic organisms or propagules from a surface (reviewed in Money and Fischer, 2009), and similarly animals can create mechanical vibrations that cause removal (e.g. King and Buchmann, 1995). The transition from contacting a surface to entering a moving fluid can also be mediated by the ambient fluid flow itself, either in the form of fluid dynamic forces acting directly on the organism, or through a flow-induced movement of the surface, which includes beating tentacles (e.g. Labarbera, 1984; Humphries, 2009) and fluttering leaves (e.g. Baker 1995).

Liberation mechanisms by airflow at intermediate *Re*

Wind is important in the life cycles of many plants (reviewed in de Langre, 2008), and approximately 10% of all angiosperms are wind pollinated (Friedman and Barrett, 2009). Some seeds that have an aerial phase are macroscopic, e.g. samaras (Salcedo et al., 2013) and dandelion seeds (Andersen, 1993), and their size and the wind velocities they experience prior to release place them at $Re \sim 10^3 - 10^4$ (5cm length for mahogany samaras and 0.8cm length for dandelion seeds, with a fresh breeze of 8 m/s). Such seeds have masses on the order of grams. However, many wind liberated seeds are nearly microscopic and dust-like (Okubo and Levin, 1989; Murren and Ellison, 1998), as are wind liberated pollen grains and fungal spores and packets of spores (sporocarps). Examples include orchid seeds of the genus *Orchis* that have diameters on the order of 500μm (Arditti and Ghani, 2000), conidia of the fungal cause of corn blight *Helminthosporium maydis* that have lengths of approximately 100μm (Aylor and Parlange, 1975), and the pollen of the wheat genus *Triticum* that have diameters of approximately 50μm (Hammer, 2005). When considering the same wind speed of 8 m/s prior to liberation these propagules are operating at *Re* of ∼20 to ∼200. These propagules have masses ranging from tens of nanograms to micrograms.

Considering the masses of pollen grains, fungal spores, and very small seeds, it is apparent that gravitational forces are not a satisfactory explanation of liberation, whereas they may be for seeds like samaras. Likewise, aerodynamic forces are much smaller for sub-millimeter propagules than for large airborne seeds, as defined by the drag equation:

$$F_d = 1/2 C_D \rho S_w U^2 \tag{2.2}$$

where C_D is the drag coefficient, ρ is the density of the fluid, S_w is the surface area of the propagule, and U is the wind speed. Although C_D increases as a function of decreasing *Re* below *Re* ≈1000 (White, 1974), drag's proportionality to area leads to very small forces for small objects. These small aerodynamic forces are made yet smaller by the existence of leaf boundary layers (Grace and Collins, 1976), and have lead to the term "pollen paradox" (reviewed in Jackson and Lyford, 1999), which refers to the gale-force winds required to produce air flow at the grain-level fast enough to cause entrainment. As Aylor (1975) points out, the conidia of *Helminthosporium maydis* are being liberated at wind speeds less than 25 m/s, despite velocity gradient calculations to the contrary.

The difficulty in arriving at quantifiable explanations of wind-induced spore and pollen liberation at intermediate *Re* has perhaps exacerbated the classification between active and passively liberated propagules. Actively liberated spores are defined as those that can become airborne independent of the speed and turbulent intensity of the wind, whereas passively liberated spores in dry air are those whose concentrations in air can be correlated with wind conditions (reviewed in Aylor, 1990). In fact, much of the literature focusing on active liberation does so within the context of mechanical triggers (e.g. Ingold, 1992; Fischer et al., 2004; Trail et al., 2005; Roper et al., 2008), while literature on passive wind-liberated spores discusses atmospheric concentrations

(e.g. Pady et al., 1965; Willocquet and Clerjeau, 1998; Ryley and Chakraborty, 2008). Published mechanical explanations for passive liberation do exist (e.g. Bainbridge and Legg, 1976; Timerman et al., 2014 and reviewed in Lacey, 1996), but the division between passive and active liberation largely persists. However, it is worth considering the combined effects of passive and active liberation for a single organism's propagules, with the fair assumption that one form of liberation does not necessarily preclude another.

Phyllactinia — model system for liberation with and without wind

The genus *Phyllactinia* is a true fungus in the phylum Ascomycota, commonly known as sac fungi, and in the order Erysiphales, commonly known as powdery mildews (Braun and Cook, 2012). Mildews in the Erysiphales are pleomorphic with both an asexual and a sexual state. The asexual propagules are the unicellular conidia, and the multicellular sexual spores or ascomata are known as chasmothecia (called a sporocarp in this study for wider recognition). Powdery mildews are plant parasites with the conidia having been shown to initiate and sustain the disease cycle, while sexual sporocarps bridge periods of harsh weather and a lack of foliage on the host plant (reviewed in Glawe, 2008). A large number of studies propose mechanisms for the liberation of conidia, which include largely passive wind-initiated processes such as aerodynamic forces (e.g. Clerk and Ankora, 1969; Grove, 1998) and fluttering leaves (Bainbridge and Legg, 1976). Significantly fewer studies have proposed mechanisms for the liberation of sexual sporocarps and the reason for this may be two fold. First, some species of powdery mildew have persistent sporocarps that stay anchored to a substrate of the host plant (e.g. Jarvis et al., 2002, Gadoury et al., 2010). Second, the fecundity of conidia and their small size means that their liberation occurs frequently and is achieved at a low force threshold. Conversely, sporocarps are not nearly as abundant as conidia, and have radii approximately two orders of magnitude larger than conidia. At least two genera of powder mildew, however, are known to include liberation of sporocarps from host leaves in their life cycles, *Erysiphe* and *Phyllactinia* (Gadoury and Pearson, 1988; Cook et al., 2006)

The size range of most sporocarps is 100 - 200 μm (Glawe, 2008), and, although drastically different in size from most conidia, basidiospores and individual ascospores, they are representative of a group of fungal propagules. These relatively large fungal and fungal-like units include the sporangia of downy mildews in the order Peronsporales, and the teliospores of rusts in the order Pucciniales. As with liberated sporocarps in the Erysiphales, sporangia attached to sporangiophores and teliospores may be liberated by the employment of hygroscopic movement (Slusarenko and Schlaich, 2003; Elbert et al., 2007). Piepenbring et al. (1998) points to the importance of flexibility in liberation strategies among the teliospores of rusts, a versatility that is shared by sporangia and sporocarps. Furthermore, sporocarps, sporangia, and teliospores alike are mostly found on the downward facing sides of foliage, seemingly taking advantage of gravity.

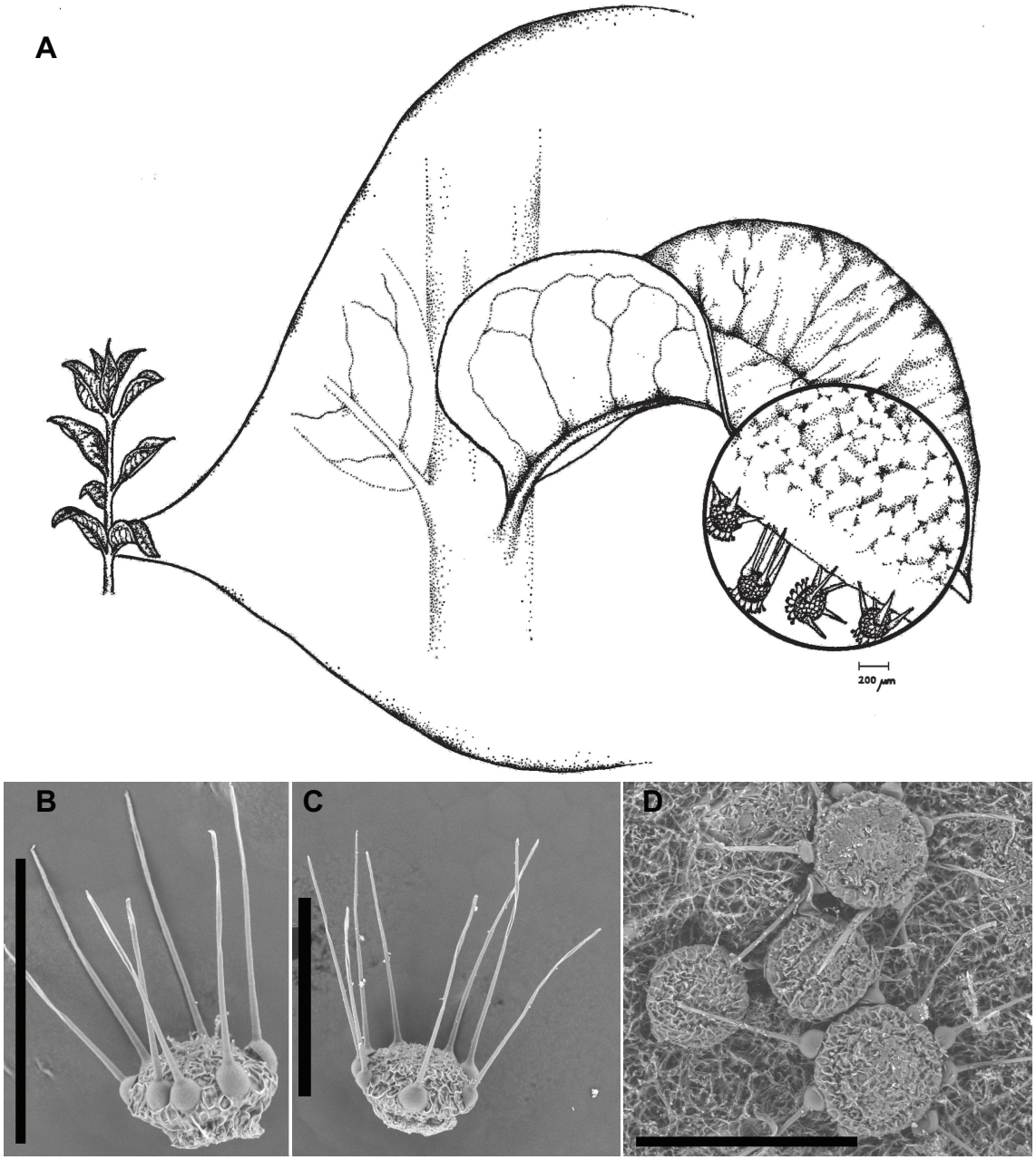

Figure 2.1: (A) Drawing of plant host *Calycanthus*, magnified infected leaf attached to stem, and *Phyllactinia* sporocarps on the bottom side of infected leaf. (B - C) Scanning electron microscope images of individual mature *Phyllactinia* sporocarps (following some desiccation). (C) Scanning electron microscope image of maturing sporocarps on host with radial appendages prior to bending. Scale bars 200 μm in (B - C) and 300 μm in (D). (art by Brittany Cummings)

The sporocarps of *Phyllactinia* are a rather captivating example of the powdery mildews. The body size of the sporocarp is typical of the order and depends on the species, but with little variation among a species (Glawe, 2006). The radial appendages of the sporocarp, however, are unique among the genera, and are often described as lance-like (Kumar and Gupta, 2004). The sporocarp also contains a second set of appendages located ventrally (Liberato, 2007), that are known as penicillate cells (Fig. 1). The penicillate cells are thought to aid in deposition following liberation and transport, and keep the sporocarp fixed during dehiscence (Itoi et al., 1962), and the radial appendages are hypothesized to have an aerodynamic purpose (Webster, 1979), but of particular relevance to this study is the function the radial appendages serve during liberation. The radial appendages have a pulpous base where they are connected to the body of the sporocarp, and it has been long established that the appendages bend during maturation (Neger, 1903). However, two hypotheses exist regarding the effect of the bending, with one suggesting the hygroscopic buckling causes a vaulting launch of the spore packet (Cullum and Webster, 1977), and the other postulating that drying and bending only serve to expose the spore packet to greater wind velocity (Alexopoulos et al., 1996). These two liberation mechanisms, either working in mutual exclusivity or in unison, make *Phyllactinia* a model organism for liberation with and without wind.

Aerodynamics forces and moments at intermediate Re in turbulent wind on a fluttering leaf

To understand the efficacy of wind-induced liberation of sporocarps the aerodynamics near a leaf need to be quantified, as do the dynamic effects of non-rigid fluttering of that leaf. A leaf can be naively approximated as a flat plate, with the Blasius solution offering a value for the height of the velocity gradient over the plate (Blasius, 1908), i.e. the boundary layer thickness:

$$\delta \approx \frac{4.91x}{\sqrt{Re_x}} \tag{2.3}$$

where x is the distance from the leading edge of the plate, and the characteristic length scale in Re_x is x. This entails boundary layer thicknesses in the range of 1 to 3 mm for leaves with lengths on the order of 10cm exposed to a fresh breeze of 8 m/s. Nobel (1975) has formulated a semi-empirical boundary layer height for a leaf-like object in air:

$$\delta \approx 0.0040\sqrt{\frac{x}{U_w}} \tag{2.4}$$

where U_w is the free-stream wind speed, which suggests thinner boundary layers in the range of 300 to 500 μm for the same sized leaves and strength breeze. In both these cases, and in particular the former, a mature sporocarp of *Phyllactinia* with an height of $\approx$250 μm would be fully embedded within the boundary layer (Fig. 2A). In such approximations the boundary layer is assumed to be laminar and have not transitioned

to a turbulent state. This is a reasonable assumption since the transition to a turbulent boundary layer across a flat plate should occur at $Re_x \approx 5 \times 10^5$ (Bergman et al., 2011), a Re_x value that is reached but not surpassed at the tip of a 10cm leaf in a 8 m/s breeze. The velocity of air flow experienced locally by a sporocarp is

$$U_L \approx 0.166 U_w \sqrt{Re_x}(h/x) \tag{2.5}$$

where h is the height of the spore (Schlichting, 1979; Urzay et al., 2009). The local

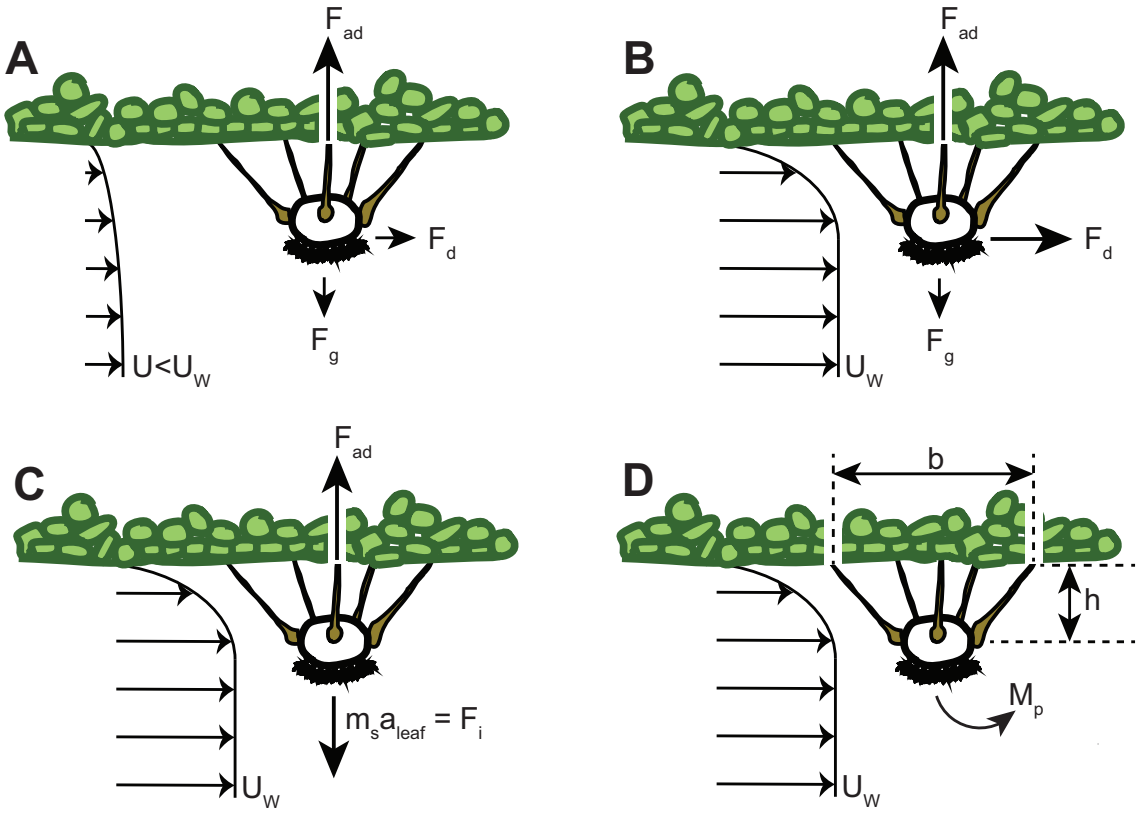

Figure 2.2: Diagrams showing (A) aerodynamic, gravitational, and adhesive forces acting on a sporocarp when embedded in a laminar boundary layer. (B - D) represent a sporocarp exposed to free-stream wind, with (B) showing aerodynamic, gravitational, and adhesive forces, (C) aeroelastic inertial and adhesive forces, and (D) aerodynamic pitching moment.

velocity for a sporocarp located in the middle of 10cm leaf is ≈1 m/s when the free-stream wind speed is 8 m/s. This results in a local Re of ∼13 (characteristic length set to sporocarp diameter). This low Re justifies the use of the steady Stokes drag force on a sphere in contact with a wall (O'Neill, 1968):

$$F_d = 1.7093(3\pi\mu D U_L) \tag{2.6}$$

where D is the diameter of the sporocarp, and μ is the dynamic viscosity of air, which is 1.85×10^{-5} Pa·s. This approach estimates drag forces acting on sporocarps of ∼60 nN.

Despite the robust associated theory, laminar flow over a flat plate is not a satisfactory approximation for wind over a leaf. Grace (1978) found that when the incident air flow to a leaf was made turbulent to resemble natural conditions that the transition to a turbulent boundary layer occurred at a much lower Re of 0.4×10^4, thus suggesting that boundary layers over leaves are always turbulent. In fact, leaf shapes, motion, orientation with respect to the wind, and roughness all tend to decrease the boundary layer thickness of a leaf (reviewed in Schuepp, 1993). The presence of leaf trichomes can also hasten the onset of turbulence if the average trichome height is $\geq 2\%$ of the leaf length (Schreuder et al., 2001). The effects of ambient turbulence on leaf boundary layers is well documented in the literature. Aylor and Parlange (1975), determined experimentally that gusts of wind could sweep over a section of leaf before the viscous boundary layer had time enough to grow. This fact is predicated on the no-slip condition between a solid and a fluid, and the resulting gradual development of a boundary layer where the height $\delta \sim \sqrt{\nu_{air} t}$ (Batchelor, 1967), with ν_{air} the kinematic viscosity of air at 1.57×10^{-5} m^2/s. For a gust to take advantage of the this viscous lag time it must operate on the order of 10^{-3} and 10^{-4}. Urzay et al. (2009) defines this parameter of turbulent gusts as the (inertial) gust time scale:

$$t_g = \delta_i / u' \tag{2.7}$$

where δ_i is the gust front thickness, and u' is the gust velocity fluctuations. The exact value of t_g will vary with the characteristics of a particular gust, but one experimentally obtained value is 0.4 ms (Aylor and Parlange, 1975). If the boundary layer height δ is set to the height of a sporocarp then the viscous time scale can be defined as

$$t_\nu = h^2 / \nu \tag{2.8}$$

and the ratio of the gust and viscous time scales is termed the Stokes-Reynolds number (Urzay et al., 2009):

$$\epsilon = t_\nu / t_g \tag{2.9}$$

If $\epsilon \leq 1$ then boundary layers should be equal to or larger than the height of the sporocarp, and if $\epsilon > 1$ then some or all of the sporocarp should be exposed to the free-stream wind velocity (Fig 2B).

Beyond deviations from an idealized flat plat and the effects of turbulence, the micro-scale flow accords a leaf can be affected by the movement of the leaf, i.e. fluttering. It has been suggested that wind agitation is required for pollen release from catkins (Faegri and van der Pijl, 1978), and even the liberation of mildew conidia has been correlated with shaking leaves (Bainbridge and Legg, 1976). Much of the literature covering the effect of high wind on leaves is focused on the consequences on the leaves themselves (reviewed in Vogel, 2009), but still have a bearing on organisms living

on wind-exposed leaves, such as the pronounced fluttering of poplar leaves (Roden and Pearcy, 1993). Recent studies on plant aerodynamics using particle image velocimetry have elucidated details such as larger oscillations brought about by a flexible tether or petiole (e.g. Miller et al., 2012). Research on the dynamics of flag flapping has obvious application to understanding leaf fluttering. Zhang et al. (2000) establishes that flexible filaments do not simply follow the vortexes shed upstream, but instead flap based on tension, elasticity and the mass of the filament. Furthermore, the typical frequency of flapping for a flag has been shown to be predictable based on physical characteristics (Argentina and Mahadevan, 2004). Of most direct relevance to the current study, the aeroelastic properties of a oscillating plant stamen have been quantified in relation to pollen shedding (Urzay et al., 2009). Congruently with the two time scales described in Eqn. 2.7 and 2.8, the kinematics of a vibrating anther can be expressed as

$$t_a = U_w / a_{rms} \tag{2.10}$$

with a_{rms} the root-mean square of the anther acceleration. This formulation leads to the concept of the probability of aeroelastic pollen shedding

$$P = e^{-\psi^2/2} \tag{2.11}$$

for which

$$\psi = \frac{F_{ad} t_a}{U_w m} \tag{2.12}$$

where ψ is termed the pollen shedding number, F_{ad} is the adhesive force of the pollen to the anther, and m is the mass of the pollen grain. With the replacement of a pollen grain with a sporocarp and an anther with a leaf, this theoretical approach can be applied to *Phyllactinia* liberation. The accelerations of a fluttering leaf can also be used to directly calculate the inertial force acting on a sporocarp at a given time using Newton's second law of motion and the average mass of a sporocarp. (Fig. 2C).

Research has been conducted on the hydrodynamic moments acting on zooplankton during settlement in a Re range similar to that of sporocarps on leaves (Abelson and Denny, 1997; de Montaudouin et al., 2003), with flow velocities reported but moments covered in a mostly qualitative manner. The principles outlining the biological importance of overturning have been discussed for arthropods in Alexander, (1971) and for stiff stemmed plants in Wainwright et al., (1976). Approaching the concept of overturning based on the critical flow velocity that initiates it, small animals like a blowfly are stated as having need for wider spaced legs and a less upright posture, because of the proportionality of the critical flow velocity to the animal profile height. Having legs spread well apart for the purpose of stability is postulated as more important for organisms in the surf than those exposed to wind due to the much greater density of water (Alexander, 1971; Martinez, 2001), but owing to the size range considered in these studied the drag coefficient (C_d) is considered to vary little with Re. However, the intermediate Re of sporocarp liberation suggests C_d significantly larger than those

for macroscopic animals, and increased importance of pasture and overturning.The approach taken in the study is a balancing of moments:

$$M_p = F_{ad} b \tag{2.13}$$

where b is the spread of radial appendages at the point of contact with the leaf (Fig. 2D), and M_p is the pitching moment:

$$M_p = 1/2 C_p \rho S U^2 R \tag{2.14}$$

where C_p is the pitch coefficient. The right-hand side of Eqn. 2.13 can effectively be thought of as the stability moment. Despite the potential importance of pitching over for sporocarps, to the best of the author's knowledge, neither the literature concerning pollen shedding nor the literature on spore liberation in wind discusses aerodynamic moments.

Adhesive force of spores and other biological particles

Measurements and estiments of adhesive force (F_{ad}) at the micron scale exists for a wide range of microscopic organism and propagules, but the reported values are scattered across phyla and length scales. Perhaps the most robust subfield of biological adhesive force research is that concerning bacteria adhesion, where spore diameters are on the order of $\sim 1 \mu$m and the method of adhesive force measurement is usually atomic force microscopy (e.g. Chung et al., 2010), or microfluidic flow chambers (e.g. de la Fuente et al., 2007). The magnitude of these adhesive forces range from 10^{-10} - 10^{-9} N. Boulbene et al., (2012) even go as far as to systematically address the hydrodynamic forces and moments that may overcome bacterial adhesive forces. However, due to the drastically different size scale and surface composition, it is unreasonable to attempt to scale any of the force measurements made on bacterial spores to fungal sporocarps.

Adhesive force measurements are scattered across the literature on pollen grains and fungal spores. Individual *Aspergillus* spore adhesion to mica was measured in the range of 40-90 nN using atomic force microscopy (Bowen et al., 2000). The adhesive force of insect-pollinated pollen grains with diameters on the order of 30μm is reported as $\sim$1nN as measured using a centrifugal method (King and Buchman, 1995). A similar centrifugal technique has been used by Aylor, (1975) who measured the adhesive force on leaves of large fungal conidia with a volume of 9.2×10^3 μm^3 at ~ 0.2 μN, and by Wright et al. (2002) who measured the adhesive force of the smaller conidia of *Blumeria* on barley leaves at a value of 4.9 nN. A common theme of the research on airborne propagule adhesion is that the force varies with maturation of the propagule and varies greatly among organisms. Despite the importance of establishing a range of adhesive forces to answer questions such as those that may resolve the pollen paradox, propagule adhesive forces remain poorly known quantities.

Objectives

The objective of this study was to address the mechanical mechanisms of liberation of a propagule in air at Reynolds numbers of ∼62 to 220 from a fluttering leaf. Liberation of sporocarps of the genus *Phyllactinia* were chosen to study for the above stated reasons, i.e. morphology varying with maturation, established active liberation mechanism, and established airborne transport. This study quantifies the importance of wind in the liberation of a propagule that is capable of liberate in the absence of wind. The specific hypotheses addressed were:

1) Mature sporocarps are liberated as a result of unsteady aerodynamic forces.

2) Mature sporocarps are liberated as a result of unsteady aerodynamic pitching moments.

3) Mature sporocarps are liberated as a result of aeroelastic inertial forces.

4) Location on a leaf and ambient wind speed affect the percent of sporocarps liberated.

5) Wind affects the rate of sporocarp liberation relative to the liberation rate in still air.

METHODS

This study involved field measurements, field collections, laboratory experiments using field collections, and physical modeling. All statistical methods specified in the results were carried out using Matlab 2012b.

Measuring wind and wind tunnel experiments

Wind speed in the field and in the lab was measured using a hot wire anemometer (Kurz series 2440 portable thermal anemometer, Kurz Instruments, Inc., Monterey CA). The analog signal from the anemometer was converted to a digital signal using an analog output circuit and a multifunction DAQ (NI USB-6009, National Instruments, www.ni.com), and recorded on a Windows PC using Matlab 2007b at a sampling rate of 60Hz. All wind speed records were taken for 45 seconds with field records timed to capture wind gusts or the lulls between gusts, and lab records timed to begin the moment the fan was powered on and end the moment the fan was powered off. Turbulent spectra were calculated using Matlab 2012b with the lowest frequency analyzed set at the inverse of 1/4 of the record time, or approximately 0.1Hz, and the highest analyzed frequency was that of the Nyquist frequency, or 15Hz in this case. Good agreement is shown between wind tunnel spectra and field gust spectra both in magnitude and slope (Fig. 2.3A), while the spectra of a breezy lull between gusts in the field is markedly different.

The wind tunnel was open circuit and open jet with a working section of 0.4m in diameter and custom built for previous research (Emerson and Koehl, 1990). The fan

was powered by an air circulator motor (model 4M197, Dayton Electric Co., Niles IL). The RPM of the fan was controlled by a variable transformer (Powerstat, Superior Electric Co., Bristol CT). The four wind speeds used in the wind-tunnel portion of this study represent the averages of multiple measurements along a 12cm × 4cm × 4cm grid that defined the experimental location. Two such experimental locations were used because only the highest wind speed of 9.4 cm/s only occurred at the second location (Fig. 2.3B).

Leaves of *Calycanthus* were individually placed at one of these two regions during an experiment. Leaves were fixed to a clip on a mounted clamp by their petiole and allowed to flutter freely downstream of the petiole (Fig. 2.3C). The small upstream clip was designed to have similar aerodynamic effects to those of upstream branches in a bush. A total of 39 leaves were subjected to a sweep of four sequential wind speeds of 4.9 ± 0.19 m/s, 6.7 ± 0.20 m/s, 7.4 ± 0.21 m/s, 7.4 ± 0.21 m/s (with the highest speed purposefully repeated). A smaller set of 16 leaves were subjected to a sweep of five wind speeds that included 9.4 ± 0.47 m/s following the other four speeds. These velocities were chosen to represent wind from a gentle breeze to a fresh breeze on the Beaufort scale (Oliver, 2005). The duration of each wind exposure was 45 seconds and included the time for the fan motor to reach full power. This method of using an ascending series of wind speeds is consistent with other leaf biomechanical studies (Vogel, 1989), and has the advantage of not damaging leaves with high wind before recording their kinematics at lower wind speeds. No leaf was ever used for more than one ascending set of wind speeds, and every leaf was used within 120 minutes of collection. No evidence of wilting was observed for any experimental leaf.

Leaves were filmed while fluttering with a high speed camera (Fastec Hispec 1 Color camera, fastecimaging.com) at 600 frames per second. Videos were collected on a Windows PC using proprietary software, and a set of ∼100 frames was exported as an image stack for offline analysis. This selection of frames representing 1/6 of a second of fluttering contained at least three full oscillations. Each set of frames was analyzed in ImageJ where the leaf tip location was tracked manually and the coordinates were used to calculate leaf accelerations. This tracking analysis was repeated for the the midline of each leaf 22% and 44% of the leaf-length upstream from the tip. The peak acceleration of each of the 516 combination of leaf, location on a leaf, and wind speed was calculated by averaging the three maximum downward accelerations. Aeroelastic time was calculated for leaf tip fluttering using Eqn. 2.10 with the root-mean square of the leaf acceleration. The typical flapping frequency was determined for each leaf as a non-rigid analog to a beam's resonant frequency, and was

$$\omega \approx \sqrt{\frac{\rho_{air} U_w^2}{\rho_{leaf} h_{leaf} L_{leaf}}} \tag{2.15}$$

where ρ_{air} was the density of air estimated as 1.18 kg/m^3, ρ_{leaf} was the density of the leaf estimated as 500 kg/m^3 (Iqbal et al., 2013), h_{leaf} was the thickness of the leaf measured at ∼2mm, and L_{leaf} was the measured length of the leaf (Argentina and

Mahadevan, 2004).

Weighing, measuring, and determining adhesive force of sporocarps

Sporocarps were collected with a paint brush off of freshly picked infected leaves and placed in groups of five to seven on wax paper. These samples of sporocarps were weighed on a micro balance (CP2-F Satorius, readability 1 μg, sartorius-intec.us). The average weight of sporocarps in each sample was calculated. The average across samples was taken as the average sporocarp mass. Sporocarps were collected and weighed this way from early October, 2014 through December, 2014, and no trend was observed.

Sporocarps diameters were measured from scaled photographs using ImageJ and taken through a stereomicroscope at 50x magnification (Wild Heerbrugg M5A, leica-microsystems.com). Body diameters were only recorded for those sporocarps that were a dark brown color and that had been liberated by scraping the upper side of the leaf, i.e. the side of the leaf on which sporocaprs do not grow. In this way only the dimensions of mature and readily liberated sporocarps were measured. A smaller sample of sporocarps were used to measure appendage lengths, with only appendages measured that showed no signs of damage. The diameters of radial appendages were measured using images taken with a scanning electron microscope (Hitachi TM-1000 SEM, Hitachi High Technologies America, Inc., hitachi-hta.com).

The adhesive force holding sporocarps to host leaves prior to liberation was measured using cantilever deflection (Fig. 2.3D). Encompassed under Euler-Bernoulli beam theory, a cantilever beam with an end load has the following relationship between its deflection length and load force:

$$\delta_c = \frac{F_{ad} L^3}{3EI} \tag{2.16}$$

where δ is the deflection distance, F_{ad} is the adhesive force of the sporocarp, L is the cantilever length, E is the Young's modulus, and I is the second moment of area of the cantilever (Gere and Timoshenko, 1997). Small glass fibers were used, measuring 4 to 11 mm in length, and 0.002 to 0.006 mm in diameter (boron-containing E-glass, Multi-Tech Products, Murrieta CA). The Young's modulus of this glass type was 77 GPa (Wallenberger et al., 2001). The glass fibers were approximately a circular cylinder and consequently $I = \pi D^4/64$, where D was the diameter of the fiber. The above Eqn. 2.4 was only applicable when $\delta/L \leq 0.10$, however, and not all of the experiments could meet that criteria. Thus, for proportionally larger deflections adhesive force was measured with the following equation instead:

$$F_{ad} = \frac{2 sin\theta EI}{\ell^2} \tag{2.17}$$

where θ is the angle at the free end where the load is applied, and ℓ is the bent length of the cantilever beam (Chen, 2010).

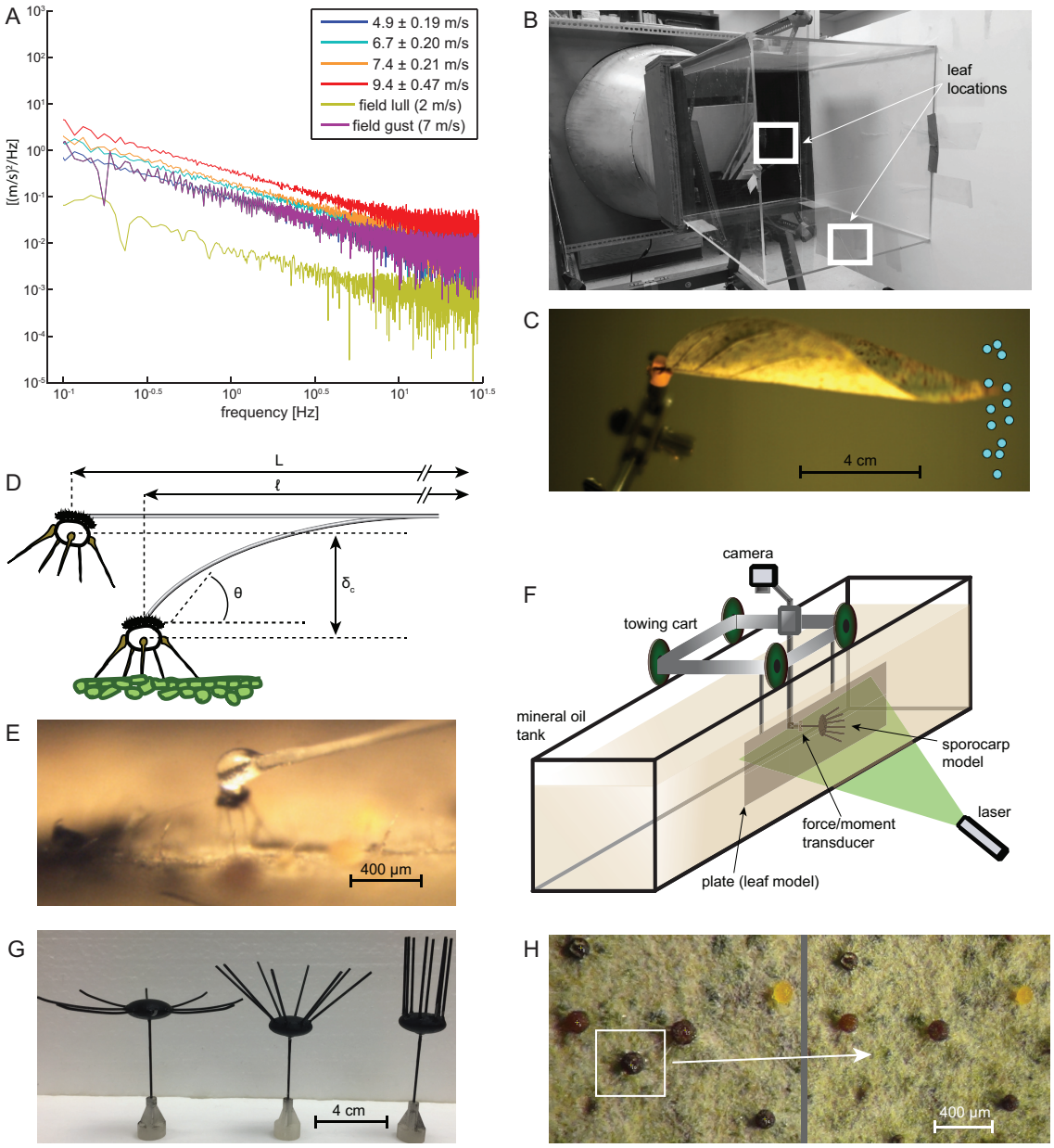

Figure 2.3: (A) Spectrum of turbulent wind in the field and recreated in a wind tunnel. (B) Wind tunnel showing the two locations leaf fluttering were recorded. (C) Fluttering leaf still image with cyan dots showing tracked tip locations. (D) Diagram indicating cantilever deflection measurements used to measure adhesive force (F_{ad}), see Eqn. 2.16 & 2.17. (E) Example of mature intact sporocarp with glass cantilever adhered by glue, and prior to F_{ad} measurement. (F) Tow tank used for dynamically scaled physical modeling. (G) Geometrically scaled sporocarp models. (H) Example of recorded sporocarp liberation in wind from infected leaf.

Deflections were conducted by applying a small amount of super glue to the tip of a glass fiber and then carefully bringing the glue-coated tip into contact with a mature attached sporocarp on the underside of a leaf. The leaf was fixed in place with clips and held with sporocarps facing horizontally for deflections normal to the leaf surface, and held with sporocarps facing upward for deflections parallel to the leaf surface. Fig. 2.3E shows an example of a fiber that has made contact with a sporocarp, and is being left in place for ~ 5 min while the glue is allowed to dry. After the glue had dried onto a sporocarp a micro manipulator with three degrees of freedom was used to retract the fiber in steps of $\sim 10\mu$m until liberation was observed. The incremental retraction was filmed through a dissecting microscope (Wild Heerbrugg M5A) by a video camera (Fastec Hispec 1). This way frames immediately before and after liberation could be analyzed to measure δ and thus calculate F_{ad} of individual sporocarps.

Dynamically scaled physical modeling and particle image velocimetry

Forces and moments were measured on dynamically scaled physical models of *Phyllactinia* sporocarps. The ellipsoidal models were designed in 3D modeling software (Blender 2.67a, blender.org), and printed on a multi-jet modeler (ProJet HD 3000 3-D Modeler, 3D Systems, Inc., Rock Hill, SC USA). The dimensions of the model were geometrically similar to sporocarps, based off of SEM and dissecting microscope images. The radial appendages were metal rods and glued into eight pilot holes symmetrically printed around the equator of the body and oriented with inter-appendage angles of 0°, 90°, and 180° (Fig. 2.3G). All models contained a ninth metal rod attached opposite the angled appendages and extending to a custom-printed fitting for a force transducer. Models, appendages, and extenders were rigid under all experimental conditions.

Models were dynamically similar to a Re range of 100 to 220 based on the length scale of a sporocarp diameter (200 μm), winds from a fresh breeze (8 - 10.8 m/s) to a near gale (14 - 17 m/s), and the kinematic viscosity of air ($\nu = 1.57 \times 10^{-5}$ m^2/s). The models were printed at 135× scale of sporocarps, thus, to maintain desired Re range, velocity of flow was 20 - 35 cm/s, and the fluid used was mineral oil with a kinematic viscosity $\nu = 5.8 \times 10^{-5}$ m^2/s (dynamic viscosity $\mu = 0.049$ Pa·s measured with rheometer (Brookfield DV3T, Brookfield Engineering Laboratories, brookfield-engineering.com), and density 850 kg/m^3 measured via volume and mass). Scaling allows for the ratio of velocities and forces relative to the model to be the same as to the sporocarp (Koehl, 2003). Flow velocities were obtained by towing the model through a tank of mineral oil (Fig. 2.3F). The tank was built of clear acrylic plastic and supported by aluminum framing. The towing was achieved by a belt driven cart controlled by a stepper motor (see Munk, 2011 for specifications).

A 50cm glass plate was towed alongside models, and represented a 3.7 mm section of leaf surface. Models were positioned with a 2 mm gap between appendage tips and glass surface, so that that the fluid dynamic forces on the plate would not be recorded by the transducer. This gap did not affect the flow around the model because of tis length relative to the velocity gradient and model height. The absence of effected flow

was confirmed by comparing flow fields with and without the gap (see below for PIV technique). For each of the six tow speeds, the model was placed at one of two locations relative to the leading edge of the rigid plate. These locations were chosen to create boundary layer heights representative of those on the underside of a flittering leaf in turbulent wind. The boundary layer height was partially based on the gust time scale (see Eqn. 2.7):

$$\delta = \sqrt{\nu_{air} t_g} \tag{2.18}$$

which suggests boundary layers ∼100 μm thick for $t_g = 0.4$ ms. However, t_g is only an estimate of the time scale for one particular form of wind gust. Furthermore, aeroelastic time was estimated to be no shorter than 1ms, and, although many effects reduce the boundary layer height from that determined by viscous time (see Eqn. 2.8), a form of skimming flow (Vogel, 1996) caused by leaf pubescence is expected to increase the boundary layer thickness from the minimum set by inertia (e.g. Woolley, 1964; Meinzer and Goldstein, 1985). Boundary layers heights studied here were in the range of 160 to 260 μm. These heights were confirmed with flow field visualization taken across the glass plate, both with and without a model present. Visualization was achieved through particle image velocimetry (PIV). A horizontal sheet of green laser light (300 mW, 532 nm Wicked Lasers S3 Krypton, wickedlasers.com) illuminated silver-coated hollow glass tracer beads (Potter Industries, pottersbeads.com) seeded throughout the tank and neutrally buoyant in mineral oil. The motion of the tracer beads was filmed at 60 fps using a video camera (Fastec Hispec 1). The analysis of frames was done in PIVlab run on Matlab v7.1 (Thielcke and Stamhuis, 2014).

Models were connected via an extender and fitting to a six-axis force and moment transducer (ATI Nano17 transducer, ati-ia.com) were the signal from the transducer was acquired by PCI-6220 DAQ at 1000Hz. Only the 1.5s of forces and moments that occurred during the middle of the tow were saved, as these measurements represented the steady state flow with measured boundary layer heights. The force acting on the extender and fitting was measured, averaged, and subtracted from all force and moment results. The center of mass of a sporocarp was calculated, then scaled to that of the model, and then the distance between that calculated center of mass and the transducer was measured. The center of mass correction was

$$\tau_{\mathbf{CM}} = \tau_{\mathbf{FT}} - \mathbf{r} \times \mathbf{F} \tag{2.19}$$

where $\tau_{\mathbf{CM}}$ was the vector of torque exerted about the center of mass of the model, $\tau_{\mathbf{FT}}$ was the measured vector of torque, $\mathbf{r}$ was the vector between the transducer and center of mass of the model with length described above, and $\mathbf{F}$ were the vectors of force measured by the transducer.

Infected leaf collection and sporocarp counting

Infected leaves were collected from a heavily infected *Calycanthus* bush on the University of California, Berkeley campus near Mulford Hall (37.87285°,-122.264078°). All leaves used in wind tunnel experiments described above were also infected leaves and

collected from the same location. Before beginning a series of ascending velocity wind exposures in the wind tunnel, three sections were chosen on the bottom side of each leaf. These sections ranged in size from 16 to 96 mm^2 with one each at the base, middle and tip portion of a leaf. The chosen sections were marked on their periphery with ink so that they could be found again. Images were taken of the sections through a dissecting microscope (Wild Heerbrugg M5A) with a video camera ([need brand]). After each wind exposure leaves were carefully placed under magnification and the same leaf sections were imaged. All sets of images for all sections of all leaves were viewed using imageJ were sporocarps were identified and numbered. In this way any liberated sporocarps were recorded with information on portion of leaf where located and wind velocity prior to liberation. The number of counted sporocarps in a section varied greatly from less than ten to over two hundred.

In addition to infected leaves being used for wind tunnel experiments, they were used in paired still-air experiments. Separate infected leaves were collected on the same days as wind tunnel use, and placed in a glass tank with a cardboard drop ceiling. Three leaves could be attached to the cardboard with pushpins, and note cards were placed beneath leaves to collect any liberated sporocarps. The height of the tank was 12cm to minimize convective currents. Leaves were left pined in the still air of the tank for times ranging from 24 to 72 hours. Notecards were collected and viewed under a dissecting microscope where liberated sporocarps were counted by hand.

RESULTS

Fluttering Leaf Kinematics

To estimate the magnitude of inertial forces acting on sporocarps, quantify the potential of flutter-induced sporocarp liberation, and characterize the wind velocity profile experienced by a sporocarp on a fluttering leaf, the motion of fluttering leaves had to be recorded. For the purpose of determining if leaves fluttered more at higher wind velocities and if the tip of leaves experienced greater accelerations, the mean of max downward accelerations (see methods) was compared across portions of a leaf and across velocities (Fig. 2.4A). Mean of max accelerations were unaffected by wind velocity in the range of 4.9 to 9.4 m/s for middle and base portions of the leaf (ANOVA, Tukey, $p<0.05$). However, accelerations were significantly greater at the tip than the middle or base for wind velocities above 4.9 m/s (ANOVA, Tukey, $p<0.05$). At all four wind speeds the tips of leaves experienced greater accelerations than the middle or base (ANOVA, Tukey, $p<0.05$).

The mean of maximum accelerations also showed a dependence on leaf length for all four velocities (Fig. 2.4A, B, C, D). Most pronounced at leaf tips, the greatest accelerations occurred for leaves between 9 and 12 cm in length. This phenomenon of a particular leaf length being capable of faster velocity fluctuations than shorter or longer leaves, was independent of leaf width. Thus plotting mean of maximum accelerations against leaf aspect ratio or leaf area does not show a similar cluster of larger

values.

In addition to calculating the mean of max accelerations for individual leaves, the root-mean square of acceleration was used to estimate the aeroelastic time scale, t_a, for individual leaves (see Eqn. 2.10). The aeroelastic time and mean of max acceleration show a strong negative correlation, with Kendall's τ coefficients of -0.728, -0.747, -0.844, and -0.9167 for wind velocities 4.9, 6.7, 7.4, and 9.4 m/s respectively (Fig. 2.4F). It is noteworthy that, although some leaves had long t_a, 25% of leaf-velocity pairs had t_a equal or less than 10 ms.

To discover how the flutter-associated time scale depended on another temporal characteristic of individual leaves, t_a was plotted against the characteristic flutter frequency, ω described in Eqn. 2.15 (Fig. 2.4G). With the exception of wind speeds of 4.9 m/s, each set of leaves at a given wind speed showed a trend where some leaves at a particular ω had the longer t_a than lower or higher ω. This frequency-dependent potential to have long t_a was found near 23, 26, and 32 Hz for wind of 6.7, 7.4, and 9.4 m/s respectively. Regardless of this trend seen for the longer aeroelastic times, t_a shorter than 10 ms were found across the frequency range from 15 to 35 Hz.

Adhesive force of sporocarps to leaves

To quantify the integrally important adhesive force of sporocarps, F_{ad}, measurements and calculations were made using either Eqn. 2.16 or 2.17. Fig 2.5A shows the results of F_{ad} measurements both directionally normal and parallel to the leaf surface. Measured F_{ad} showed no significant difference between normal and parallel directions, and appears to be isotropic. Median F_{ad} shown in the figure are 37 and 45 μN for the normal and parallel directions respectively. For the purpose of establishing likelihood of liberation mechanism, both the median F_{ad} and minimum F_{ad} are referred to in subsequent sections of Results (i.e. aerodynamic resultant forces, overturning moments, initial forces, aeroelastic shedding forces). The minimum F_{ad} are 6.0 and 15 μN for the normal and parallel directions respectively, representing sporocarps with the weakest connection to host leaves.

Aerodynamic resultant forces

Although t_a was at or below 10 ms for 25% of the wind trials, the published gust time scale, t_g still largely sets the minimum time on the order of $\sim$1 ms (see Eqn. 2.7). Thus the Stokes-Reynolds number for the three modeled morphologies were 0.38, 9.3, and 17.3 for inter-appendage angles of 180°, 90° and 0° respectively (see Eqn. 2.9). This is important when considering the aerodynamic resultant forces presented in Fig. 2.6, since this dimensionless number implies that the morphology with the widest spread radial appendages should not experience the full velocity of the wind, while the other two morphologies should. The resultant forces presented here are the two-dimensional resultant forces defined as

$$F_r = \sqrt{F_d^2 + F_l^2} \tag{2.20}$$

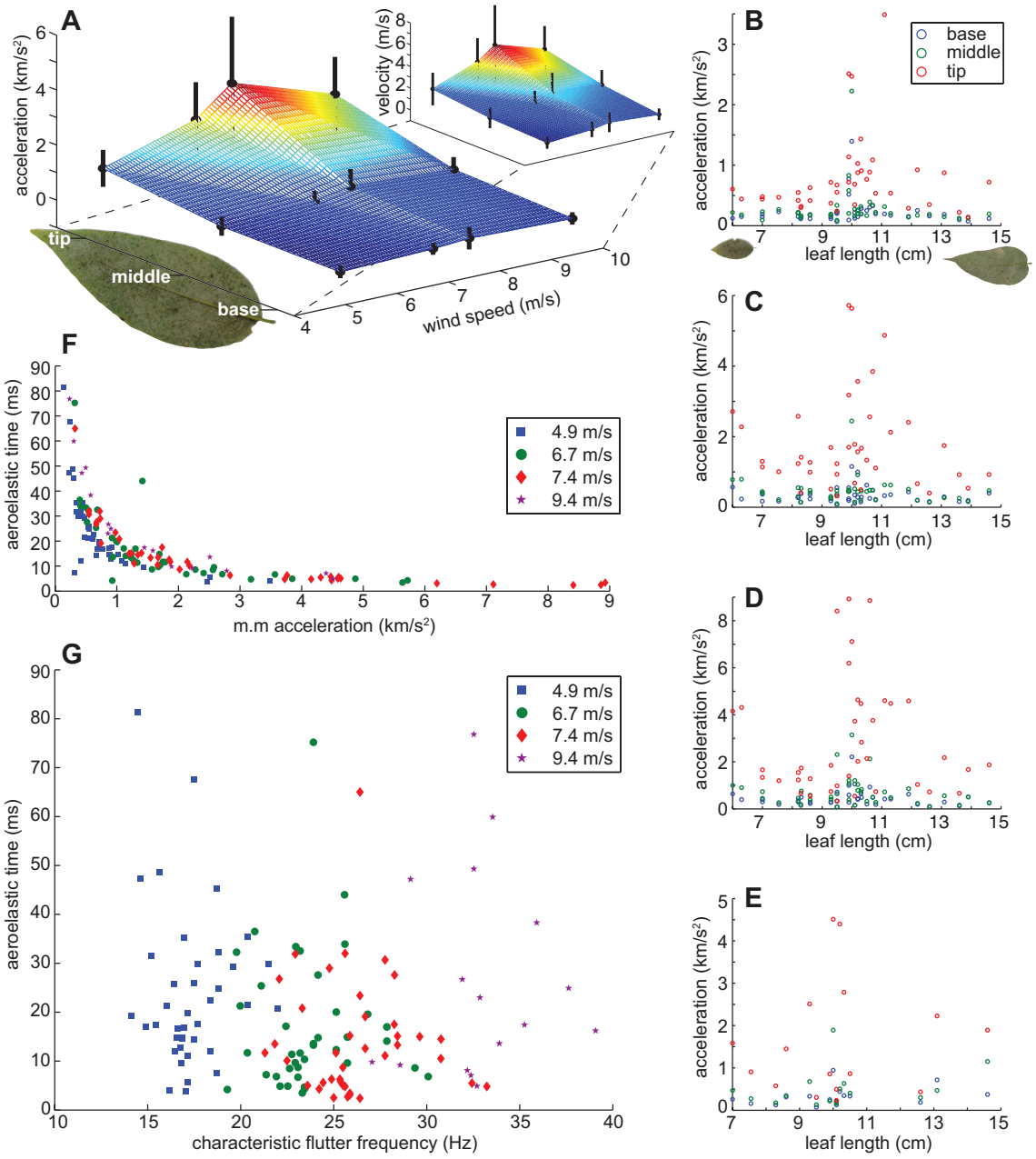

Figure 2.4: (A) Average mean of max acceleration for leaf tips, middles, and bases versus wind speed (n=39 for 4.9, 6.7 and 7.4 m/s wind; n=16 for 9.4 m/s wind), and insert showing max velocities with same horizontal axes. (B-E) Mean of max acceleration for each of three leaf locations for individual leaves versus leaf lengths, with (B) 4.9 m/s, (C) 6.7 (D) 7.4 and (E) 9.4 m/s wind. (F) Aeroelastic time, t_a, calculated for leaf tips across wind speed range versus mean of max acceleration. (G) t_a calculated at leaf tips versus characteristic flutter frequency for all four wind speeds.

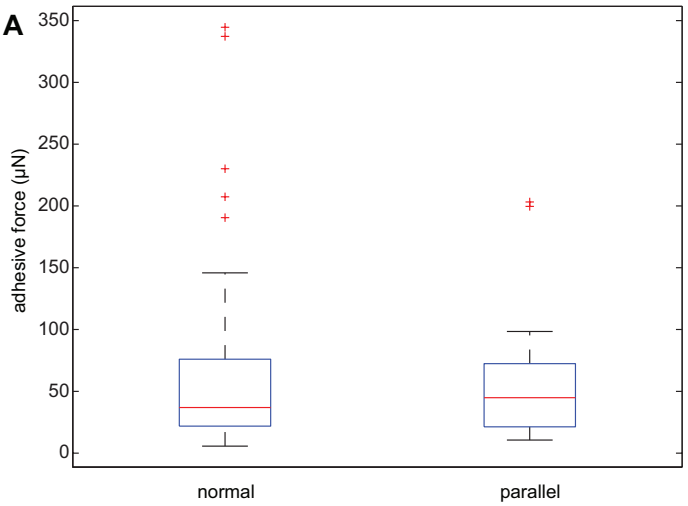

B

sporocarp	value	sample
body diamter (D_{spor})	200 ± 28 μm	n = 54
mass (m_{spor})	1.5 ± 0.40 μg	n = 84
volume (V_{spor})	≈ 2.0 x 10^{-12} m^3	calculated
appendage length (L_{spor})	315 ± 29 μm	n = 17
viscous time scale (t_v)	≈ 6.3 ms	calculated
viscous-gust time ratio (ε)	≈ 15	calculated

Figure 2.5: (A) Box plots for measured adhesive force in the normal (sample n=45) and parallel (sample n=15) directions relative to leaf surface. Blue boxes span 25^{th} to 75^{th} percentiles, red lines represent median values, black bars show minima and maxima, and red asterisks are statistical outliers. (B) Table of average parameters of mature pre-liberated sporocarps.

where F_l is the lift force:

$$F_l = 1/2 C_L \rho S_w U^2 \tag{2.21}$$

The fact that sporocarps with an inter-appendage angle of 180° (Fig. 2.6A) were subjected to significantly lower F_r than the other two morphologies is testament to the shielding effect of the boundary layer. In fact, the Kendall's τ correlation between resultant force and wind velocity was only 0.890 for the sporocarp with 180° inter-appendage angle, whereas for the sporocarps with smaller inter-appendage angles the correlation coefficient was 0.954. Interestingly, none of the morphologies showed a strong correlation between F_r and boundary layer heights, δ (τ = -0.406 for 180° and 90° morphologies, and -0.438 for 0° morphology), but it should be noted that sporocarps morphologies were either very nearly embedded in the boundary layer or protruding out of it (sporocarp profile heights: 48, 240, and 330 μm for 180°, 90°, and 0° appendages respectively).

The direction of resultant forces vectors shown in Fig. 2.6 clearly show that, although vector directions for the 180° sporocarp vary significantly, the force for the 90° and 0° sporocarps is predominantly pointing in the direction of the wind (i.e. F_r is mostly composed of F_d). The much smaller lift component of F_r points the vector slightly towards the leaf surface for the two morphologies with a narrower inter-appendage angle. It is reasonable, owing to the direction of F_{ad}, to compare modeled aerodynamic forces to parallel F_{ad}. Carrying out this comparison, it is apparent that the minimum parallel F_{ad} is not reached by aerodynamic forces, even at the highest gale force wind speeds of 18 m/s.

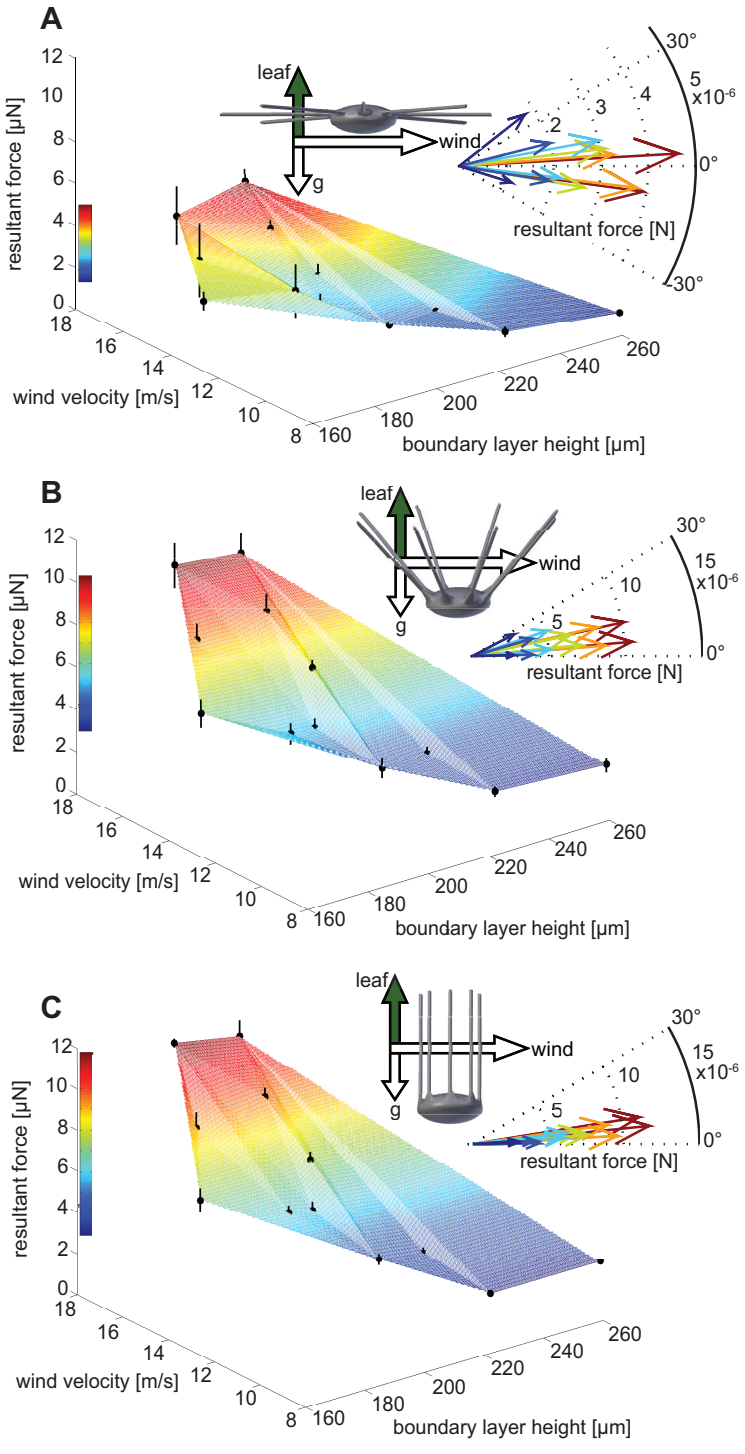

Figure 2.6: Graphs of resultant forces versus wind velocity versus laundry layer height, for (A) sporocarp with 180° radial appendages, (B) sporocarp with 90° radial appendages, and (C) sporocarp with 0° radial appendages. Errors bars represent standard deviation with n=5. Resultant force vectors are colored to matching color scale for each morphology and indicate direction of vector relative to coordinate system show beside each sporocarp icon.

Aerodynamic pitching moments

For the purpose of comparing the relative importance of the pitching moment, M_p acting on sporocarps to aerodynamic, inertial forces acting on sporocarps, moments were modeled using the same technique as aerodynamic resultant forces (see Methods). The impetus for this comparison was to quantify the effect M_p had on overturning sporocarps and potential liberation. As with modeled F_r, models upon which pitch measurements were made were delineated by inter-appendage angle (Fig. 2.7B, C, D). The sporocarp model with an inter-appendage angle of 180° experienced very small M_p as compared to the other two morphologies, and displayed a weak correlation between magnitude of M_p and boundary layer heigh, δ (Kendall's τ = -0.344). However, even the small values of M_p showed a strong correlation with wind velocity for the 180° morphology (Kendall's $\tau = 0.922$). The taller sporocarps with inter-appendage angles of 90° and 0° also displayed weak correlation between M_p and δ (τ = -0.375 and -0.438 respectively). The correlation coefficient between M_p and wind velocity was 0.954 for the 90° and 0° sporocarps.

When the magnitude of the pitch moments is compared to stability of sporocarps using Eqn. 2.13 the pitching necessary to suggest overturning is dependent on the inter-appendage angel. This implies that sporocarps with 180° appendages are less likely to be overturned for two reasons — they experience slower velocity flow so M_p is smaller, and their wider spread appendages, $b = 830\mu$m, require larger M_p to balance moments and explain liberation. Tall sporocarps with a inter-appendage angle of 0° are more likely to be overturned by the converse of the same two reasons. Considering that $b = 640\mu$m for 90° sporocarps, but only 200 μm for fully erect sporocarps, the importance of overturning is very dependent on morphology. Case in point, the minimum C_p based on minimum F_{ad} that could illicit liberation is 3.0 nNm for sporocarps with an inter-appendage of 0°, and the median C_p that implies liberation is 9.0 nNm. Thus wind speeds less than 8 m/s lead to a C_p overcoming minimum stability, and wind speeds of 14 m/s create C_p that meets median overturning stability.

Aeroelastic inertial forces and shedding

To elucidate the potential role that host-leaf aeroelasticity plays in liberating sporocarps, the kinematics of fluttering leaves were analyzed in two separate approaches. The first approach used the mean of max accelerations (see Fig. 2.4) and Newton's second law of motion to estimate directly the inertial forces, F_i exerted on sporocarps during downward acceleration of leaves (Fig. 2.2). The second approach used the root-mean square of leaf accelerations to compute within a stochastic framework the probability of spore liberation represented by a dimensionless shedding number, ψ (Eqn. 2.12).

Whereas aerodynamic resultant forces and aerodynamic pitching were measured using physical modeling, inertial forces and shedding numbers were both calculated

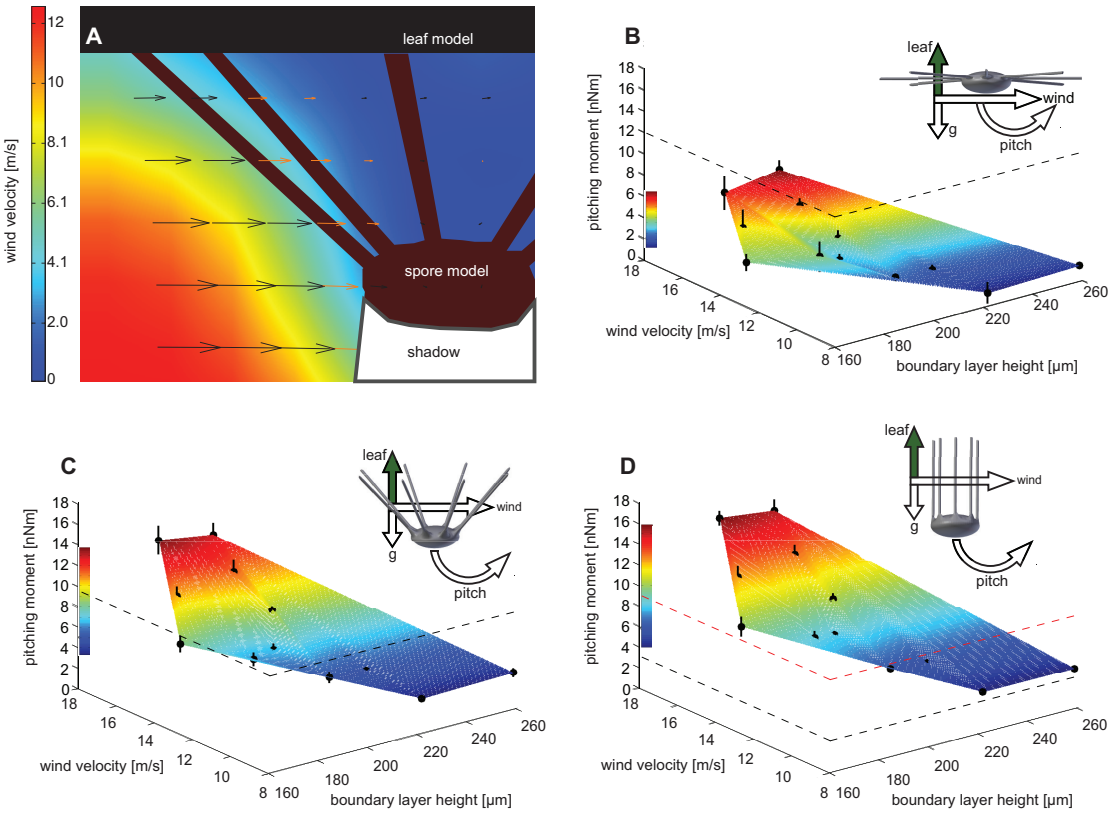

Figure 2.7: (A) PIV image of velocity gradient created by plate leaf model as it comes into contact with a sporocarp model. (B - C) Graphs of pitching moment averages (n=5) versus wind velocity versus boundary layer height with sporocarp icons showing pitch moment and coordinate system relative to the leaf, gravity and wind direction. Dotted black lines represent $C_p = F_{ad}b$ for minimum F_{ad}, and dotted red line in (D) represents $C_p = F_{ad}b$ for median F_{ad} (see Eqn. 2.13).

from collected motion capture of fluttering leaves. Unsurprisingly, the tips of leaves, as compared to the middles and bases of leaves, were calculated as exerting the greatest inertial forces on individual sporocarps (Fig 2.8A). Since inertial forces are simply the mean of max accelerations multiplied by a constant (that of the sporocarp mass, $m_s = 1.5\mu g$), all of the statistical significances stated above for average mean of maximum accelerations and shown in Fig. 2.4A hold for inertial forces compared across wind speeds and portions of a leaf (ANOVA, Tukey, $p<0.05$). Likewise, the shedding number, ψ, is proportional to t_a and when presented as dependent on characteristic flutter frequency, ω, (see Eqn. 2.15) maintains the same trends described for Fig. 2.4G. Setting ψ apart from t_a, however, is the number's inverse proportionality to wind speed. Thus, shedding numbers for higher wind-speed trials were inherently reduced relative to those of lower wind speeds. Despite this property of ψ, values for leaves exposed to 9.4 m/s were not lower than those of 7.4 m/s due to the salience of much smaller t_a

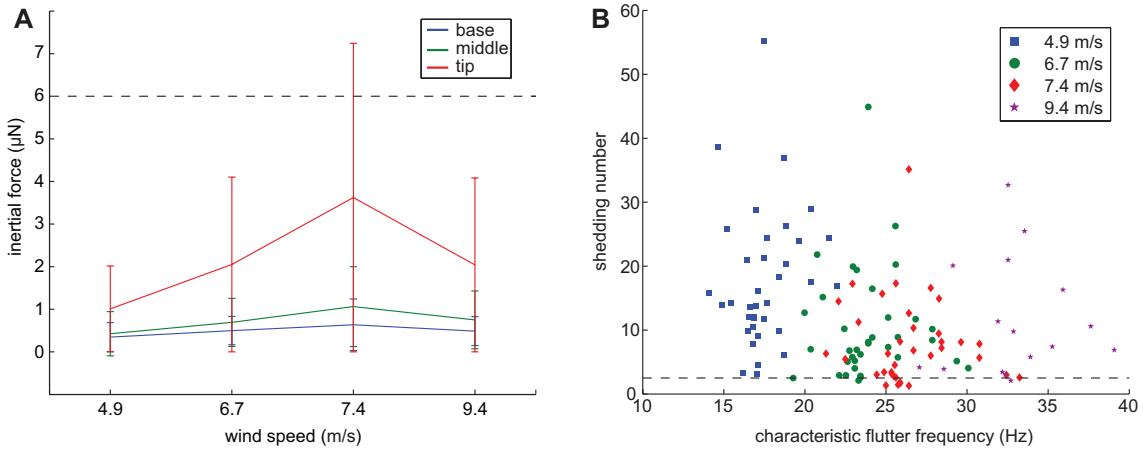

Figure 2.8: (A) Graph of average inertial force $F_i = m_s a_{leaf}$ versus wind speed for leaf locations at tip, middle, and base. Error bars are standard deviation from mean (n=39). Dotted line represents minimum F_{ad}. (B) Shedding number (Eqn. 2.12) versus characteristic flutter frequency. Dotted line represents a probability of liberation of 0.05.

for the later wind speed.

As with F_r, F_i can be directly compared to F_{ad}, but unlike F_r, F_i should be compared to F_{ad} normal to the leaf surface, since a fluttering leaf would impart kinetic energy to a sporocarp in that direction. The minimum normal F_{ad} was 6.0 μN and that value is within one standard deviation of the mean inertial force calculated for leaf tips exposed to 7.4 m/s wind, but is otherwise greater than any F_i (see Fig. 2.8A). The value of F_{ad} used in ψ was the median of 37 μN and again in the normal direction relative to the underside of the leaf. Since ψ is the variable of a narrow-band Gaussian random process (Blevins, 1990), and the probability of liberation is expressed by Eqn. 2.11, only shedding numbers below $\sim$2.5 yield an appreciably non-zero probability of sporocarp liberation. Individual leaves are indeed described by ψ below this threshold, with the majority being leaves exposed to 7.4 m/s wind and characterized by flutter frequencies just above 25 Hz (see Fig. 2.8B).

Observed sporocarp libration

Empirical liberation data supplied a ground truth within which potential liberation mechanism could be compared. The simplest manner in which to consider observed sporocarp liberation is the percent of sporocarps remaining on a given small section of leaf representing a portion of leaf after a 45 second wind exposure of a particular velocity (see Methods). Fig. 2.9A shows the average percent of spores liberated at each of twelve wind-speed leaf-portion pairs. Both wind speed and location on a leaf affect the percent of spores liberated, and evidence of an interaction effect between wind speed and leaf location exists (Two-way ANOVA, $p<0.05$).

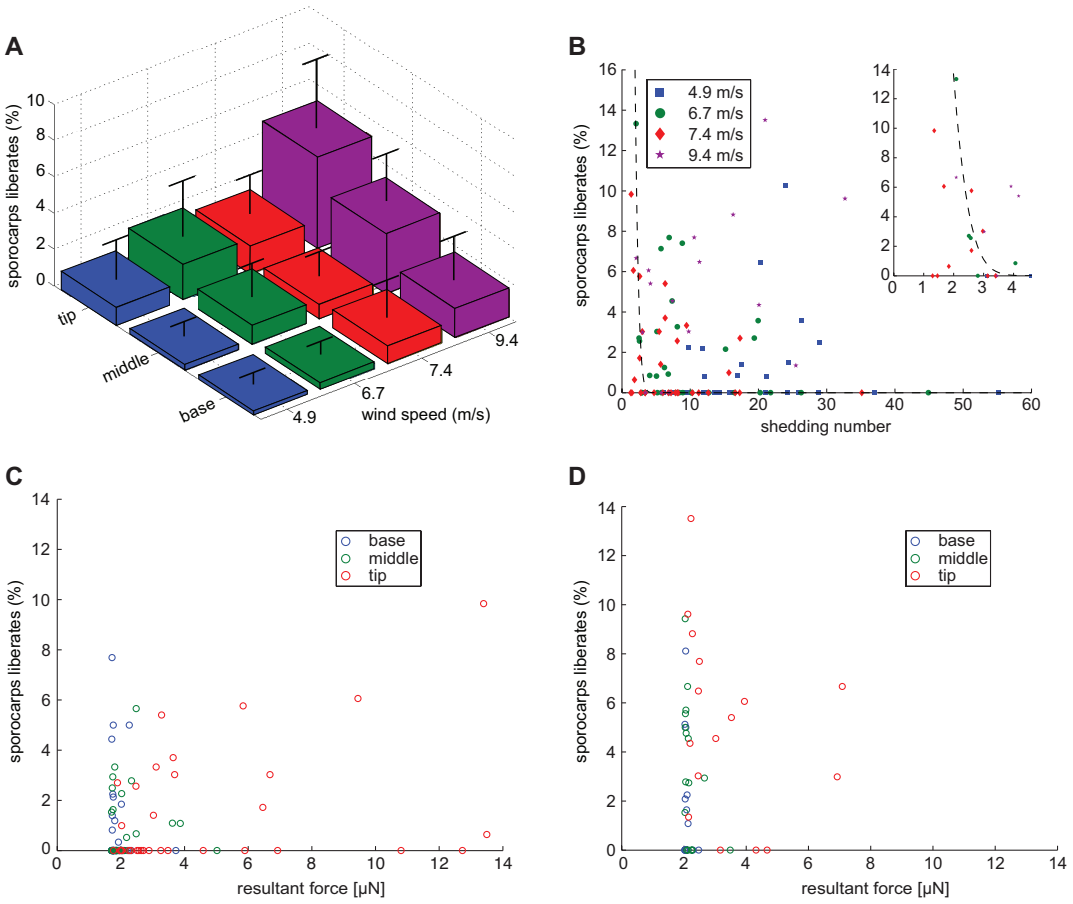

Figure 2.9: (A) Percent of sporocarps liberated versus leaf portion versus wind speed. Error bars are standard deviation from the mean (n=39). (B) Percent of sporocarps liberated versus shedding number, ψ for leaf tips across wind speeds. Insert shows in more detail the curve of the probability function predicting sporocarp liberation as represented by the dotted line (Eqn. 2.11). (C-D) Percent of sporocarps liberated versus modified resultant force, $F_{r'}$, (Eqn. 2.22) for wind speeds 7.4 m/s (C) and 9.4 m/s (D).

To compare the probability of sporocarp liberation (Eqn. 2.11) based on the shedding number, ψ to observed liberation, ψ was plotted against liberation percents (Fig. 2.9B). The correlation coefficients for these parameters were very weak with the highest being -0.216 for 7.4 m/s wind, with coefficient of -0.185 for 6.7 m/s wind (Kendall's τ). Furthermore, wind velocities of 4.9 and 9.4 m/s showed correlation in the opposite direction of what the probability distribution would suggest, with correlation coefficients of 0.202 and 0.279 respectively (Kendall's τ). These correlations are made weaker by the large number of leaves for which no sporocarps were liberated.

A modified resultant force, $F_{r'}$ was calculated for the purpose of comparison to the

percent of liberated spores. This force combined F_r and F_i by justifiably assuming the two force vector act orthogonal to one another:

$$F_{r'} = \sqrt{F_r^2 + F_i^2} \tag{2.22}$$

Again the correlation between the force based on proposed liberation mechanisms and the actual liberation of sporocarps is quite weak. In fact, for 7.4 m/s wind (Fig 2.9C) only the tip of leaves showed a correlation coefficient above 0.1, at a value of $\tau = 0.257$. In 9.4 m/s wind (Fig. 2.9D) the correlations show even less support for the idea that calculated and modeled resultant forces could be used as a predictor of actual sporocarp liberation. The correlation coefficients in 9.4 m/s wind were -0.139, -0.400, -0.262 for base, middle and tip leaf portions respectively (Kendall's τ), therefore all showing a weak trend in the opposite direction that may be expected. These weak and contradictory correlations are, as with ψ covered above, weakened by leaves that lost no sporocarps, but also imply that many sporocarps only require a force of $\sim 2\mu$N to overcome F_{ad}.

Observed sporocarp liberation was also considered as a rate for the purpose of com-

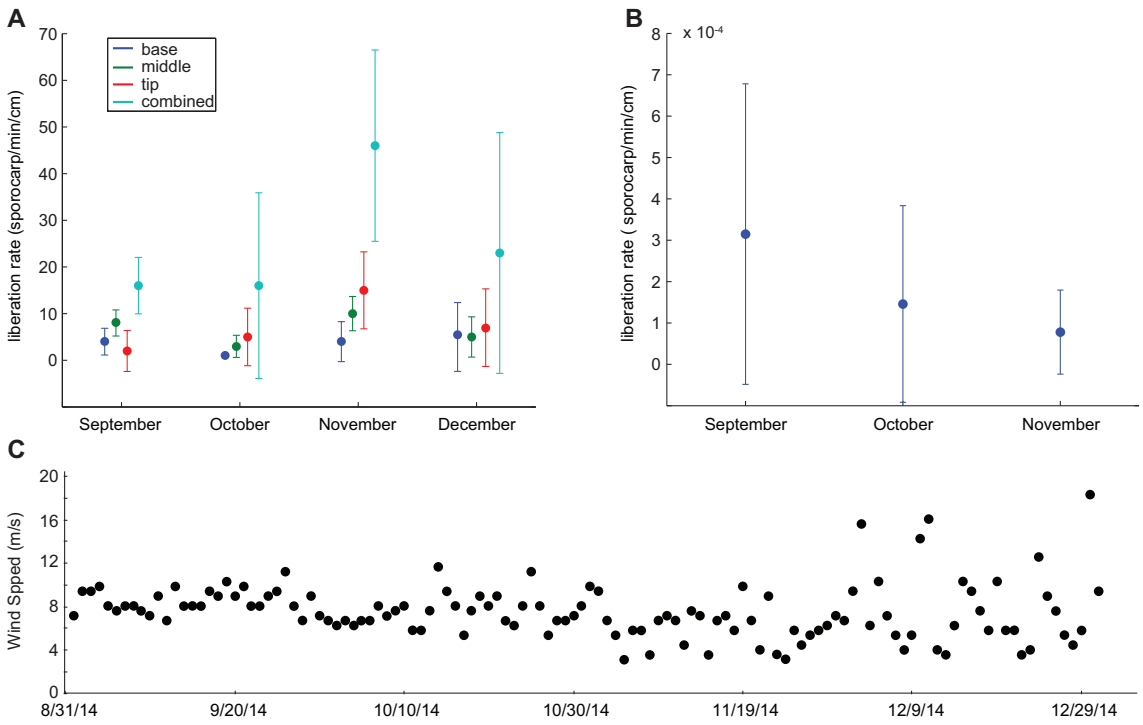

Figure 2.10: (A) Graph of average sporocarp liberation rate in wind versus month showing rates for each of three portions of leaves and rate combing all three portions. (B) Graph of average sporocarp liberation rate in still air versus month. (C) Nearby wind data for Oakland, CA (source: Oakland International Airport).

paring across the months of the sporulation season, and particularly for the purpose

of comparing wind liberation to liberation in still air (see Methods). The liberation rate in wind was statistically higher in November than in September (Fig. 2.10A), but otherwise did not depend on the month of the year (ANOVA, Tukey, $p<0.05$). Liberation rates in still air (Fig. 2.10B) showed no dependence on month of the year (ANOVA, Tukey, $p<0.05$). The liberation rate in wind was approximately six orders of magnitude greater than liberation in the absence of wind. The nearby wind record (Fig. 2.10C) suggests that for 2014 large wind events began in late November. The velocities shown are representative of a more exposed location than where leaves were collected. The field gust of $\sim$7 m/s shown in Fig. 2.3A was recorded on December 30^{th}, 2014, and corresponds to a gust velocity of 19 m/s shown in Fig 2.10C.

DISCUSSION

Comparisons of potential liberation mechanisms

The four potential wind-induced liberation mechanisms presented in this study are bookended by the measured adhesive force with which sporocarps are connected to leaves, and the counted number of sporocarps liberated as a function of location on a leaf, wind velocity, and leaf accelerations. This approach of modeling supported by empirical data supplies a quite useful perspective to answer the question if sporocarps of *Phyllactinia* are sheared, rolled, flung, or shaken off by ambient wind.

It is evident that the median F_{ad} (37 μN in the normal direction and 45 μN in the parallel direction, see Fig. 2.5A) was very rarely reached by modeled and estimated forces and moments. In fact, only overturning induced by the pitching moment, and only for wind speeds above 13 m/s exceed the liberation threshold set by the median F_{ad}, and only for a sporocarp morphology with a 0° inter-appendage angle (Fig. 2.7D). It should be noted, however, that percents of observed liberated sporocarps are quite low (all with averages below 6%, see Fig. 2.9A), so a liberation mechanism meeting the force or moment requirements of median adhesive force is actually unnecessary for the purpose of speculative liberation mechanisms. Since the highest wind speed attainable in the wind tunnel was 9.4 m/s, the high wind speeds required to meet thresholds set by median F_{ad} (Fig. 2.5A), and the low percents of sporocarps liberated are in good agreement (compare Figs 2.6, 2.7, and 2.8 with 2.9).

Indeed, the most significant finding of this research is two-part, that overturning is the most supported and consequently likely liberation mechanism in wind, and that flutter effects are unsupported as a liberation mechanism. The importance of pitching over for sporocarps is congruent with the idea put forth in Alexopoulos et al. (1996) that bending radial appendages expose the sporocarp to greater wind speeds, but here it is not the drag or resulting shear that is having a large effect, but rather the unstableness inherent in a fully erect sporocarp. Inertial liberation and aeroelastic shedding seemed probable candidates for liberation, both because of recent findings in the pollen-shedding literature (Urzay et al., 2009; Timerman et al., 2014), and because the accelerations created by fluttering *Calycanthus* leaves at a biologically-relevant wind

speed are quite dramatic ($\sim$4 km/s^2 in a 7.4 m/s moderate breeze, see Fig. 2.4). However, neither the inertial forces arrived at through an average sporocarp mass, m_s, nor the shedding number, ψ, reconcile liberation thresholds in the same way achieved by pitching over for fully erect sporocarps. Furthermore, the strong disagreement between shedding number and liberation percents, and the nearly complete deviation from the shedding probability curve (Fig. 2.9B) point towards fluttering as having no bearing on liberation.

The lack of experimental support for flutter and vibration-induced liberation is somewhat confounded by the statistically significant higher percentage of sporocarps liberated at leaf tips (Fig. 2.9A), but this may be explained by considering the governing time scales, t_g and t_a (Eqns. 2.7 & 2.10). Perhaps sustained wind such as that in the wind tunnel (45 seconds at a given velocity), creates a fluid flow situation in which gust time, t_g, is no longer the shortest time scale, since it is predicated on intermittent gusts. Accordingly, t_a would set the boundary layer height. Sporocarps at the tips of leaves may be exposed to thinner velocity gradients, higher wind speeds, and consequently roll off independent of inertial and aeroelastic effects.

The modified resultant force, $F_{r'}$ (Eqn. 2.22), and plotted in Fig. 2.9C, D, seems to imply that many sporocarps are liberated with a force of 2 μN. This seems to be in contradiction with the minimum measured F_{ad} of 6.0 μN. Although the modified resultant force is appropriately plotted versus percent liberation for the purpose of seeing if certain velocities and leaf portions show greater correlation with liberation, it is not necessarily representative of the full forces and moments applied to a sporocarp — particularly not moments. The most accurate way to consider the modified resultant force is that it acts in conjunction with pitching moments. It is the sum of forces and moments that liberate a sporocarp, with pitching seemingly playing the dominant role. In point of fact, at the same two wind speeds shown in Fig. 2.9C, D sporocarps with a 0° inter-appendage angle would be acted upon by moments of $\sim$4 and $\sim$6 nNm, well above the minimum threshold for liberation.

The empirical results of sporocarp liberation show a great deal of variation, e.g. in some instances sporocarps liberated immediately at the lowest wind speeds, and in other instances not a single liberated sporocarp was recorded for a leaf (implied by the large error bars present in Fig. 2.9A). This is indicative of each liberated sporocarp, and each F_{ad} measurement made on a sporocarp, representing a window-in-time into the gradual and coordinated degradation of the physical connection between sporocarp appendage tip cells and neighboring mycelium cells, which is a well documented and important phenomenon throughout the life cycles of plants (reviewed in Roberts et al., 2002). This degradation may be due to the upregulation of certain genes during abscission or it may be the result of a purely mechanical process brought about by dehiscence and resulting hygroscopic movement, but regardless the connection between sporocarp and leaf is not severed by wind alone.

Nor does it seem likely that the abscission and gravity are solely responsible for liberation in still air. The gravitational force acting on a sporocarp is only $\sim$15 nN based on the measured average m_s in this study, and thus the physical interface between

sporocarp and leaf would have to be weakened beyond what seems possible. Furthermore, measured F_{ad} never approached such a small value of force. It is more probably that viscoelastic energy stored in the appendages is released as a catapulting force as hypothesized by Cullum and Webster (1977), and similar to the jumping of *Equisetum* spores (Marmottant et al., 2013). What is clear, however, is that in combination with passive liberation in wind, *Phyllactinia* liberates sporocarps actively in still air (as evidenced by Fig. 2.10B). When presented with the drastically different rate of spore liberation in still air versus in strong wind, it may help to consider that based on those rates it takes ∼100 days, (the entire sporulation season) for a comparable number of spores to be liberated in still air as are liberated in one minute of strong wind.

Implications and future directions

One may ask why are sporocarps not liberated more easily? The evidence in this study is that sporocarps are liberated actively at a steady, but very slow rate (especially in relation to their fecundity), but why is that rate not faster, and why do values of F_{ad} not point to liberation in light or gentle breezes? It is, of course, possible that sporocarps cannot liberate more easily, that development from the mycelium does not allow it even if there exists a selective advantage for low-force liberation. Another possibility is that a selective advantage exists for high-force liberation. This is an attractive notion, because it would support liberation coinciding with high wind events, while still allowing for slow but consistent liberation. As Gaines and Denny (1993) call attention to, ecological dynamics may depend as much on environmental extremes as average conditions. Active liberation with its rate of $\sim 3 \times 10^{-4}$ sporocarps/min/cm might serve the purpose of reinfection of the host, while passive liberation in high wind with its rate of ∼30 sporocarps/min/cm may function as an effective means of dispersal.

The quantification of liberation in wind presented in this study in terms of F_{ad} and wind speed thresholds adds to the emerging incorporation of liberation mechanisms into the research on propagule dispersal. Johansson et al. (2014) states that transport is comparatively well studied, but that liberation, especially in the presence of turbulent wind, is a largely missing component of our knowledge of dispersal. The need for understanding liberation thresholds and mechanisms has received a good deal of recent attention in the modeling of dispersal (e.g. Schippers and Jongejans, 2005; Kuparinen, 2006). Furthermore, the size and Re range covered in this study may apply well to the similar biological systems of large pollen grains, rust teliospores, and downy mildew sporangia.

To further reveal the importance of pitching over in sporocarp liberation a key parameter of passively liberated sporocarps could be measured — the inter-appendage angle. This could be accomplished by either collecting liberated sporocarps downstream, precisely filming sporocarps as they are liberated, or simply taking microscope section images as done here, but with transverse lighting so sporocarp shadow lengths could be used as proxy for sporocarp height. Using one or more of these techniques, inter-appendage angles of liberated sporocarps could be correlated with liberation, and

the liberation mechanism of pitching could be tested empirically.

Furthermore the importance of the pitching moments and subsequent overturning and liberation of mature sporocarps was based on a balancing of moments, but the argument could be made for the occurrence of fracture at the tips of the radial appendages. This approach was not taken in this study for discussing the physical importance of overturning, because, although the radial appendages were observed to tapper at the tips, the tip radius connected to the mycelium was not consistently measured, and the maximum strength of the material composing the appendages is unknown. However, if a mechanical connection is assumed the most likely source of adhesion then relevant work can be done in the future to approach appendage-tip fracture as in Wainwright et al., (1976):

$$r_{min} = \left(\frac{4F_d h}{\pi \sigma} \right)^{1/3} \tag{2.23}$$

where h is the profile height of the sporocarp, σ is the maximum strength of the radial appendages, and r_{min} is the minimum appendage-tip radius that could withstand a drag force of magnitude F_d before fracturing.

This set of experiments has shown that while vibration may be important for some pollen grains, the same is not trie of the larger sporocarps of *Phyllactinia* on fluttering leaves. The evidence supporting the importance of the pitching moments in liberation should be considered in the context of aerodynamic and hydrodynamic moments in general. The biological importance of rolling, twisting and pitching is largely overlooked, but with techniques such as physical modeling it can be explored to the great benefit of biomechanical understanding, and the importance of shape. The fact that sporocarps are not protected in the boundary layer, but that real world conditions like fluttering and turbulence insure that they are exposed to high speed air flow is an example of an important physical phenomenon that explains how flow interacts with organisms in a way steady-state approximations would overlook.

ACKNOWLEDGEMENTS

This research was supported by a National Science Foundation IGERT Traineeship (to T. Dolinajec), IGERT Grant #DGE-0903711 (to R. Full, M. Koehl, R. Dudley, and R. Fearing), and by NSF Grant #IOS-1147215 (to M. Koehl). For technical assistance, I thank Hao Pham, Brooke Maushund, Karen Burtt, Gian Ha, Nancy Wang, Michael Manguinao, Eric Shade, Bethany Zhang, Roman Ramos, and Katelyn Greene, students participating in the Undergraduate Research Apprenticeship Program at the University of California, Berkeley.

3

Aerodynamic stability and terminal velocity of sporocarps: microscopic shuttlecocks

KEYWORDS

abiotic dispersal, phytopathogens, *Phyllactinia*, aerial righting, PIV, chasmothecia, irregular shape

HIGHLIGHTS

- Terminal velocity is correlated with morphological features of sporocarps, including the length and spread of radial appendages
- Stokes law accurately models terminal velocity of sporocarps operating at Re 1.0 to 3.3, but only when the aerodynamic diameter accounts for airflow between widely spread radial appendages
- Angular velocities and angular accelerations of rotating sporocarps decrease as the angle of attack of sporocarps approaches zero
- Sporocarps display a stable fixed point at zero angle of attack
- Sporocarps that rotate the fastest also fall the fastest, and sporocarps that rotate the slowest also fall the slowest

INTRODUCTION

Dispersal is an important component of the life histories of many types of organisms across the kingdoms of life. Dispersal serves a number of important functions, including spread within a habitat, extension of geographic range, and enhancement of genetic diversity of a species (Ingold 1965). Motile organisms are capable of active dispersal, but non-motile organisms, such as plants and Ascomycota fungi, produce propagules that are dispersed passively, either by being carried on or in other organisms, or by being transported by ambient wind or water flow (reviewed in Howe and Smallwood, 1982). Passive dispersal of propagules involves three steps: liberation, transport, and deposition. The focus of this study is the transport stage of dispersal of passive propagules carried by the wind.

Wind dispersal

Terminal velocity

The longer a passive propagule remains airborne, the greater the distance the wind can carry it before it lands, therefore features that reduce the terminal velocity of a falling propagule can increase its dispersal distance. (e.g. Nathan, 2011). The terminal velocities of a variety of wind-dispersed propagules have been measured. Spherical spores of *Lycoperdon giganteum*, (diameter $\sim$4 μm) are reported to settle in air at a range of terminal velocities: 0.44 to 0.68 mm/s (Gregory and Hendon, 1976). Spores of slime molds in the class Myxomycetes (diameters of 5.6 to 12.7 μm) have V_t ranging from 0.53 to 3.85 mm/s (Tesmer and Schnittler, 2007). Urediniospores of the fungus *Uromyces phaseoli*, pollen grains of the ragweed *Ambrosia elatior*, and spores of *Lycopodium*, with average diameters of 21.0, 21.5, and 32.8 μm respectively, have mean terminal velocities of 0.86, 1.05, and 1.94 cm/s respectively; with a normalized terminal velocity for clusters of spores fit by the exponential regression $V_{tN} = 0.98N^{0.53}$ (Ferrandino and Aylor, 1984). However, a more recent study measures V_t of *Lycopodium* at 4.2 cm/s (Loubet et al., 2007). Jackson and Lyford (1999) review the measured terminal velocities of pollen grains from 42 genera of plants and report terminal velocities from $\sim$2 to $\sim$14 cm/s. Dust-like seeds of *Brassavola nodosa* have mean dimensions of $640 \times 56\mu$m and a mean terminal velocity, V_t, of 15.7 cm/s (Murren and Ellison, 1998). Small seeds of the family Asteraceae, measuring 1 - 5 mm in length, fall at Re 160 - 900, and at terminal velocities ranging from 0.28 to 1.4 m/s, with morphology demonstrating a pronounced effect on V_t (Andersen, 1993). In addition to the pattern that as propagule size increases from microns to millimeter, so too reported V_t increases from mm/s to cm/s, there is a implicit, and occasionally explicit, trend in the literature cited above that propagule shape affects terminal velocity.

The terminal veloicty (V_t) of a body falling through air is given by

$$F_d = mg \tag{3.1}$$

where m is the mass of the propagule, g is the acceleration due to gravity, and F_d is drag, the aerodynamic force resisting the motion of the body through air. Drag is higher if the velocity of a body through a fluid is greater, but the quantitative relationship between drag and velocity depends on the relative importance of inertial forces and viscous forces in resisting the motion of the body. Reynolds number (Re), which represents the ratio of inertial forces to viscous forces, is given by

$$Re = UL/\nu \tag{3.2}$$

where U is the velocity of the fluid relative to the propagule, L is a characteristic linear dimension of the organism (radius in this study), and ν is the kinematic viscosity of air (1.57×10^{-5} m^2/s for air at 20° in this study). Many of the smallest propagules are on the order of 1 - 10 μm, and can be thought of as bioaerosols with terminal velocities not large enough to suggest significant settling. Many fungal propagules occupy this size range, and fall at Re < 1, where drag is given by the Stokes equation:

$$V_t = \frac{\rho_s d_a^2 g}{18\eta} \tag{3.3}$$

where ρ_s is the density of the propagule, d_a is the aerodynamic diameter (Hinds, 1999), g is the acceleration of gravity, and η is the dynamic viscosity of air (1.85×10^{-5} Pa·s). This derivation ignores buoyancy since the density of air is only 1.18 kg/m^3, and thus ~ 3 order of magnitude less than the density of most propagules. Gregory (1961) observed that Stokes' law provides a good approximation of spores and pollen grains ranging from 4 to 100 μm in diameter falling through still air. In contrast, for propagules operating at Re > 1 various versions of a quadratic equation have been used to describe the drag, such as:

$$V_t = \sqrt{\frac{2mg}{\rho S_p C_d}} \tag{3.4}$$

where m is the mass of the propagule, ρ is the density of air, S_p is the projected area of the propagule, and C_d is the drag coefficient of the propagule. This formulation largely assumes that C_d is not a function of Re and consequently independent on V_t (Vogel, 1996), but direct measurement of C_d can extend the use of quadratic drag to lower Re. In fact, detailed curve fitting of C_d for irregularly shaped particles at intermediate Re has mitigated the need for experimental measurement of C_d (reviewed in Loth, 2008). When propagules with d ≈ 200 μm fall at Re ~ 1, it is not yet clear whether Stokes drag or quadratic drag is a better approximation of the fluid dynamic force on the body.

Wind dispersed propagules operate at a range of Re. For example, fungal spores, many of which are $< 10\mu$m, fall at Re $\leq 4\times10^{-4}$ (e.g. Gregory and Hendon, 1976). Passively transported pollen grains of anemophilous gymnosperms operate at Re 4×10^{-2} to 3×10^{-1} (reviewed in Jackson and Lyford, 1999). Wind-dispersed plant seeds vary in size from tiny free-falling orchid seeds with a Re of $\sim$6 (Murren and Ellison, 1998), to autorotating single-winged samaras with a Re of about 2000 (Norberg 1973). Arthropods that are passively dispersed such as ballooning spiders operate at higher Re of approximately 2×10^3 to 3×10^4 owing to the long lengths of silk (Suter, 1991). While Stokes' equation can be used for the tiniest spores and pollen, and a quadratic drag equation for spiders and large seeds, small plant seeds and fungal sporocarps operate at Re $\sim$ 1 where the dependence of drag on velocity is not clear.

Whether or not propagule shape affects drag depends on Re. Propagule shape does not affect the aerodynamic performance of dispersal for the smallest fungal spores such as individual ascospores measuring $\sim$1 μm in diameter, and in fact such spores have drag minimizing shapes that suggest optimization during forcible liberation (Roper et al., 2008). Pollen grains are mostly spherical with little evidence of specialized morphologies for dispersal (Niklas, 1985), with the notable exception of saccate pollen that contain air-filled bladders that have been shown to increase drag, and which are described by Re $\sim 10^{-2}$ at terminal velocity (Schwendemann et al., 2007). This research on saccate pollen suggests that a decrease in density rather than the shape of the pollen grain affects aerodynamics. At larger size scales; falling ants (Yanoviak et al., 2010), aerodynamically stable samaras (Salcedo et al., 2013), and gliding frogs (McCay, 2001) all demonstrate the importance of shape with regards to dispersal. However, the effects of shape at Re $\sim$ 1 are not well understood.

Wind-dispersed propagules of plants and fungi are transported across a wide range of spatial scales, from 10^-2 to 10^2 m affecting spread within a habitat, and 10^1 to 10^4 m affecting colonization of new sites (Levin, 1992). Studies of dispersal of fungal pathogens of plants have used two different types of equations to calculate the spatial distribution of spores landing around an infected plant. Both types of distributions relate the spore concentration, C, to horizontal distance, x, with the first assuming $C \propto e^{Ax}$, and the second assuming $C \propto x^{-B}$, where A and B are constants that determine the rate of decrease in spore concentration with distance (McCartney et al., 2006). Furthermore, the Cauchy distribution, a model using the second type of distribution, has proven important in the study of spore dispersal gradients (Zhou and Kot, 2013). The fitting of constants A and B used in distribution models is done through mechanistic modeling that considers the trajectories of individual propagules(e.g. Bullock and Clarke, 2000), and require careful attention at Re $\sim$ 1 for the reasons stated above.

Mechanistic models of dispersal have undergone many iterations in the literature (Nathan, 2011), with the most rudimentary ballistic model yielding

$$D = \frac{h_z \bar{u}}{V_t} \tag{3.5}$$

where h_z is the release height, $\bar{u}$ is the mean horizontal windspeed, and V_t is the terminal velocity of the propagule. Refinements on the basic ballistic trajectory include refinements to $\bar{u}$, which include logarithmic profiles typical of flow over short canopies or crops (e.g. Sharpe and Fields, 1982; Nathan et al., 2001), and exponential profiles including an attenuation coefficient typical of flow through dense canopies (e.g. Cionco, 1965; reviewed in Finnigan, 2000). One property these models have in common is an inverse proportionality between dispersal distance D and terminal velocity, V_t, or perhaps more accurately the difference $(V_t - W)$, where W is the vertical wind speed (Nathan et al., 2001).

Aerodynamic stability

In addition to terminal velocity, aerodynamic stability and aerial righting are important aspects of performance for wind-dispersed propagules that must land right-side-up to successfully colonize a new surface (Webster, 1979). Aerodynamic stability and righting performance have been studied for a variety of animals of different sizes parachuting or gliding through the air. Animals can assume an aerodynamically-stable posture as they fall, or can actively move their limbs to exert restoring moments. Among macroscopic animals aerial righting and gliding are potential evolutionary precursors to winged or flapping flight (Dudley and Yanoviak, 2011; Jusufi et al., 2011), with a strong selective pressure likely leading to the evolution of directed aerial descent (Yanoviak et al., 2011). Rotational maneuvers are affected by the mass-moment of inertia of the animal, and active changes in the instantaneous moment of inertia can reorient an animal that is falling upside-down without pushing off a surface, without changes to angular momentum, and without significant aerodynamic drag moments (Jusufi et al., 2010; Jusufi et al., 2011, Libby et al., 2012).

If the moment of inertia of an organism is not mutable during aerial descent than another explanation for the generation of rotational moments must be found. In fact, the allometry of maneuverability suggests that even for organisms capable of changing their instantaneous moment of inertia (e.g. through muscle movement) there exists a size limit below which rigidity and a static moment of inertia may effectively lead to rotational accelerations and aerial-righting (Dudley, 2002; Ribak and Swallow, 2007). For insects of length 20 mm or less, aerial righting has been observed with the limbs held stiff (larval stick insects in Jusufi et al., 2011; wingless pea aphids in Ribak et al., 2013). This strongly implies that small insects are not using inertial air-righting moments to reorient. The two part scaling argument is that force and moment coefficients increase steeply with size and Re, and aerodynamic moments causing rotation scale with length to the power three, while the mass-moment of inertia scales with the length to the power of five. Thus aerial righting below Re$\sim$20 is dominated by aerodynamic moments. In this size and terminal velocity regime the moment of inertia of an organism only serves the purpose of slowing rotation, rather than initiating it.

A relevant implication of aerodynamic aerial-righting to the present study is that

organisms and propagules need not be capable of movement mid-air to achieve reorientation. Considering the scaling arguments mentioned above and Newton's second law for rotational motion:

$$M = I\dot{\omega} \tag{3.6}$$

where M is the aerodynamic moment, I is the moment of inertia, and $\dot{\omega}$ is angular acceleration. It is apparent that the ratio of M/I may create large values of α with only the requirement of very small values of M in magnitude. The counterpoint to this is that the minuscule moment of inertia that allows for large angular accelerations may also make airborne propagules with characteristic $L \leq 1$ mm inherently unstable. Aerodynamic stability without muscles has been studied in some depth with regard to single-winged seeds (e.g. Norberg 1973; Salcedo et al., 2013), but such seeds are much too larger for the aforementioned allometric considerations to apply. To the best of the author's knowledge there is no research on the mechanism that may create aerodynamic stability in dust-like seeds, or other propagules in the size range of 100 μm to 1 mm. Aerodynamic stability for these propagules operating at Re ~ 1 may not be combined with autorotation or the generation of lift as with maple seeds and tuliptree seeds (Horn et al., 2001), but instead orient the propagule at a high-drag angle with respect to airflow. Passive aerodynamic stability for propagules falling at near-unity Re may also serve a similar purpose as stability in falling aphids, i.e. allowing for a desirable orientation upon landing.

Phyllactinia — model system for short and long range airborne and microscale aerodynamic stability

Sporocarps of the mildew *Phyllactinia* were used to study the effects of body shape on the terminal velocity and aerial righting performance of wind-dispersed propagules at Re ~ 1.

In the context of phytopathogens, extension of range equates to locating new hosts, and maintenance of a current range entails reinfection of a host. For obligate parasites such as powdery mildews, reinfection of a plant host can only occur after surviving a period of time such as the winter in which plant tissue is not available for infection — a process known as perennation (reviewed in Glawe, 2008), that must be followed by short distance transport onto fresh plant tissue. The fungal mildew *Phyllactinia* is an example of an obligate parasite, and the resting spore packet adapted to perennation is known as a cleistothecium (Cullum and Webster, 1977) or chasmothecium (Glawe, 2008), but hereafter referred to as a sporocarp for wider comprehension. The sporocarp of *Phyllactinia* has an ellipsoidal body approximately 200 μm in diameter (Fig. 3.1), and contained within that body are tubes know as asci that contain sexual ascospores (Alexopoulos et al., 1996). It is common in the order Erysiphales (powdery mildews) for perennating spores to also be a component of the sexual life cycle of the organism, but *Phyllactinia* is unusual in that reinfection via sporocarps involves an aerial transport phase (Cook et al., 2006).

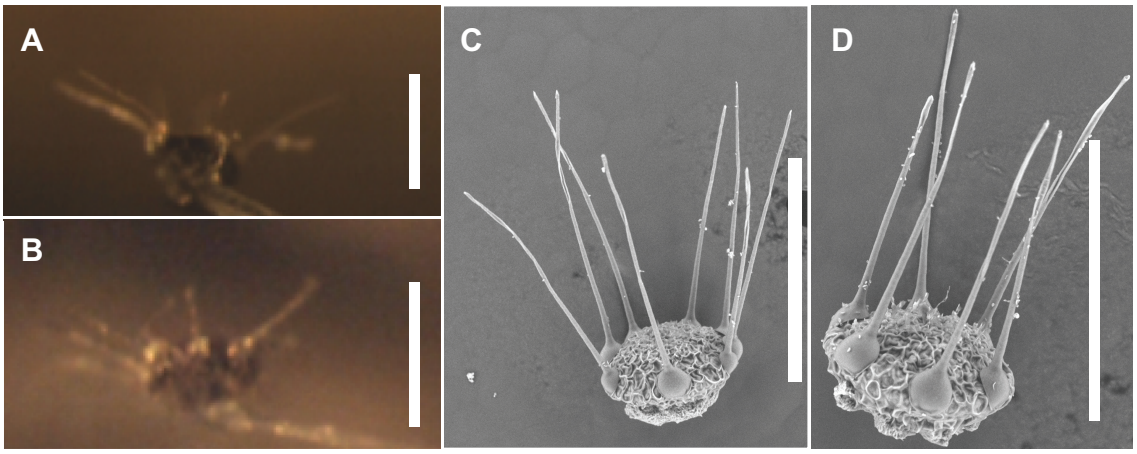

Figure 3.1: A-B) Light microscope images of sporocarps with widely spread radial appendages. (C) Scanning electron microscopy (SEM) images of sporocarps with appendages bent upward. All scale bars are 250 μm.

It is hypothesized that the shape of *Phyllactinia* sporocarps affects aerodynamic performance, in that rigid radial appendages function as the skirt of a shuttlecock and lead to aerial righting (Webster, 1979). There exists a strong selection pressure for successful aerial righting since sporocarps must land with their radial appendages facing up to stay attached following deposition (Itoi et al., 1962), and to be in the correct orientation for forcible release of ascospores following perennation (Cullum and Webster, 1977; Alexopoulos et al., 1996). The lance-like radial appendages are known to bend during maturation while still attached to the host-plant leaf (e.g. Kumar and Gupta, 2004), and consequently airborne sporocarps have a wide range of appendage spread (see Fig. 3.1A, B, C, D for examples). Based on a sphere of equal diameter to a *Phyllactinia* sporocarp and density of 1000 kg/m^3 the terminal velocity is $\sim$70 cm/s, and the Re is $\sim$9 (Dennis, 1976). However, the appendages speculated to cause aerial righting may also increase drag and decrease terminal velocity and Re in a similar way to high Re shuttlecocks (Verma et al., 2013).

Objectives

The objective of the this study was to investigate the consequences of shape to the aerodynamic performance of wind-dispersed propagules at Re of order 1. Sporocarps of *Phyllactinia* were used to address two specific hypotheses:

1) Shape affects terminal velocity.

2) Shape affects aerial righting.

METHODS

This study contained two parts, high-speed videography of free-falling sporocarps, and dynamically scaled physical modeling of sporocarps using values obtained videography. All statistical methods specified in the results were carried out using Matlab 2012b.

High-speed videography of free-falling sporocarps

Leaves containing mature sporocarps were were collected from a heavily infected *Calycanthus* bush on the University of California, Berkeley campus near Mulford Hall (37.87285°,-122.264078°). Leaves were cut into strips and strips were held taught between two alligator clamps with the bottom side of the leaf facing in the direction of gravity. Leaves were scraped with a small stiff-bristled brush on the side of the leaf not containing sporocarps (upper side) in oder to stimulate liberation through vibration. All experiments with live sporocarps were concluded within 120 min of collection.

The trajectories of descending sporocarps were viewed at 25x magnification

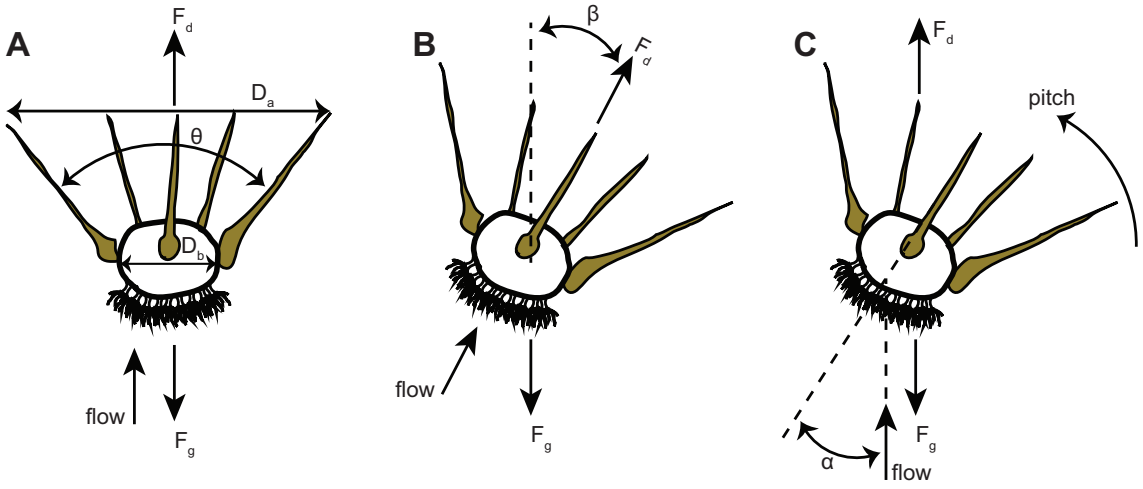

Figure 3.2: Diagrams of distance and angle measurements made on sporocarps. (A) Sporocarp falling straight down with no horizontal flow ($\beta = 0$, $\alpha = 0°$), with inter-appendage angle, θ, appendage-spread diameter, D_a, body diameter, D_b, and aerodynamic drag, F_d, labeled. (B) Sporocarp falling at a nonzero angle relative to gravity due to horizontal flow, but steady with no rotation ($\beta \neq 0$, $\alpha = 0$). (C) Sporocarp falling at an angle relative to flow and gravity while mid-rotation, but with no horizontal flow ($\beta = 0$, $\alpha \neq 0$), with resulting aerodynamic pitching moment labeled.

though a dissecting microscope turned on its side (Wild Heerbrugg M5A, leicamicrosystems.com), with illumination provided by the microscope's built-in base lamp. Video was recorded at 700 frames per second using a high speed color camera (Fastec

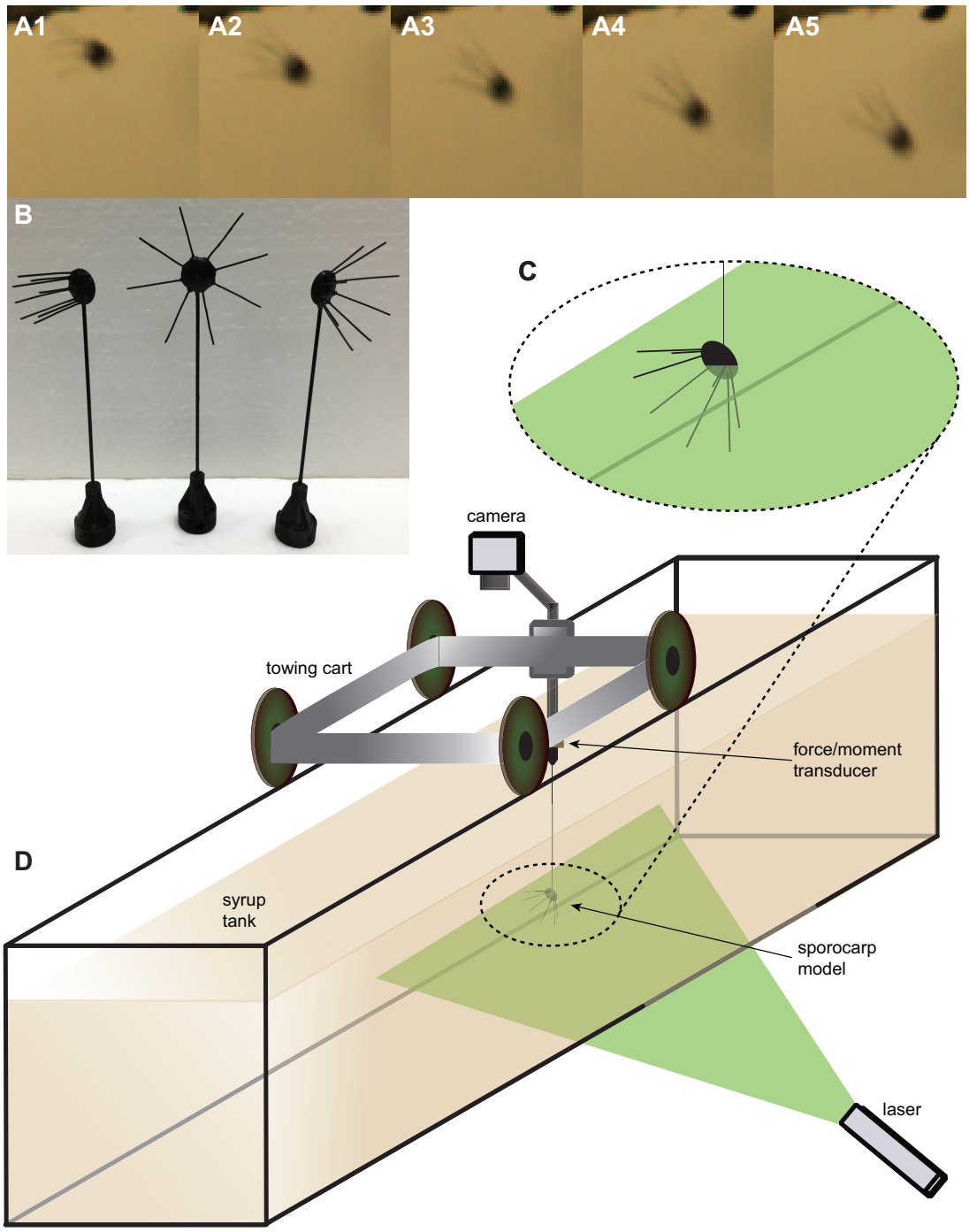

Figure 3.3: (A) Series of images exemplifying falling and rotating sporocarp (time step = 1.4 ms, sporocarp diameter $\approx$ 200 μm). (B) Dynamically scaled physical models (model diameters = 1.3 cm). (C) Zoom of model bisected by sheet of laser light, and showing vertical extender rod. (D) Tow tank used to measure forces and moments on models, and capture flow field around models using particle image velocimetry (PIV).

Hispec 1 Color camera, fastecimaging.com). Sections of the video were saved for analysis that clearly showed an individual sporocarp in free-fall, in which the path was in the focal plane and the radial appendages were clearly visible (n = 55). The lamp used produced heat, and many of the trajectories were not entirely vertical ostensibly as a result of convection currents (see Results).

Analysis of falling sporocarps was done frame by frame in imageJ. Static parameters measured for each of the 55 sporocarps were the body diameter, D_b, the appendage-spread diameter, D_a and the inter-appendage angle, θ (see Fig. 3.2A). Following liberation the position of the body center was tracked, which was used to calculate terminal velocity, defined as $\Delta(position)/\Delta(time)$ for frames in which $\Delta(velocity)/\Delta(time) \approx 0$. The rotation of the sporocarp was also tracked over time by making separate measurements of the angles made by the leftmost appendage relative to horizontal, ϕ and the rightmost appendage relative to horizontal, ζ. The body's angle relative to the direction of gravity was calculated by averaging $\phi - 0.5\theta$ and $\zeta + 0.5\theta$ — a method that reduced the error of this measurement. This angle relative to gravity was referred to as the off-set angle, β, and the majority of sporocarps had a nonzero offset angle once rotation was concluded (Fig 3.2B). The angle of attack, α was defined relative to the direction of flow as done with fluid-dynamic studies of shuttlecocks (e.g. Verma et al., 2013). The direction of flow was assumed to be aligned with β so that α was zero once rotation had ceased and a steady β was reached (see Fig. 3.2C). Thus each falling and rotating sporocarp had a single value of β, but values of α for each time step preceding steadiness. The angle of attack, α, was used to calculate angular velocity, $\omega = \Delta\alpha/\Delta(time)$, and angular acceleration, $\dot{\omega} = \Delta\omega/\Delta time$, for each frame. Fig. 3.3A1-5 shows an example of 7 ms of sporocarp rotation and descent from which kinematics measurements were obtained.

Dynamically scaled physical modeling and particle image velocimetry

Forces and moments were measured on dynamically scaled physical models of *Phyllactinia* sporocarps. The ellipsoidal models were designed in 3D modeling software (Blender 2.67a, blender.org), and printed on a multi-jet modeler (ProJet HD 3000 3-D Modeler, 3D Systems, Inc., Rock Hill, SC USA). The dimensions of the model were geometrically similar to sporocarps, based off of SEM (Hitachi TM-1000 SEM, Hitachi High Technologies America, Inc., hitachi-hta.com) and dissecting microscope images (Wild Heerbrugg M5A) (see Fig. 3.1C, D). The radial appendages were metal rods and glued into eight pilot holes symmetrically printed around the equator of the body and oriented with inter-appendage angles of 35°, 77°, and 180° (Fig. 3.3B). These angels were chosen because they were representative of the lower, middle, and upper third of the 55 recorded sporocarps ordered by their inter-appendage angle. All models contained a ninth metal rod attached to the ellipsoid equator and extending to a custom-printed fitting for a force transducer. This ninth rod affected the forces, moments, and flow field along its axis (vertical axis of the tow tank), but the radial symmetry of the models allowed for unaffected orthogonal measurements to the rod

with no loss of applicability to real sporocarps (Fig. 3.3C). Models, appendages, and extenders were rigid under all experimental conditions.

Models were dynamically similar to a Re range of 1.0 to 3.3 based on the characteristic length of the sporocarp (D_b = 200 μm), recorded terminal velocities of 8 to 26 cm/s, and the kinematic viscosity of air ($\nu = 1.57 \times 10^{5-}$ m^2/s). The models were printed at 65x scale of sporocarps, and thus to maintain desired Re range experimental flow velocities were 7.7 to 25 cm/s, and the fluid used was a mixture of Karo syrup and water with a kinematic viscosity $\nu = 9.7 \times 10^{-4}$ m^2/s (dynamic viscosity $\mu = 1.36$ Pa·s measured with rheometer (Brookfield DV3T, Brookfield Engineering Laboratories, brookfieldengineering.com), and density 1380 kg/m3 measured via volume and mass). Scaling allows for the ratio of velocities and forces relative to the model to be the same as to the sporocarp (Koehl, 2003), but with a much greater signal-to-noise ration than direct measurements on the sporocarp could achieve. Flow velocities were obtained by towing the model through a tank of Karo syrup mixed with water (Fig. 3.3D). The force transducer and model could be manually rotated so that the orientation of the model with respect to the flow was experimentally varied. The tank was built of clear acrylic plastic and supported by aluminum framing. The towing was achieved by a belt driven cart controlled by a stepper motor (see Munk, 2011 for specifications). The maximum appendage-spread diameter, D_a, was kept small relative to the tank width to insure no wall effects on the fluid interacting with the model (Loudon et al., 1994).

Flow visualization was achieved through particle image velocimetry (PIV). A horizontal sheet of green laser light (300 mW, 532 nm Wicked Lasers S3 Krypton, wickedlasers.com) illuminated silver-coated hollow glass tracer beads (Potter Industries, pottersbeads.com) seeded throughout the tank and minimally buoyant in the Karo-water mix. The motion of the tracer beads was filmed at 60 fps using a video camera (Fastec Hispec 1). The analysis of frames was done in PIVlab run on Matlab v7.1 (Thielcke and Stamhuis, 2014).

Models were connected via an the aforementioned extender rod (see Fig. 3.3C), and fitting to a six-axis force and moment transducer (ATI Nano17 transducer, ati-ia.com) were the signal from the transducer was acquired by PCI-6220 DAQ at 1000Hz. Only the 1.5s of forces and moments that occurred during the middle of the tow were saved, as these measurements represented the steady state flow. The force acting on the extender and fitting was measured, averaged, and subtracted from all force and moment results. The center of mass of a sporocarp was calculated, then scaled to that of the model, and then the distance between that calculated center of mass and the transducer was measured. The center of mass correction was

$$\tau_{\mathbf{CM}} = \tau_{\mathbf{FT}} - \mathbf{r} \times \mathbf{F} \tag{3.7}$$

where $\tau_{\mathbf{CM}}$ was the vector of torque exerted about the center of mass of the model, $\tau_{\mathbf{FT}}$ was the measured vector of torque, $\mathbf{r}$ was the vector between the transducer and center of mass of the model with length described above, and $\mathbf{F}$ were the vectors of force measured by the transducer.

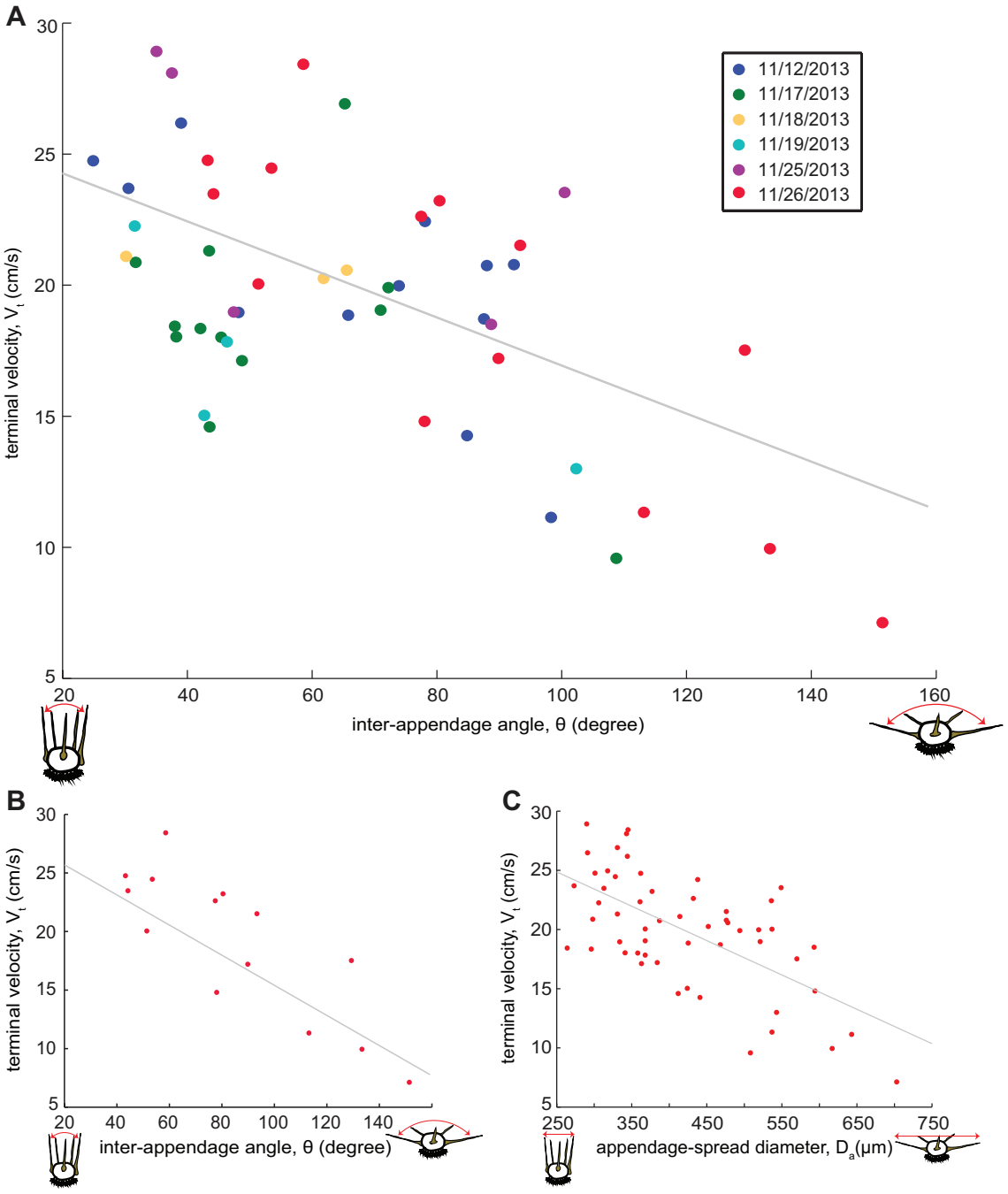

Figure 3.4: Scatter plots of terminal velocity, V_t as function of inter-appendage angle, θ (A-B), and appendage-spread diameter, D_a (C). Sporocarps liberated from a given leaf on a given day are indicated by color in (A) as shown in legend, and (B) shows only sporocarps from a single leaf collected on 11/26/2013. Sporocarp sketches on horizontal axes represent range of angle *theta* (A-B), and D_a (C). Gray lines on all plots show linear regressions.

RESULTS

Terminal velocity

Measured terminal velocities for individual sporocarps were compared against individual inter-appendage angles, θ, body diameters, D_b, and appendage-spread diameters, D_a, for the purpose of determining if terminal velocity was dependent on any of these geometric parameters of sporocarps (see Fig. 3.4). Appendage-spread diameter, D_a, showed the greatest correlation with V_t ($R^2 = 0.405$, RMSE = 0.038) (Fig. 3.4C). However, D_a was not a parameter that could be easily manipulated with models, because it captures two parameters, appendage length and inter-appendage angle. Thus, inter-appendage angle, θ, was considered the physical parameter of real sporocarps that directed subsequent modeling experiments. The correlation between θ and V_t has $R^2 = 0.340$, RMSE = 0.040 (Fig. 3.4A). Obviously, variables other than θ alone had an effect on a sporocarp's terminal velocity. In fact, individual leaves, or alternatively the date a leaf was collected, seemed to have an effect on measured V_t. For example,

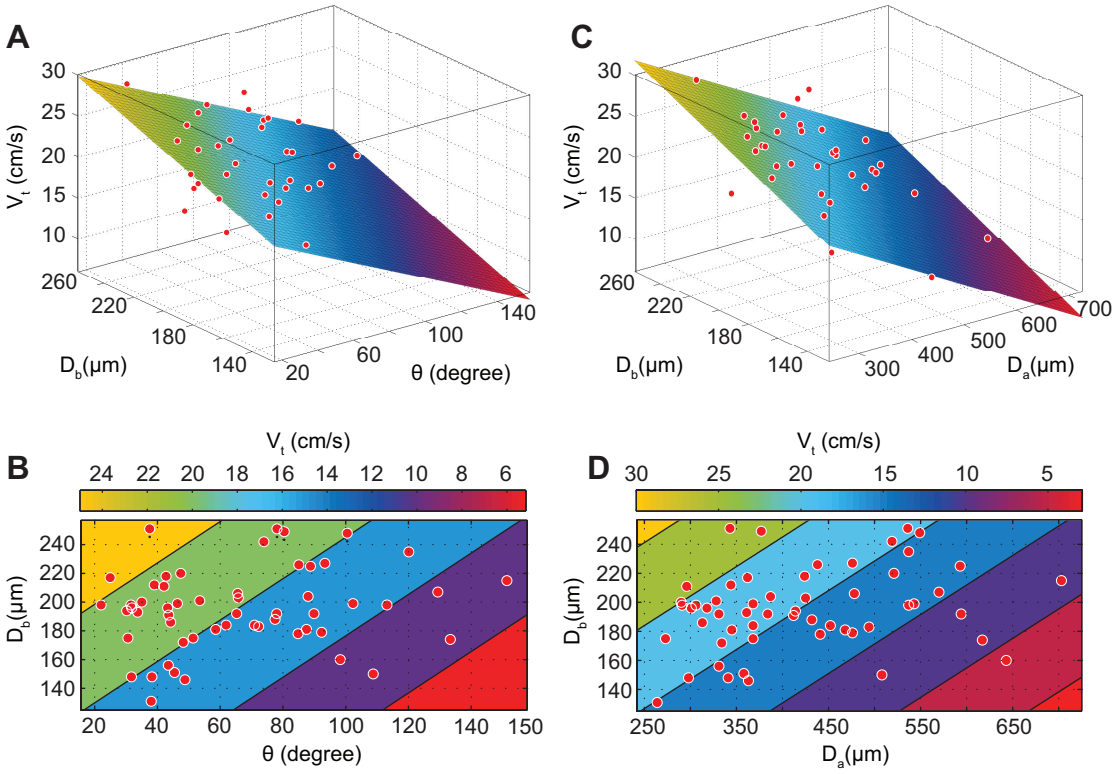

Figure 3.5: (A) 3D scatter plot of inter-appendage angle, θ versus body diameter, D_b, versus terminal velocity, V_t, showing fitted linear surface, and (B) corresponding contour plot. (C) 3D scatter plot of appendage-spread diameter, D_a, versus D_b versus V_t showing fitted linear surface, with (D) corresponding contour plot.

11/17/2013 and 11/19/2013 each show values of V_t consistently less than comparable sporocarps from other days. For November 26^{th}, θ versus V_t has an R^2 of 0.697, RMSE = 0.036 (Fig 3.4B), implying that if the variation between leaves is removed perhaps θ is a better predictor of V_t than it appears. Body diameter, D_b was a very poor predictor of V_t with an R^2 of only 0.083, RMSE = 0.047 (not shown in figure).

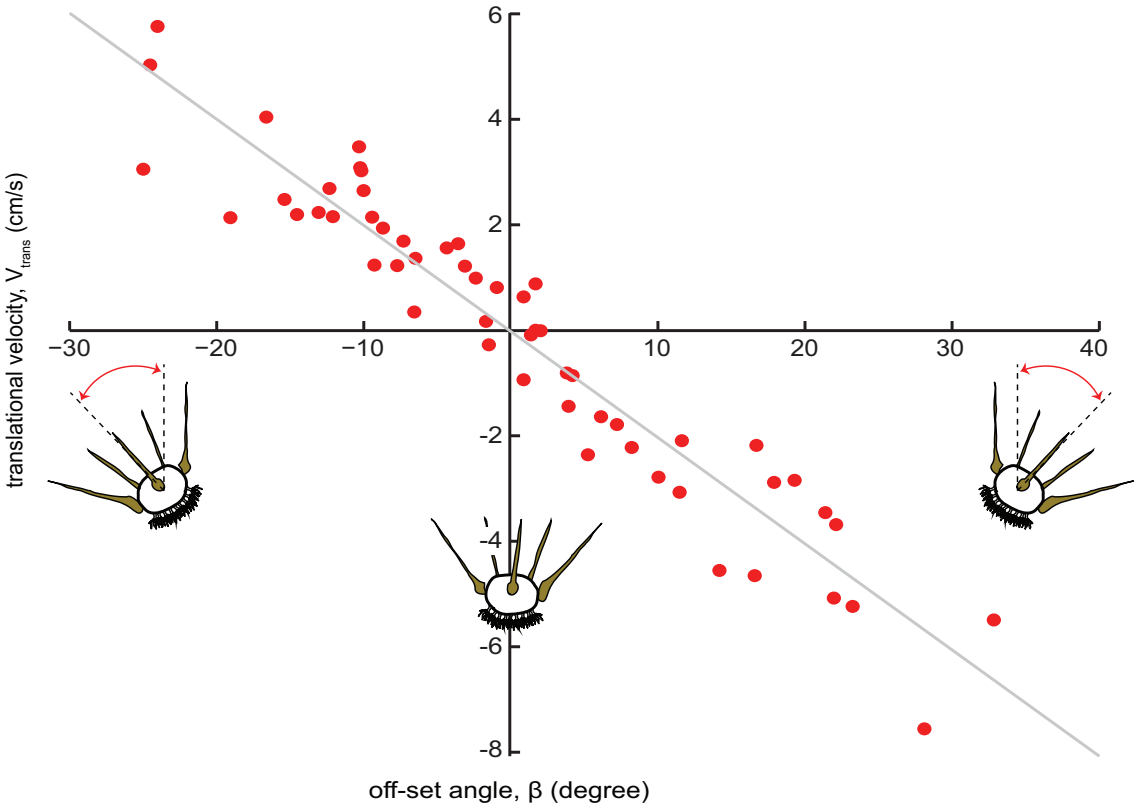

Figure 3.6: Scatter plot showing translation velocity, V_{trans}, as a function of off-set angle, β, with linear regression shown as gray line and sporocarp sketches representing range of β.

To see if a combination of parameters gave an improved correlation to terminal velocity, V_t, both θ and D_a were combined with D_b and plotted against V_t (Fig. 3.5). Despite D_b having no significant correlation to V_t on its own, when combined with either θ or D_a it improved correlations with V_t. Terminal velocity as a function of inter-appendage angle, θ, and body diameter, D_b shows a correlation that explains approximately half of the variation in V_t ($R^2 = 0.511$, RMSE = 0.035). Terminal velocity as a function of the two measured diameters, D_a and D_b, shows the strongest correlation (R^2 of 0.644, RMSE = 0.030). Thus, body diameter combined with appendage-spread diameter are the best predictor of terminal velocity of all measured parameters in this study.

Since many of the freely falling sporocarps did not reach a final orientation in which their long axis was aligned with gravity, but instead finished rotating at an angle termed the off-set angle, β (see Methods), it was important to correlate this angle with translational velocity, V_{trans}. Fig 3.6 shows a strong correlation between both magnitude and direction of β and V_{trans} ($R^2 = 0.913$, RMSE $= 0.009$). Off-set angle is a very strong predictor of translational velocity, and thus the direction of flow following rotation is always assumed to be aligned with the long axis of the sporocarp (the definition of $\alpha = 0°$ used in this study). The off-set angle, β, is in no way correlated with V_t (R^2 of 0.008).

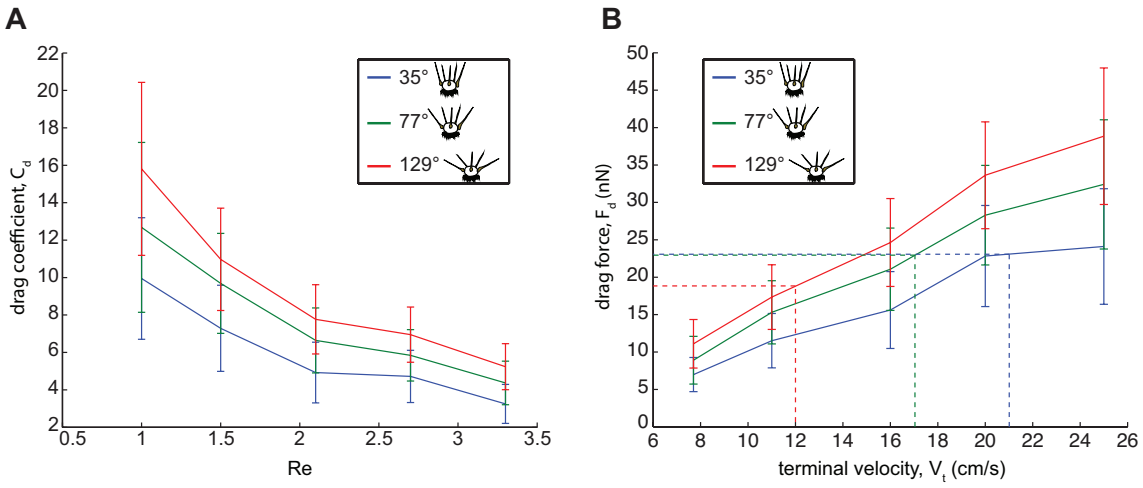

Figure 3.7: (A) Drag coefficient, C_d versus Re for three modeled morphologies as indicated in legend. (B) Drag force, F_d acting on sporocarps in air versis V_t. Error bars represent σ (n =5). Dotted lines in (B) show average V_t and F_d for each morphology.

With the information garnered from filmed sporocarp descents, modeling was used to explain observed correlations with physical mechanisms, and derive semi-empirical equations fit to V_t. The three chosen biologically-representative sporocarp models all had identical length appendages and D_b but differed in inter-appendage angle, θ (35°, 77°, and 129°, see Methods). The drag coefficient, C_d, as a function of Re is shown in Fig. 3.7A. The drag coefficient is

$$C_d = \frac{2F_d}{\rho S_w U^2} \tag{3.8}$$

where F_d is the drag force, ρ is the fluid density, S_w is the sporocarp surface area (calculated as ellipsoid and circular cylinders with $S_w = 1.86 \times 10^{-7}$ m^2 for sporocarps), and U is the fluid flow velocity. As expected, C_d decreases as Re increases (see Vogel, 1996). When C_d is compared between model morphologies at a particular Re there is no significant difference (ANOVA, Tukey, p ≈ 0.09), even though larger θ does result

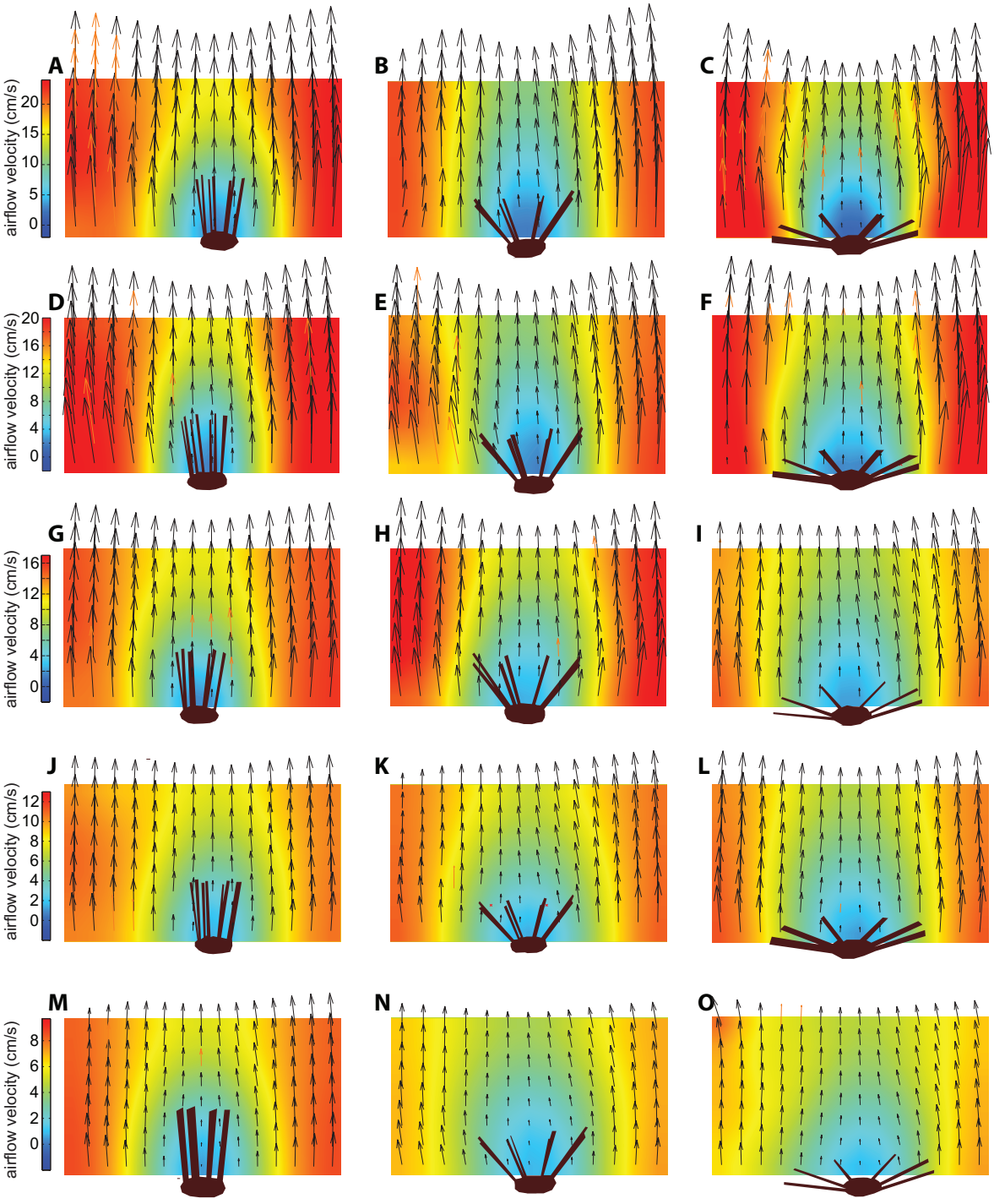

Figure 3.8: Particle image velocimetry for all models (β of 35°, 77°, and 129°) at all tested velocities at zero angel of attack ($\alpha = 0$). (A-C) Models at V_t of 26 cm/s. (D-F) Models at V_t of 21 cm/s. (G-I) Models at V_t of 17 cm/s. (J-L) Models at V_t of 12 cm/s. (M-O) Models at V_t of 8 cm/s. All vectors are the same scale, and colormaps are set to scale of each V_t.

in higher average C_d. However, if C_d is compared between models operating at the Re determined by the avergae V_t at which that morphology falls (Re = 2.7 for 35°, Re = 2.1 for 77°, Re = 1.5 for 129°), then the 129° morphology has a significantly higher C_d than 35° and 77° (ANOVA, Tukey, $p < 0.05$). Orientation with respect to the flow had no effect on any of the models at any of the flow velocities (ANOVA, Tukey, $p \approx 0.95$), which supports the video evidence that off-set angle, β does not correlate with V_t.

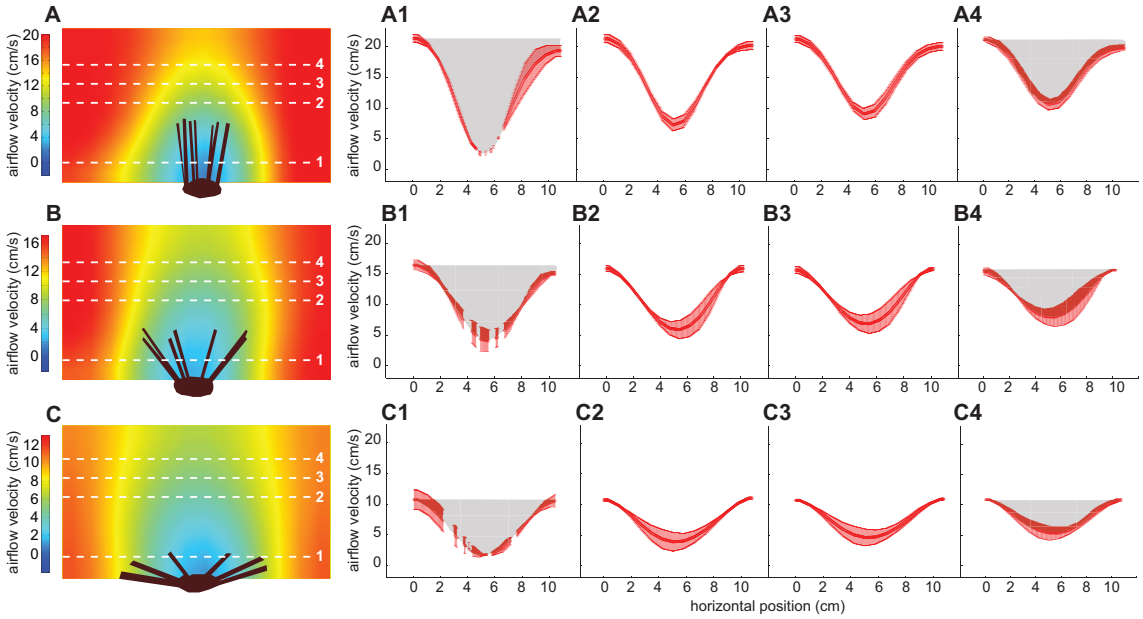

Figure 3.9: (A) PIV colormap for 35° morphology at characteristic V_t of 21 cm/s with velocity profiles 100, 500, 600, and 700 μm downstream from body (A1-A4). (B) PIV colormap for 77° morphology at characteristic V_t of 17 cm/s with velocity profiles 100, 500, 600, and 700 μm downstream from body (B1-B4). (C) PIV colormap for 129° at characteristic V_t of 12 cm/s with velocity profiles 100, 500, 600, and 700 μm downstream from body (C1-C4). Error bars on velocity profiles represent σ (n=3). Gray shading explained in text.

The calculated drag, F_d, acting on freely-falling sporocarps in air was plotted against a range of terminal velocity for the purpose of determining the proportionality between F_d and V_t, and to compare F_d to gravitational forces. The drag force was found by solving for F_d in Eqn. 3.8 using the density of air ($\rho = 1.18$ kg/m^3), the surface area of a sporocarp ($S_w = 1.86 \times 10^{-7}$ m^2), the recorded values of V_t, and C_d obtained through dynamically scaled physical modeling. Fig. 3.7B shows F_d as a function of V_t for the three morphologies, and the F_d appears to have a linear dependence on V_t, ($R^2 = 0.985$), as opposed to $F_d \propto V_t^2$ ($R^2 = 0.536$). The values of V_t that each sporocarp morphology was most likely to fall were 26 cm/s, 21 cm/s, and 17 cm/s for 35°, 77°, and 129°, respectively (based on videography). The corresponding values of F_d are shown

in Fig 3.7B, ranging between 19 and 23 nN. The flow fields resolved around the three tested sporocarp shapes provide further support that inter-appendage angle, θ, affects the surrounding fluid, drag force acting on the sporocarp, and resulting terminal velocity, V_t (see Fig. 3.8). At any given V_t, sporocarps with wider-spread appendages, larger θ thus larger D_a, have a correspondingly greater wake width. It is also apparent that some airflow passes through the appendages of sporocarps with $\theta = 77°$, and $\theta = 129°$, and that the relative amount of observed flow through the appendages of these sporocarp shapes is dependent on V_t (compare 3.8B, E, H, K, N and 3.8C, F, I, L, O). However, no airflow passes through the appendages of sporocarps with $\theta = 35°$ due to the distance between the appendages and their angle relative to the flow.

With the purpose to further understand the flow around each sporocarp morphology at its most probable velocity, as mentioned above, velocity profiles were taken at consistent distances downstream from the sporocarp body (Fig. 3.9). A momentum defect can be estimated by considering the area between a horizontal line at V_t and the curve of a velocity profile. The shaded areas in Fig. 3.9A1, A4, B1, B4, C1, and C4 represent momentum defects. The ratio between a momentum defect immediately behind a sporocarp and one further downstream indicates how rapidly the wake is dissipating. This ratio normalizes for V_t so that that wake lengths can be compared across velocities, as is the case in Fig. 3.9. The 35° morphology has a ratio of 0.51 between the momentum defect at 100 μm behind the sporocarp and that at 700 μm downstream (ratio of areas A4:A1). The same ratio for the 77° morphology is 0.64, and for the 129° morphology it is 0.76. Thus, the relative wake for the the sporocarps with larger inter-appendage angels, θ, are more persistent and extend further downstream than for sporocarps with smaller θ.

Using the observations made regarding wake widths using PIV, and the obtained drag coefficients, C_d, semi-empirical formulas were fitted to actual sporocarp terminal velocities, V_t. Three fitting formulas were compared to V_t. The first two were modifications on a Stokes' law approximation of terminal velocity (Eqn. 3.3), with the first assuming no air flow through the sporocarp appendages and defined as

$$V_t = \frac{\mathcal{V}_s \rho_s g}{6\pi\eta D_a} \tag{3.9}$$

where $\mathcal{V}_s$ is the volume of the sporocarp (calculated with individually measured values of D_b and assumption of ellipsoid with cylindrical appendages), and ρ_s is the density of the sporocarp (based on wight measurements (see Chapter #2), and average $\mathcal{V}_s$). This formula is called the "Stokes-full-D_a." Its counterpart is the "Stokes-operational-D_a," which instead of using D_a for each sporocarp uses $0.5D_a$ or the body diameter, D_b, taking the larger of the two. This approach is justified by the the fact that widely-spread appendages partially admit airflow (see Fig. 3.8), but narrowly-spread appendages do not extend beyond the wake of the upstream sporocarp body. These two formula are plotted alongside actual V_t in Fig. 3.10A.

Since sporocarps falling at V_t operate at Re between 1.0 and 3.3, it is also reasonable that the Newton quadratic-drag model of terminal velocity will be a good fit to

actual V_t (Eqn. 3.4). The values of drag coefficients,C_d, used to fit Eqn. 3.4 to actual V_t were those collected from modeling (see Fig. 3.7A). The projected area, S_p was calculated from individually measured values of sporocarp body diameters, D_b, (see Fig. 3.5 for range) and assuming the projection was circular. This formula is called "Newton-operational-C_d" and is plotted alongside actual V_t in Fig. 3.10B.

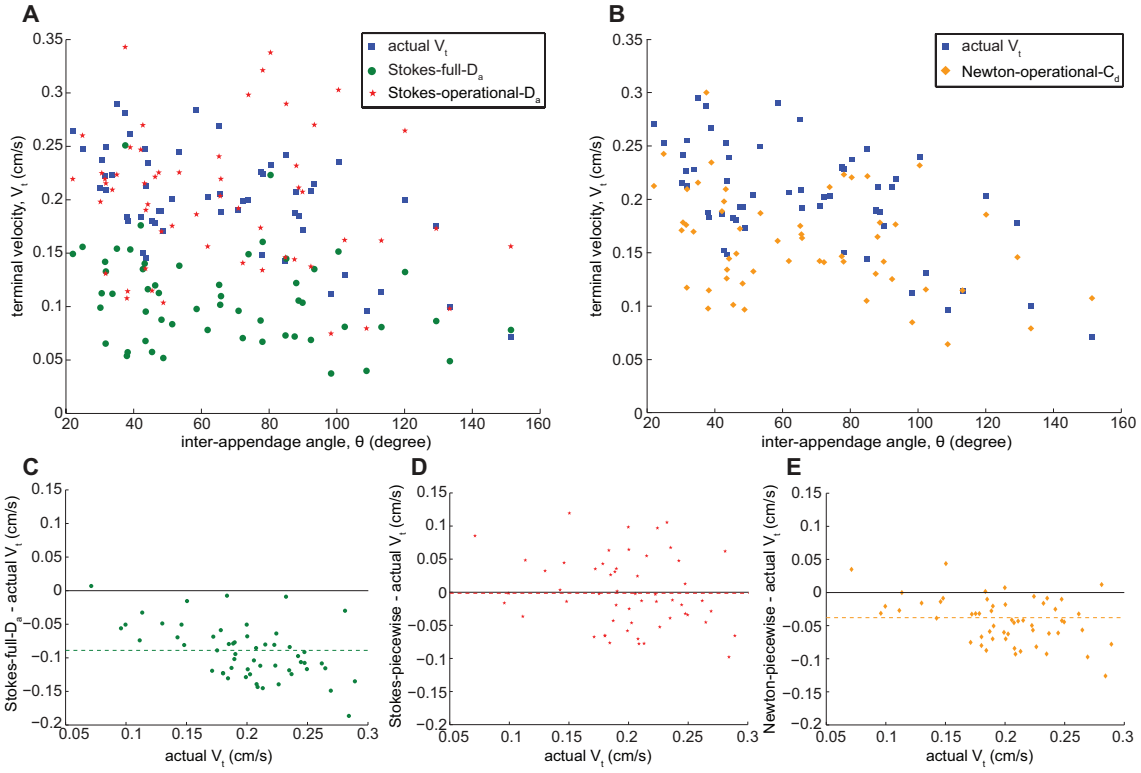

Figure 3.10: (A) Comparisons of actual V_t and two formula fitting V_t using Stokes' law (Eqns. 3.3 & 3.9). (B) Comparison of actual V_t and formula fitting V_t using quadratic drag (Eqn. 3.4). (C-D) Simple Bland-Altman plots showing error between fitting formulae and actual V_t. Dotted lines in (C-D) show averages of error and underestimation of "Stokes-full-D_a" (C) and "Newton-piecewise" (E) formulae, as well as accuracy of "Stokes-piecewise" (D).

Both "Stokes-full-D_a" and "Newton-operational-C_d" underestimate V_t. Furthermore, there two formulae have slopes that are not equal to the regression of actual V_t, as indicated by the increasing difference between the calculated V_t and actual V_t as a function of actual V_t (see Fig. 3.10C, E). "Stokes-operational-D_a," however, shows much greater accuracy and homogenous error with respect to actual V_t (Fig. 3.10D). Despite the accuracy of "Stokes-operational-D_a" as a formula describing V_t, it shows less precision than the less accurate "Newton-operational-C_d" (comparing the vertical range of error between 3.10D and E).

Aerial righting and stability

Instantaneous angular velocity, ω, was measured as a function of angle of attack, α, for freely falling sporocarps captured with high speed videography (Fig. 3.11A) to see if sporocarps would conclude rotation upon reaching $\alpha = 0°$ (see Methods). The same 55 sporocarps described whose terminal velocity is described above were used to quantify aerial righting. In fact, these sporocarps represent a small subset of a much larger set of recorded sporocarp descents, but are those for which a significant amount of rotation occurred and was clearly visible. Angular velocity was binned into increments of α 10 degrees in width, and because not all sporocarps passed through larger values of α the larger error for these values of α are partially due to smaller sample sizes. Furthermore, the large amount of variation shown in ω is a result of sporocarps undergoing simultaneous vertical acceleration or deceleration while rotating, and from not all beginning their descent at the same angle. However, ω does approach zero as α approaches zero for all the recorded sporocarps (insert in Fig. 3.11A shows typical trajectories in ω-α space). Instantaneous angular velocity, ω at $\alpha = 10°$ is significantly lower than ω at all other values of α except 20° and 110° (ANOVA-Tukey, $p<0.05$). Real sporocarps slow in their angular velocity as they reach their hypothesized aerodynamically-stable orientation — evidence of passive aerial righting.

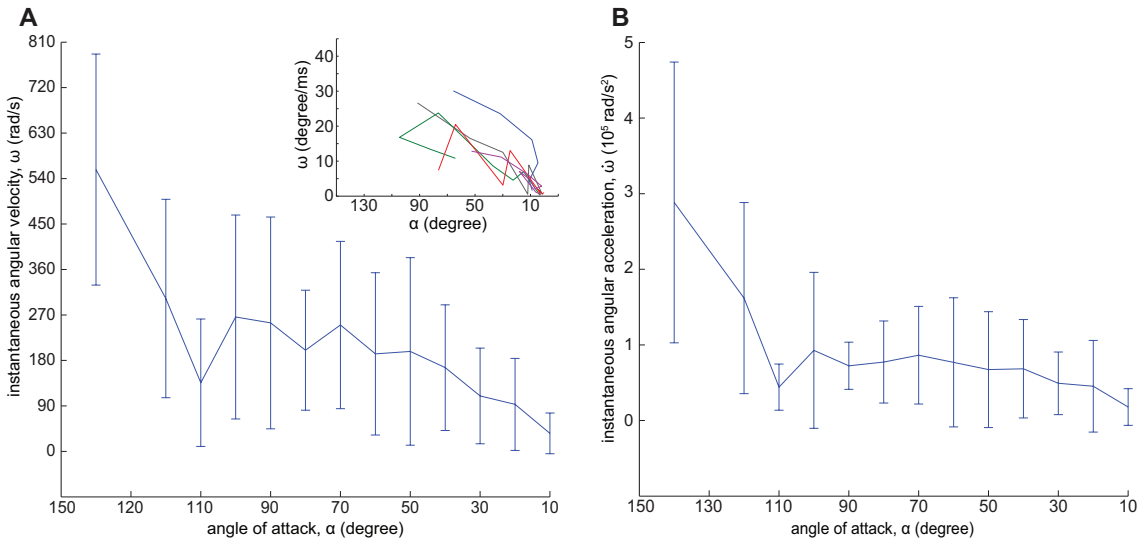

Figure 3.11: (A) Binned angular velocity, ω, versus angle of attack, α, with insert showing examples of individual sporocarp trajectories taken at timesteps of 1.4 ms. (B) Binned angular acceleration, $\dot{\omega}$, versus α. Error bars represent σ.

Instantaneous angular acceleration, $\dot{\omega}$, was also binned and compared across values of α (Fig. 2.11B). The purpose of plotting $\dot{\omega}$ against α was to see if angular acceleration

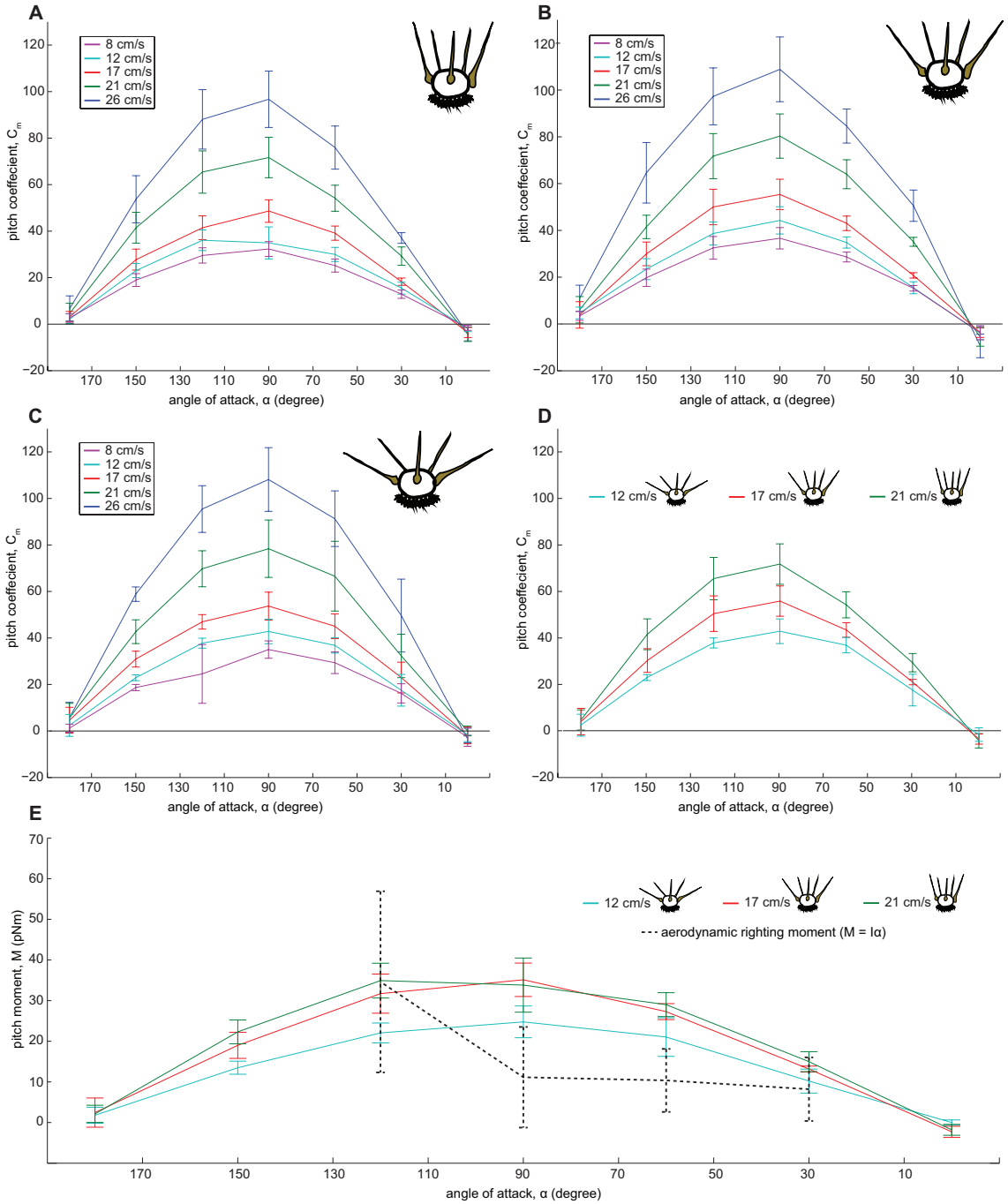

Figure 3.12: (A-C) Pitch coefficients, C_m, as functions of angle of attack, α, for full V_t range, as indicated in the legends, with (A) sporocarp possessing $\theta = 35°$, (B) 77°, (C) 129°. (D) C_m versus α for characteristic V_t of each morphology. (E) Pitch moment in pNm acquired through modeling and calculated for actual sporocarps compared to empirically acquired aerodynamic righting moment (dotted line). All error bars represent σ.

also decreased as angle of attack approached zero, and to capture the full range of $\dot{\omega}$ that is representative of a rotating sporocarp. Angular acceleration, $\dot{\omega}$, at $\alpha = 10°$ was significantly lower than at all other angles of attack, except 20°, 30°, and 110° (ANOVA-Tukey, $p<0.05$). Rotation of sporocarps appears to be decelerating as it approaches $\alpha = 0°$. The angular accelerations that sporocarps undergo are on the order of 10^5 rad/s^2, which, although dramatic, is consistent with the observation that rotations were always completed in less than 20 ms, and with the inverse proportionality $\dot{\omega} \propto M/I \propto L^{-2}$.

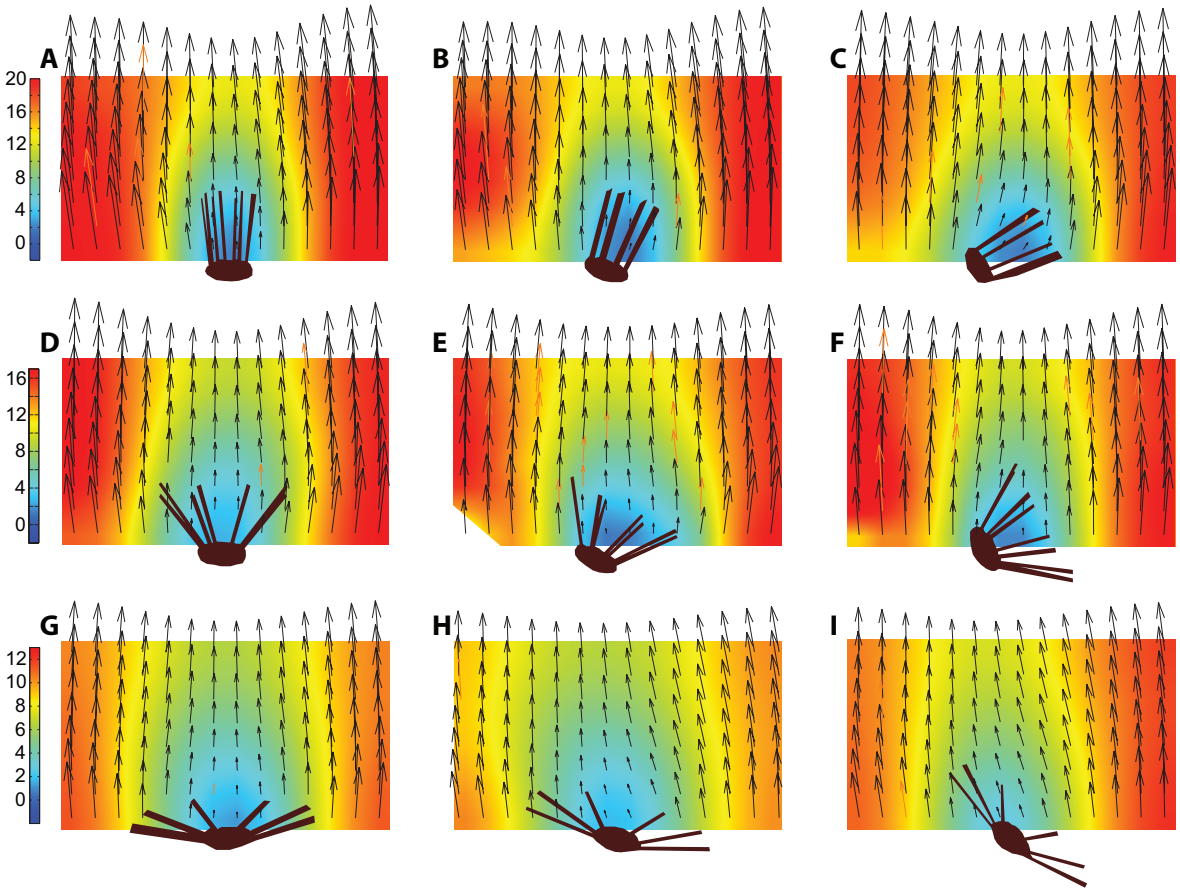

Figure 3.13: PIV of sporocarps at three angles of attack. Sporocarp with $\theta = 35$ at $\alpha = 0°$ (A), $\alpha = 30°$ (B), and $\alpha = 60°$ (C). Sporocarp with $\theta = 77$ at $\alpha = 0°$ (D), $\alpha = 30°$ (E), and $\alpha = 60°$ (F). Sporocarp with $\theta = 129$ at $\alpha = 0°$ (G), $\alpha = 30°$ (H), $\alpha = 60°$ (I).

Using physical models, pitch coefficients and pitching moments were measured for sporocarps as a function of α (Fig. 3.12), to determine if sporocarps were aerodynamically stable. The equation for the aerodynamic pitching moment is

$$M = 0.5 C_m \rho S_w U^2 L \tag{3.10}$$

where C_m is the shape-dependent pitch moment coefficient, and L is the characteristic length of the sporocarp (D_b). Fig. 3.12A, B, C, D show C_m versus α where the slope of the relationship is indicative of stability. If $C_m/\alpha > 0$ then the sporocarp is unstable, and any perturbation exerted on the sporocarp by the surrounding air will cause an increase in the moment acting on the sporocarp. If $C_m/\alpha < 0$ then the sporocarp is stable, and if perturbed the result will be a decrease in the aerodynamic moment, M. Furthermore, if $C_m = 0$ at a particular α then the local slope determines if this is a unstable fixed point ($C_m/\alpha > 0$) or a stable fixed point ($C_m/\alpha < 0$) (Koehl et al., 2011). For the three tested morphologies (35°, 77°, 129°), and across the range of observed terminal velocities (8 - 26 cm/s), sporocarps have a stable fixed point at $\alpha = 0°$ (Fig. 3.12A, B, C, D). None of the morphologies show an unstable fixed point at $\alpha = 180°$, but instead show small values of C_m. The greatest values of C_m occur when $\alpha = 90°$, as sporocarps are transitioning from unstable angel of attack to stability and an approach to their stable fixed points.

The effects of V_t and morphology on C_m are both dependent on angle of attack. At the least-stable angle of attack, $\alpha = 90°$, C_m is statistically different for each value of V_t for all morphologies (ANOVA-Tukey, $p<0.05$). However, as α approaches both 180° and 0°, C_m collapses to a single value independent of V_t. Similarly, if the three morphologies (θ of 129°, 77°, and 35°) are compared at the biologically-representative terminal velocity of each (12cm/s, 17 cm/s, and 21 cm/s) then C_m is statistically different for each shape at angles of attack of 60°, 90°, and 120°, but not for lower or higher α (ANOVA-Tukey, $p<0.05$) (see Fig. 3.12D). If sporocarp shape is compared at a fixed value of α then there is no effect on C_d.

The moment of inertia for an average sporocarp was approximated by an ellipsoid that enveloped the sporocarp (axes 250 μm and 200 μm in length, $\rho = 1000$ kg/m^3), and that was free to rotate about its vertex. This approximation yields $I = 1.2 \times 10^{-16}$ kg·m^2, and can be multiplied by the angular accelerations presented in Fig. 3.11 to arrive at a estimate of the aerodynamic moment necessary to create such observed $\dot{\omega}$. This empirically derived moment is compared against the modeled moments in Fig. 3.12E. Comparisons were made at the four values of α for which both model and videography results were collected (30°, 60°, 90°, and 120°). It is apparent that $M = I\alpha$ is less than modeled M at $\alpha = 60°$ and 90°, and instead of showing a peak at 90° is greatest at 120°. However, modeled and empirical pitching are in good agreement at angles of attack of 30° and 120°, and nearly agree within error across α.

The flow fields around sporocarp models show asymmetric flow around titled sporocarps (Fig. 3.13). For the 35° and 77° morphologies the high-pressure, low-velocity region moves with the appendages as α increases, whereas for the 129° morphology the appendages do not seem to significantly obstruct flow. In fact, the variation between the wakes of the three morphologies is much more pronounced at nonzero angles of attack.

DISCUSSION

Terminal velocity

Terminal velocity, V_t affects dispersal distance (see Eqn. 3.5), and thus it is important to determine if the shape of *Phyllactinia* sporocarps affect V_t. Sporocarps with their radial appendages fall slower than spheres of equal diameter and comparable density. In fact, the peak V_t sporocarps reached (those only achieved by sporocarps with $\theta < 80°$) is less than half that of a 200 μm sphere (see Fig. 3.4) (Dennis, 1976). Furthermore, sporocarps with wider-spread appendages, and larger inter-appendage angles fell slower (Fig. 3.4), but such correlations were significantly improved by considering the body diameter of sporocarps, which showed that sporocarps with larger bodies fell faster (see Fig. 3.5). Shape has a definitive effect on V_t at this Re range of 1.0 to 3.3, with spheres falling fastest at ~70 cm/s, sporocarps falling at velocities between 8 and 28 cm/s, and both falling faster than cigar-shaped orchid seeds at similar Re (Murren and Ellison, 1998).

The drag forces and drag coefficients obtained with physical modeling were validated by comparing F_d to mg (see Fig. 3.7). Although modeled values of F_d do not agree perfectly with the gravitational force based on a measured average sporocarp mass of $m_s = 1.5$ μg (see Chapter #2), the gravitational force and F_d do agree quite well within the error of F_d and m_s. The values of F_d presented in this study suggest a slightly more massive spore than direct measurements of m_s.

At this near-unity Re range two equations can be used to calculate V_t (Eqns. 3.3 and 3.4). The best fit to measured values of V_t was that based on Stokes' law, but only when an operational D_a was used that accounted for flow through the widest spread appendages (see Fig. 3.10). The notion that the aerodynamic diameter of a sporocarp during free-fall may be less than D_a is supported by flow-field visualizations around models (see Fig. 3.8 and 3.9). The Re range of flow around individual appendages is 0.05 to 0.2, and in this range the ratio of cylinder diameter to gaps between cylinders has a strong effect on leakiness, defined as the flow permitted through an array of cylinders as a proportion of the flow in the absence of any obstruction (Cheer and Koehl, 1987). Estimations for leakiness of sporocarp morphologies suggest that when the inter-appendage angle θ is 35° no more than 30% of air can pass through the appendages. However, when $\theta = 129°$ 40% to 75% of air can pass through appendages as they spread radially outward. This large variation in airflow between sporocarp's appendages, dependent on both V_t and morphology, is a reasonable mechanism explaining how simple cylindrical appendages can have a salient effect on aerodynamics.

Aerial righting and stability

The life cycle of *Phyllactinia* is dependent on successful aerial righting and stability of sporocarps during transport so that deposition occurs with appendages facing

upward (Cullum and Webster, 1977). The results of this study found that sporocarps exhibit a gradually decreasing angular velocity as they approach their stable fixed point (see Fig. 3.11, and 3.12 for evidence of stability). The flow fields around sporocarp models provide further qualitative support of sporocarp aerial righting by showing the asymmetric flow around titled sporocarps (Fig. 3.13). All tested sporocarp morphologies appeared equally stable, but sporocarps with small values of θ were subjected to greater moments when falling at their characteristic V_t, implying that this morphology would conclude aerial righting in less time than sporocarps with wide spread appendages. Sporocarps do not continue to oscillate, wobble, or autorotate after they attain an angle of attack of zero, and as such display no indication of generating lift in the manner of samaras (Norberg, 1973).

The magnitude of pitching moments obtained through physical modeling can be validated by comparing them to the aerodynamic-righting moment obtained through Eqn. 3.6 ($I = 1.2 \times 10^{-16}$ kg·m^2). The agreement between modeled and empirical moments (see Fig. 3.12E) strongly suggests that physical modeling captured an accurate description of the fluid-dynamics acting on a sporocarp. Furthermore, this implies that an aerodynamic moment may provide a full explanation of aerial righting, with the effects of an inertial moment about the center of mass being negligible.

As the Re decreased to the lowest Re relevant to this study (Re = 1.0) the magnitude of sporocarp pitch coefficients, C_m, in the most unstable orientations ($\alpha = 60^\circ - 120^\circ$) decreased rapidly. This may suggests that the shape of sporocarps would no longer cause rotation at lower Re (see Fig. 3.12). Furthermore, sub-millimeter propagules and organisms experience very high angular velocities, since even a small aerodynamic moment has a large effect on the tiny moments of inertia intrinsic at their length scale (see Eqn. 3.6), but sufficiently small propagules would need increasingly dramatic morphologies to experience any aerodynamic moment due to increasing viscous effects as Re decreases. Sporocarps may represent the lower size limit at which aerial righting is possible, but nonetheless they seem analogous to macroscopic shuttlecocks, and, more directly, to free-falling aphids and ants that assume a fixed posture during descent that places the center of drag downstream from the center of mass (Ribak et al., 2013; Yanoviak et al., 2011).

Trade-off between terminal velocity and aerial righting

Sporocarps with an inter-appendage angle of $\theta = 35^\circ$ have the largest aerodynamic moments acting on them (Figs 3.12 and 3.13), but they are also more likely to have a higher V_t. This leads to the question of whether there exists a biological trade-off between terminal velocity and rate of aerial righting. Indeed, in an ambient wind of 3 m/s and starting at a height of 1 m, the slowest falling sporocarps (those more likely to have large θ) will be transported 38 m according to a simplistic dispersal equation (Eqn. 3.5), whereas sporocarps with the greatest V_t (those more likely to have small θ) will only be transported 10 m. Conversely, sporocarps with $\theta = 35^\circ$ are acted upon by aerodynamic moments 1.5 times greater than those on sporocarp with $\theta = 129^\circ$, which

suggests faster rotations for narrower morphologies. However, the difference in rotation times is on the order of milliseconds (Fig. 3.11), and completed over vertical distances on the order of centimeters. This may, in fact, be biologically relevant since eddies in turbulent natural conditions within vegetation are comparable in size to sporocarps ($\sim$500 μm) (Finnigan, 2000; van Hout, 2007). Such eddies could dramatically reorient sporocarps and necessitate frequent and repeated aerial righting before deposition is completed.

The natural variation in sporocarp morphology affects biologically important aspects of performance. Aerial righting, dispersal distance, and likelihood of being liberated prior to transport (see chapter # 2), are all affected by the length and angle of radial appendages. There appears to exist competing demands for sporocarps to be tall with small inter-appendage angles (more likely to be liberated by wind and reorient quickly) and short with large inter-appendage angles (more likely to disperse long distances), and perhaps both morphological extremes are necessary for the survival of the fungus. The aerodynamic principles that apply to *Phyllactinia* sporocarps apply to the family of powdery mildews, all of which have radial appendages serving a variety of hypothesized functions (Glawe, 2008), and are applicable to small flightless insects, and parachuting spores.

References

Abelson, A. (1997). Settlement in flow: Upstream exploration of substrata by weakly swimming larvae. *Ecology* **78**, 160–166.

Abelson, A. and Denny, M. (1997). Settlement of marine organisms in flow. *Annual Review of Ecology and Systematics* **28**, 317–339.

Ackerman, J. (1997). Submarine pollination in the marine angiosperm *zostera marina* (zosteraceae) . 2. pollen transport in flow fields and capture by stigmas. *American Journal of Botany* **84**, 1110–1119.

Ackerman, J. (2000). Abiotic pollen and pollination: ecological, functional, and evolutionary perspectives. *Plant Systematics and Evolution* **222**, 167–185.

Alexander, R. (1971). *Size and Shape*. Number 29 in The Institute of Biology's Studies in Biology. Edward Arnold Limited.

Alexopoulos, C., Mims, C. and Blackwell, M. (1996). *Introductory Mycology*. New York: Wiley, 4th edition.

Alve, E. (1999). Colonization of new habitats by benthic foraminifera: a review. *Earth-Science Reviews* **46**, 167–185.

Ambler, J., Cloern, J. and Hutchinson, A. (1985). Seasonal cycles of zooplankton from san francisco bay. *Hydrobiologia* **129**, 177–197.

Andersen, M. (1993). Diaspore morphology and seed dispersal in several wind-dispersed asteraceae. *American Journal of Botany* **80**, 487–492.

Arditti, J. and Ghani, A. (2000). Tansley review no. 110 - numerical and physical properties of orchid seeds and their biological implications. *New Phytologist* **145**, 367–421.

Argentina, M. and Mahadevan, L. (2005). Fluid-flow-induced flutter of a flag. *Proceedings of the National Academy of Sciences of the United States of America* **102**, 1829–1834.

Aylor, D. (1975). Force required to detach conidia of *helminthosporium maydis*. *Plant Physiology* **55**, 99–101.

Aylor, D. (1990). The role of intermittent wind in the dispersal of fungal pathogens. *Annual Review of Phytopathology* **28**, 73–92.

Aylor, D. and Parlange, J. (1975). Ventilation required to entrain small particles from leaves. *Plant Physiology* **56**, 97–99.

Bainbridge, A. and Legg, B. (1976). Release of barley-mildew conidia from shaken leaves. *Transactions of the British Mycological Society* **66**, 495–498.

Baker, C. (1995). The development of a theoretical-model for the windthrow of plants. *Journal of Theoretical Biology* **175**, 355–372.

Batchelor, G. (1967). *An Introduction to Fluid Dynamics*. Cambridge University Press.

Bergman, T., Lavine, A., Incropera, F. and DeWitt, D. (2011). *Fundamental of Heat and Mass Transfer*. Wiley, 7th edition.

Blasius, H. (1908). Grenzschichten in flüssigkeiten mit kleiner reibung. *Zeitschrift für angewandte Mathematik und Physik* **56**, 1–37.

Blevins, R. (1990). *Flow-induced Vibration*. New York: Van Nostrand Reinhold.

Boulbene, B., Morchain, J., Bonin, M., Janel, S., Lafont, F. and Schmitz, P. (2012). A combined computational fluid dynamics (cfd) and experimental approach to quantify the adhesion force of bacterial cells attached to a plane surface. *Aiche Journal* **58**, 3614–3624.

Braun, U. and Cook, R. (2012). *Taxonomic Manual of the Erysiphales (Powdery Mildews)*. Biodiversity Series No. 11. CBS.

Bullock, J. and Clarke, R. (2000). Long distance seed dispersal by wind: measuring and modelling the tail of the curve. *Oecologia* **124**, 506–521.

Butman, C. (1989). Sediment-trap experiments on the importance of hydrodynamical processes in distributing invertebrate larvae in near-bottom waters. *Journal of Experimental Marine Biology and Ecology* **134**, 37–88.

Cheer, A. and Koehl, M. (1987). Paddles and rakes: Fluid flow through bristled appendages of small organisms. *Journal of Theoretical Biology* **129**, 17–39.

Chen, L. (2010). An integral approach for large deflection cantilever beams. *International Journal of Non-Linear Mechanics* **45**, 301–305.

Chung, E., Kweon, H., Yiacoumi, S., Lee, I., Joy, D. and Palumbo, A. (2010). Adhesion of spores of *bacillus thuringiensis* on a planar surface. *Environmental Science and Technology* **44**, 290–296.

Cionco, R. (1965). A mathematical model for air flow in a vegetative canopy. *Journal of Applied Meteorology* **4**, 517–522.

Cisneros, L., Cortez, R., Dombrowski, C., Goldstein, R. and Kessler, J. (2007). Fluid dynamics of self-propelled microorgamisms, from individuals to concentrated population. *Experiments in Fluids* **43**, 737–753.

Clerk, G. and Ankora, J. (1969). Development and release of conidia of *phyllactinia corylea*. *Canadian Journal of Botany* **47**, 1289–1291.

Conova, S. (1999). Role of particle wettability in capture by a suspension-feeding crab (*emerita talpoida*). *Marine Biology* **133**, 419–428.

Cook, R., Henricot, B., Henrici, A. and Beales, P. (2006). Morphological and phylogenetic comparisons amongst powdery mildews on catalpa in the uk. *Mycological Research* **110**, 672–685.

Crimaldi, J., Thompson, J., Rosman, J., Lowe, R. and Koseff, J. (2002). Hydrodynamics of larval settlement: The influence of turbulent stress at potential recruitment sites. *Limnology and Oceanography* **47**, 1137–1151.

Cullum, F. and Webster, J. (1977). Cleistocarp dehiscence in *phyllactinia*. *Transactions of the British Mycological Society* **68**, 316–320.

de la Fuente, L., Montanes, E., Meng, Y., Li, Y., Burr, T., Hoch, H. and Wu, M. (2007). Assessing adhesion forces of type i and type iv pili of *xylella fastidiosa* bacteria by use of a microfluidic flow chamber. *Applied and Environmental Microbiology* **73**, 2690–2696.

de Langre, E. (2008). Effects of wind on plants. *Annual Review of Fluid Mechanics* **40**, 141–168.

de Montaudouin, X., Bachelet, G. and Sauriau, P. (2003). Secondary settlement of cockles *cerastoderma edule* as a function of current velocity and substratum: a flume study with benthic juveniles. *Hydrobiologie* **503**, 103–116.

Dennis, R., ed. (1976). *Handbook on Aerosols*. Technical Information Center Energy Research and Development Administration.

Denny, M. (1988). *Biology and the Mechanics of the Wave-Swept Environment*. Princeton, NJ: Princeton UP.

Denny, M. and Gaines, S. (2007). *Encyclopedia of Tidepools and Rocky Shores*. University of California Press.

Denny, M., Hunt, L., Miller, L. and Harley, C. (2009). On the prediction of extreme ecological events. *Ecological Monographs* **79**, 397–421.

Dudley, R. (2002). Mechanisms and implications of animal flight maneuverability. *Integrative and Comparative Biology* **42**, 135–140.

Dudley, R. and Ellington, C. (1990). Mechanics of forward flight in bumblebees .2. quasi-steady lift and power requirements. *Journal of Experimental Biology* **148**, 53–88.

Dudley, R. and Yanoviak, S. (2011). Animal aloft: The origins of aerial behavior and flight. *Integrative and Comparative Biology* **51**, 926–936.

Eckman, J. (1996). Closing the larval loop: Linking larval ecology to the population dybnamics of marine benthic invertebrates. *Journal of Experimental Marine Biology and Ecology* **200**, 207–237.

Eckman, J., Savidge, W. and Gross, T. (1990). Relationship between duration of cyprid attachement and drag forces associated with detachment of balanus-amphitrite cyrpids. *Marine Biology* **107**, 111–118.

Edwards, J., Whitaker, D., Klionsky, S. and Laskowski, M. (2005). Botany - a record-breaking pollen catapult. *Nature* **435**, 164–164.

Elbert, W., Taylor, P. and Poschl, M. A. U. (2007). Contribution of fungi to primary biogenic aerosols in the atmosphere: wet and dry discharged spores, carbohydrates, and inorganic ions. *Atmospheric Chemistry and Physics* **7**, 4569–4588.

Emerson, S. and Koehl, M. (1990). The interaction of behavioral and morphological change in the evolution of a novel locomotor type - flying frogs. *Evolution* **44**, 1931–1946.

Estes, J. and Peterson, C. (2000). Marine ecological research in seashore and seafloor systems: accomplishments and future directions. *Marine Ecology Progress Series* **195**, 281–289.

Faegri, K. and Pijl, L. V. D. (1978). *Principles of Pollination Ecology*. Pergamon international library of science, technology, engineering, and social studies.

Ferrandino, F. and Aylor, D. (1984). Settling speed of clusters of spores. *Phytopathology* **74**, 969–972.

Finnigan, J. (2000). Turbulence in plant canopies. *Annual Review of Fluid Mechanics* **32**, 519–571.

Fischer, M., Cox, J., Davis, D., Wagner, A., Taylor, R., Huerta, A. and Money, N. (2004). New information on the mechanism of forcible ascospore discharge from *ascobolus immersus*. *Fungal Genetics and Biology* **41**, 698–707.

Forterre, Y. (2013). Slow, fast and furious: understanding the physics of plant movements. *Journal of Experimental Botany* **64**, 4745–4760.

Friedman, J. and Barrett, S. (2009). Wind of change: new insights on the ecology and evolution of pollination and mating in wind-polinated plants. *Annals of Botany* **103**, 1515–1527.

Fritz, J., Seminara, A., Roper, M., Pringle, A. and Brenner, M. (2013). A natural o-ring optimizes the dispersal of fungal spores. *Journal of the Royal Society Interface* **10**.

Gadoury, D., Asalf, B., Heidenreich, M., Herrero, M., Weiser, M., Seem, R., Tronsmo, A. and Stensvand, A. (2010). Initiation, development, and survival of cleistothecia of *podosphaera aphanis* and their role in the epidemiology of strawberry powdery mildew. *Phytopathology* **100**, 246–251.

Gadoury, D. and Pearson, R. (1988). Initiation, development, dispersal, and survival of cleistothecia of *uncinula necator* in new-york vineyards. *Phytopathology* **78**, 1413–1421.

Gaines, S. and Denny, M. (1993). The largest, smallest, highest, lowest, longest, and shortest - extremes in ecology. *Ecology* **74**, 1677–1692.

Gaylord, B., Denny, M. and Koehl, M. (2008). Flow forces on seaweeds: field evidence for roles of wave impingement and organism inertia. *Biological Bulletin* **215**, 295–308.

Gere, J. and Timoshenko, S. (1997). *Mechanics of Materials*. Boston PWS, 4th edition.

Glawe, D. (2006). Synopsis of genera of erysiphales (powdery mildew fungi) occurring in the pacific northwest. *Pacific Northwest Fungi* **1**, 27.

Glawe, D. (2008). The powdery mildews: A review of the world's most familiar (yet poorly known) plant pathogens. *Annual Review of Phytopathology* **46**, 27–51.

Grace, J. (1978). The turbulent boundary layer over a flapping populus leaf. *Plant, Cell and Environment* **1**, 35–38.

Grace, J. and Collins, M. (1976). Spore liberation from leaves by wind. In *Microbiology of aerial plant surface* (eds. C. Dickinson and T. Preece), pp. 185–198. Academic Press, London.

Granbaum, D. and Strathmann, R. (2003). Form, performance and trade-offs in swimming and stability of armed larvae. *Journal of Marine Research* **61**, 659–691.

Gregory, P. (1961). Plant science monographs. In *The microbiology of the atmosphere* (ed. N. Polunin). Leonard Hill.

Gregory, P. and Henden, D. (1976). Terminal velocity of basidiospores of giant puffball (lycoperdon-giganteum). *Transactions of the British Mycological Society* **67**, 399–407.

Grove, G. (1998). Meteorological factors affecting airborne conidia concentrations and the latent period of podosphaera clandestina on sweet cherry. *Plant Disease* **82**, 741–746.

Guinez, R. and Pacheco, C. (1999). Maximum wave velocity estimations on the intertidal rocky shore at central chile, using a prototype dynamometer. *Revista Chilena De Historia Natural* **72**, 251–260.

Hammer, K. (2005). Remarks to the breeding systems of the triticeae with special reference to the pollen to *ovule ratios*. *Czech Journal of Genetics and Plant Breeding* **41**, 145–153.

Haugen, N. and Kragset, S. (2010). Particle impaction on a cylinder in a crossflow as function of stokes and reynolds numbers. *Journal of Fluid Mechanics* **661**, 239–261.

Heilderberg, K., Sebens, K. and Purcell, J. (2004). Composition and sources of near reef zooplankton on a jamaican forereef along with implications for coral feeding. *Coral Reefs* **23**, 263–276.

Heip, C., Goosen, N., Herman, P., Kromkamp, J., Middelburg, J. and Soetaert, K. (1995). Production and consumption of biological particles in temperate tidal estuaries. *Oceanography and Marine Biology - an Annual Review* **33**.

Hinds, W. (1999). *Aerosol Technology*. Wiley - Interscience, 2nd edition.

Horn, H., Nathan, R. and Kaplan, S. (2001). Long-distance dispersal of tree seeds by wind. *Ecological Research* **16**, 877–885.

Howe, H. and Smallwood, J. (1982). Ecology of seed dispersal. *Annual Review of Ecology and Systematics* **12**, 201–228.

Humphries, S. (2009). Filter feeders and plankton increase particle encounter rates through flow regime control. *Proceedings of the National Academy of Sciences of the United States of America* **106**, 7882–7887.

Hunter, T. (1989). Suspension feeding in oscillating flow: the effect of coloby morphology and flow regime on plankton capture by the hydroid *obellia longissima*. *Biological Bulletin* **176**, 41–49.

Ingold, C. (1965). *Spore Liberation*. Oxford University Press.

Ingold, C. (1992). The basidium: A spore-gun of precise range. *Mycologist* **6**, 111–113.

Iqbal, A., Beaugrand, J., Garnier, P. and Recous, S. (2013). Tissue density determines the water storage characteristics of crop residues. *Plant and Soil* **367**, 285–299.

Itoi, S., Nakayama, K. and Kubomura, Y. (1962). Studies on the powdery mildew disease of mulberry tree caused by *phyllactinia moricola* (p. henn.) homma. *Bull. sericult. Exp. Stn.* **17**, 321–445.

Jackson, S. and Lyford, M. (1999). Pollen dispersal models in quaternary plant ecology: Assumptions, parameters, and prescriptions. *Botanical Review* **65**, 39–75.

Jarvis, W., Gubler, W. and Grove, G. (2002). Epidemiology of powdery mildews in agricultural pathosystems. *Powdery Mildews: a Comprehensive Treatise* pp. 169–199.

Johnson, A. and Sebens, K. (1993). Consequences of a flattened morphology - effects of flow on feeding rates of the scleractinian coral *meandrina meandrites*. *Marine Ecology Progress Series* **99**, 99–114.

Jonsson, P., Adre, C. and Lindegarth, M. (1991). Swimming behavior of marine bivalave larvae in a flume boundary-layer flow - evidence for near-bottom confinement. *Marine Ecology Progress Series* **79**, 67–76.

Jusufi, A., Kawano, D., Libby, T. and Full, R. (2010). Righting and turning in mid-air using appendage inertia: reptile tails, analytical models and bio-inspired robots. *Bioinspiration and Biomimetics* **5**, 12.

Jusufi, A., Zeng, Y., Full, R. and Dudley, R. (2011). Aerial righting reflexes in flightless animals. *Integrative and Comparative Biology* **51**, 937–943.

Kay, M. and Emlet, R. (2002). Laboratory spawning, larval development, and metamorphosis of the limpets *lottia digitalis* and *lottia asmi* (patellogastropoda, lotiidae). *Invertebrate Biology* **121**, 11–24.

King, M. and Buchmann, S. (1995). Bumble bee-initiated vibration release mechanism of rhododendron pollen. *American Journal of Botany* **82**, 1407–1411.

Kiorboe, T. (2008). *A mechanistic approach to plankton ecology*. Princton University Press.

Kiorboe, T., Anderson, A., Langlois, V. and Jakobsen, H. (2010). Unsteady motion: escape jumps in planktonic copepods, their kinematics and energetics. *Journal of the Royal Society Interface* **7**, 1591–1602.

Koehl, M. (1977). Effects of sea-anemones on flow forces they encounter. *Journal of Experimental Biology* **69**, 87–105.

Koehl, M. (2003). Physical modeling in biomechanics. *Philosophical Transactions of The Royal Society* **358**, 1589–1596.

Koehl, M. (2007). Mini review: Hydrodynamics of larval settlement into fouling communities. *Biofouling* **23**, 357–368.

Koehl, M., Evangelista, D. and Yang, K. (2011). Using physical models to study the gliding performance of extinct animals. *Integrative and Comparative Biology* **51**, 1002–1018.

Koehl, M. and Hadfield, M. (2004). Soluble settlement cue in slowly moving water within coral reefs induces larval adhesion surfaces. *Journal of Marine Systems* **49**, 75–88.

Koehl, M. and Hadfield, M. (2010). Hydrodynamics of larval settlement from a larva's point of view. *Integrative and Comparative Biology* **50**, 539–551.

Koehl, M. and Reidenbach, M. (2007). Swimming by microscopic organisms in ambient water flow. *Experiments in Fluids* **43**, 755–768.

Kumar, V. and Gupta, V. (2004). Scanning electron microscopy on the perithecial development of *phyllactinia corylea* on mulberry - ii. sexual stage. *Journal of Phyopathology* **152**, 169–173.

Kuparinen, A. (2006). Mechanistic models for wind dispersal. *Trends in Plant Science* **11**, 296–301.

Labarbera, M. (1984). Feeding currents and particle capture mechanisms in suspension feeding animals. *American Zoologist* **24**, 71–84.

Lacey, J. (1996). Spore dispersal - its role in ecology and disease: The british contribution to fungal aerobiology. *Mycological Research* **100**, 641–660.

Levin, S. (1992). The problem of pattern and scale in ecology. *Ecology* **73**, 1943–1967.

Libby, T., Moore, T., Chang-Siu, E., Li, D., Cohen, D., Jusufi, A. and Full, R. (2012). Tail-assisted pitch control in lizards, robots and dinosaurs. *Nature* **481**, 181–184.

Liberato, J. (2007). Taxonomic notes on two powdery mildews: *Phyllactinia chorisiae* and *ovulariopsis wissadulae* (erysiphaceae : Phyllactinieae). *Mycotaxon* **101**, 29–34.

Loth, E. (2008). Drag of non-spherical solid particles of regular and irregular shape. *Powder Technology* **182**, 342–353.

Loubet, B., Jarosz, N., Saint-Jean, S. and Huber, L. (23). A method for measuring the settling velocity distribution of large biotic particles. *Aerobiologia* **2**.

Loudon, C., Best, B. and Koehl, M. (1994). When does motion relative to neighboring surfaces alter the flow through arrays of hairs. *Journal of Experimental Biology* **193**, 233–254.

Mace, A. and Morgan, S. (2006). Larval accumulation in the lee of a small headland: implications for the design of marine reserves. *Marine Ecology Progress Series* **318**, 19–29.

Marcus, N. (1995). Seasonal study of planktonic copepods and their benthic resting eggs in northern california coastal waters. *Marine Biology* **123**, 459–465.

Marmottant, P., Ponomarenko, A. and Bienaime, D. (2013). The walk and jump of *equisetum* spores. *Proceedings of the Royal Society B-Biological Sciences* **280**, 5.

Martinez, M. (2001). Running in the surf: hydrodynamics of the shore crab *grapsus tenuicrustatus*. *Journal of Experimental Biology* **204**, 3097–3112.

Martinez-Berdeja, A., Torres, M., Altshuler, D. and Ezcurra, E. (2014). Hydration history and attachment morphology regulate seed release in *chorizanthe rigida* (polygonaceae), a serotinous desert annual seed release in *chorizanthe rigida* (polygonaceae), a serotinous desert annual. *American Journal of Botany* **101**, 1079–1084.

McCartney, H., Fitt, B. and West, J. (2006). Dispersal of foliar plant pathogens: mechanisms, dispersal of foliar plant pathogens: mechanisms, dispersal of foliar plant pathogens: mechanisms, gradients and spatial patterns. In *The Epidemiology of Plant Dispersal* (eds. B. Cook, D. Jones and B. Kaye). Dordrecht: Springer.

McCay, M. (2001). Aerodynamic stability and maneuverability of the gliding frog *polypedates dennysi*. *Journal of Experimental Biology* **204**, 2817–2826.

McEdward, L. (1995). *Ecology of marine invertebrate larvae*. CRC Press.

McHenry, M., Azizi, E. and Strother, J. (2003). The hydrodynamics of locomotion at intermediate reynolds numbers: undulatory swimming in ascidian larvae (*botrylloides* sp.). *Journal of Experimental Biology* **206**, 327–343.

Meinzer, F. and Goldstein, G. (1985). Some consequences of leaf pubescence in the andean giant rosette plant *espeletia timotensis*. *Ecology* **66**, 512–520.

Miller, K., Blower, S., Hedgecock, D. and Roughgarden, J. (1989). Comparison of larval and adult stages of *chthamalus dalli* and *chthamalus fissus* (cirripedia: Thoracica). *Journal of Crustacean Biology* **9**, 242–256.

Miller, L., Santhanakrishnan, A., Jones, S., Hamlet, C., Mertens, K. and Zhu, L. (2012). Reconfiguration and the reduction of vortex-induced vibrations in broad leaves. *Journal of Experimental Biology* **215**, 2716–2727.

Money, N. and Fischer, W. (2009). Plant relationships. In *The Mycota: A Comprehensive Treatise on Fungi as Experimental Systems for Basic and Applied Research* (eds. K. Esser and H. Deising), volume 5, chapter 6: Biomechanics of Spore Release in Phytopathogens. Springer, 2nd edition.

Morris, R., Abbott, D. and Haderlie, E. (1980). *Intertidal Invertebrates of California*. Stanford University Press.

Munk, J. D. (2011). *The Descent of Ant*. Ph.D. thesis, University of California, Berkeley.

Murren, C. and Ellison, A. (1998). Seed dispersal characteristics of *brassavola nodosa* (orchidaceae). *American Journal of Botany* **85**, 675–680.

Nathan, R., Katul, G., Nohrer, G., Kuparinen, A., Soons, M., Thompson, S., Trakhtenbrot, A. and Horn, H. (2011). Mechanistic models of seed dispersal by wind. *Theoretical Ecology* **4**, 113–132.

Nathan, R., Safriel, U. and Noy-Meir, I. (2001). Field validation and sensitivity analysis of a mechanistic model for tree seed dispersal by wind. *Ecology* **82**, 374–388.

Neger, F. (1902). Neue beobachtungen uber das spontane freiwerden der erysiphaceenfruchtkorpen. *Centralblatt fur Bakteriologie und Parasitologie* **2**, 570–573.

Niklas, K. (1985). The aerodynamics of wind pollination. *Botanical Review* **51**, 328–386.

Nobel, P. (1975). Effective thickness and resistance of air boundary-layer adjacent to spherical plant parts. *Journal of Experimental Botany* **26**, 120–130.

Noblin, X., Yang, S. and Dumais, J. (2009). Surface tension propulsion of fungal spores. *Journal of Experimental Biology* **212**, 2835–2843.

Norberg, R. (1973). Autorotation, self-stability, and structure of single-winged fruits and seeds (samaras) with comparative remarks on animal flight. *Biological Reviews of the Cambridge Philosophical Society* **48**, 561–596.

Nowell, A. and Jumars, P. (1987). Flumes - theoretical and experimental considerations for simulation of benthic environments. *Oceanography and Marine Biology* **25**, 91–112.

Nybakken, J. (2004). *Marine Biology: An Ecological Approach*. Menlo Park, CA: Benjamin Cummings, 6th edition.

Okubo, A. and Levin, S. (1989). A theoretical framework for data-analysis of wind dispersal of seeds and pollen. *Ecology* **70**, 329–338.

Oliver, J., ed. (2005). *Encyclopedia of world climatology*. Springer.

O'neill, M. (1968). A sphere in contact with a plane wall in a slow linear shear flow. *Chemical Engineering Science* **23**, 1293–1298.

Pady, S., Kramer, C., Pathak, V., Morgan, F. and Bhatti, M. (1965). Periodicity in airborne cereal rust urediospores. *Phytopathology* **55**, 132–136.

Paine, R. (1994). *Marine Rocky Shores and Community Ecology: An Experimentalist's Perspective*. Germany: Ecology Institute: Oldendorf/Luhe.

Pang, M. and Wei, J. (2011). Analysis of drag and lift coefficient expressions of bubbly flow systems for low to medium reynolds number. *Nuclear Engineering and Design* **241**, 2204–2213.

Pasternak, Z., Blasius, B., Achituv, Y. and Abelson, A. (2004). Host location in flow by larvae of the symbiotic barnacle *trevathana dentata* using odour-gated rheotaxis. *Proceedings of the Royal Society B - Biological Sciences* **271**, 1745–1750.

Piepenbring, M., Hagedorn, G. and Oberwinkler, F. (1998). Spore liberation and dispersal in smut fungi. *Botanica Acta* **111**, 444–460.

Pratt, M. (2008). Living where the flow is right: How flow affects feeding in bryozoans. *Integrative and Comparative Biology* **48**, 808–822.

Pringle, A., Patek, S., Fischer, M., Stolze, J. and Money, N. (2005). The captured launch of ballistospore. *Mycologia* **97**, 866–871.

Reidenbach, M., Koseff, J. and Koehl, M. (2009). Hydrodynamic forces on larvae affect their settlement on coral reefs in turbulent, wave-driven flow. *Limnology and Oceanography* **54**, 318–330.

Ribak, G., Gish, M., Weihs, D. and Inbar, M. (2013). Adaptive aerial righting during the escape dropping of wingless pea aphids. *Current Biology* **23**, R102–R103.

Ribak, G. and Swallow, J. (2007). Free flight maneuvers of stalk-eyed flies: do eye-stalks affect aerial turning behavior? *Journal of Comparative Physiology Neuroethology Sensory Neural and Behavioral Physiology* **193**, 1065–1079.

Roberts, J., Elliott, K. and Gonzalez-Carranza, Z. (2002). Abscission,dehiscence, and other cell separation processes. *Annual Review of Plant Biology* **53**, 131–158.

Robinson, H., Finelli, C. and Koehl, M. (2013). Interactions between benthic predators and zooplankton prey are affected by turbulent waves. *Integrative and Comparative Biology* **53**, 810–820.

Roden, J. and Pearcy, R. (1993). The effect of flutter on the temperature of poplar leaves and its implications for carbon gain. *Plant, Cell and Environment* **16**, 571–577.

Rodriguez, S., Ojeda, F. and Inestrosa, N. (1993). Settlement of benthic marine-invertebrates. *Marine Ecology Progress Series* **97**, 193–207.

Roper, M., Pepper, R., Brenner, M. and Pringle, A. (2008). Explosively launched spores of ascomycete fungi have drag-minimizing shapes. *Proceedings of the National Academy of Sciences of the United States of America* **105**, 20583–20588.

Roper, M., Seminara, A., Bandi, M., Cobb, A., Dillard, H. and Pringle, A. (2010). Dispersal of fungal spores on a cooperatively generated wind. *Proceedings of the National Academy of Sciences of the United States of America* **107**, 17474–17479.

Rubenstein, D. and Koehl, M. (1977). Mechanisms of filter feeding - some theoretical considerations. *American Naturalist* **111**, 981–994.

Ryley, M. and Chakraborty, S. (2008). Patterns of release of the secondary conidia of *claviceps africana*, the sorghum ergot pathogen in australia. *Plant Pathology* **57**, 473–483.

Salcedo, E., Trevino, C., Vargas, R. and Martinez-Suastegui, L. (2013). Stereoscopic particle image velocimetry measurements of the three-dimensional flow field of a descending autorotating mahogany seed (*swietenia macrophylla*). *Journal of Experimental Biology* **216**, 1017–2030.

Sane, S. (2003). The aerodynamics of insect flight. *Journal of Experimental Biology* **206**, 4191–4208.

Schiel, D. (2004). The structure and replenishment of rocky shore intertidal communities and biogeographic comparisons. *Journal of Experimental Marine Biology and Ecology* **300**, 309–342.

Schippers, P. and Jongejans, E. (2005). Release thresholds strongly determine the range of seed dispersal by wind. *Ecological Modeling* **185**, 93–103.

Schlichting, H. (1979). *Boundary Layer Theory*. New York: McGraw-Hill.

Schreuder, M., Brewer, C. and Heine, C. (2001). Modelled influences of non-exchanging trichomes on leaf boundary layers and gas exchange. *Journal of Theoretical Biology* **210**, 23–32.

Schuepp, P. (1993). Tansley review no. 59 leaf boundary-layers. *New Phytologist* **125**, 477–507.

Schwendemann, A., Wang, G., Mertz, M., McWilliams, R., Thatcher, S. and Osborn, J. (2007). Aerodynamics of saccate pollen and its implications for wind pollination. *American Journal of Botany* **94**, 1371–1381.

Sebens, K. (1981). The allometry of feeding, energetics, and body size in three sea anemone species. *Biological Bulletin* **161**, 152–171.

Sebens, K. and Koehl, M. (1984). Predation on zooplankton by the benthic anthozoans *alcyonium siderium* (alcyonacea) and *metridium senile* (actiniaria) in the new england subtidal. *Marine Biology* **81**, 255–271.

Sharpe, D. and Fields, D. (1982). Integrating the effects of climate and seed fall velocities on seed dispersal by wind - a model and application. *Ecological Modeling* **17**, 297–310.

Shimeta, J. and Jumars, P. (1991). Physical-mechanisms and rates of particle capture by suspension-feeders. *Oceanography and Marine Biology* **29**, 191–257.

Shimeta, J. and Koehl, M. (1997). Mechanisms of particle selection by tentaculate suspension feeders during encounter, retention, and handling. *Journal of Experimental Marine Biology and Ecology* **209**, 47–73.

Skotheim, J. and Mahadevan, L. (2005). Physical limits and design principles for plant and fungal movements. *Science* **308**, 1308–1310.

Slusarenko, A. and Schlaich, N. (2003). Downy mildew of *arabidopsis thaliana* caused by *hyaloperonospora parasitica* (formerly *peronospora parasitica*). *Molecular Plant Pathology* **4**, 159–170.

Smith, D. (1977). *A Guide to Marine Coastal Plankton and Marine Invertebrate Larvae*. Kendall/Hunt Publishing Company.

Strickler, J. (1977). Observation of swimming performances of planktonic copepods. *Limnology and Oceanography* **22**, 165–169.

Suter, R. (1991). Ballooning in spiders - results of wind-tunnel experiments. *Ethology Ecology and Evolution* **3**, 13–25.

Tesmer, J. and Schnittler, M. (2007). Sedimentation velocity of myxomycete spores. *Mycological Progress* **6**, 229–234.

Thielicke, W. (2014). *The flapping flight of birds*. Ph.D. thesis, University of Groningen.

Thielicke, W. and Stamhuis, E. (2014). Pivlab – towards user-friendly, affordable and accurate digital particle image velocimetry in matlab. *Journal of Open Research Software* **2**, 30.

Timerman, D., Greene, D., Urzay, J. and Ackerman, J. (2014). Turbulence-induced resonance vibrations cause pollen release in wind-pollinated *plantago lanceolata l.* (plantaginaceae). *Journal of the Royal Society Interface* **11**, 7.

Trail, F., Gaffoor, I. and Vogel, S. (2005). Ejection mechanics and trajectory of the ascospores of *gibberella zeae* (anamorph *fuarium graminearum*). *Fungal Genetics and Biology* **42**, 528–533.

Turner, J. (2004). The importance of small planktonic copepods and their roles in pleagic marine food webs. *Zooligical Studies* **43**, 255–266.

Urzay, J., Smith, S., Thompson, E. and Glover, B. (2009). Wind gusts and plant aeroelasticity effects on the aerodynamics of pollen shedding: A hypothetical turbulence-initiated wind-pollination mechanism. *Journal of Theoretical Biology* **259**, 785–792.

van Hout, R., Zhu, W., Luznik, L., Katz, J., Kleissl, J. and Parlange, M. (2007). Piv measurements in the atmospheric boundary layer within and above a mature corn canopy. part i: Statistics and energy flux. *Journal of Atmospheric Sciences* **64**, 2805–2824.

Verma, A., Desai, A. and Mittal, S. (2013). Aerodynamics of badminton shuttlecocks. *Journal of Fluids and Structures* **41**, 89–98.

Visser, A. and Kiorboe, T. (2006). Plankton motility patterns and encounter rates. *Oecologia* **148**, 538–546.

Vogel, S. (1989). Drag and reconfiguration of broad leaves in high winds. *Journal of Experimental Botany* **40**, 941–948.

Vogel, S. (1996). *Life in Moving Fluid: The Physical Biology of Flow*. Princeton, 2nd edition.

Vogel, S. (2009). Leaves in the lowest and highest winds: temperature, force and shape. *New Phytologist* **183**, 13–26.

Wainwright, S., Biggs, W., Currey, J. and Gosline, J. (1976). *Mechanical Designs in Organisms*. Edward Arnold.

Wallenberger, F., Watson, J. and Li, H. (2001). Glass fibers. In *ASM Handbook*, volume 21, Composites, pp. 27–34. ASM International.

Weber, P., Howle, L., Murray, M. and Fish, F. (2009). Lift and drag performance of *odontocete cetacean* flippers. *Journal of Experimental Biology* **212**, 2149–2158.

Webster, J. (1979). Cleistocarps of *phyllactinia* as shuttlecocks. *Transactions of the British Mycological Society* **72**, 489–490.

White, F. (1974). *Viscous Fluid Flow*. McGraw-Hill.

Willocquet, L., Berud, F., Raoux, L. and Clerjeau, M. (1998). Effects of wind, relative humidity, leaf movement and colony age on dispersal of conidia of *uncinula necator*, causal agent of grape powdery mildew. *Plant Pathology* **47**, 234–242.

Woolley, J. (1964). Water relations of soybean leaf hairs. *Argon J* **56**, 569–571.

Yanoviak, S., Munk, Y. and Dudley, R. (2011). Evolution and ecology of directed aerial descent in arboreal ants. *Integrative and Comparative Biology* **51**, 944–956.

Yanoviak, S., Munk, Y., Kaspari, M. and Dudley, R. (2010). Aerial manoeuvrability in wingless gliding ants (*cephalotes atratus*). *Proceedings of the Royal Society B-Biological Sciences* **277**, 2199–2204.

Yule, A. and Walker, G. (1984). The adhesion of the barnacle, *balanus balanoides*, to slate surfaces. *Journal of the Marine Biological Association of the United Kingdom* **64**, 147–156.

Zardus, J., Nedved, B., Huang, Y., Tran, C. and Hadfield, M. (2008). Micronial biofilms facilitate adhesion in biofouling invertebrates. *Biological Bulletin* **214**, 91–98.

Zhang, J., Childress, S., Libchaber, A. and Shelley, M. (2000). Flexible filaments in a flowing soap film as a model for one-dimensional flags in a two-dimensional wind. *Nature* **408**, 835–839.

Zhou, Y. and Kot, M. (2013). Life on the move: modeling the effects of climate-driven range shifts with integrodifference equations. In *Dispersal, Individual Movement and Spatial Ecology: A Mathematical Perspective* (eds. M. Lewis, P. Maini and S. Petrovskii), volume 2071. Springer.

Zimmer, R., Fingerut, J. and Zimmer, C. (2009). Dispersal pathways, seed rains, and the dynamics of larval behavior. *Ecology* **90**, 1933–1947.